eROSITA observations of the non-thermal supernova remnant HESS J1731-347

MASTER THESIS
for the acquisition of the academic degree
Master of Science

Mirjam Bogner

January 25, 2023

Eberhard Karls Universität Tübingen

Institut für Astronomie und Astrophysik (IAAT)
Abteilung Hochenergieastrophysik

Eigenständigkeitserklärung

Hiermit erkläre ich, Mirjam Bogner, Matrikelnummer 4076894, dass ich die vorliegende Arbeit mit dem Titel “eROSITA observations of the non-thermal supernova remnant HESS J1731-347” selbstständig verfasst und keine anderen als die angegebenen Quellen und Hilfsmittel benutzt habe. Alle sinngemäß und wörtlich übernommenen Textstellen aus fremden Quellen wurden kenntlich gemacht. Ich versichere, dass die Arbeit weder vollständig noch zu wesentlichen Teilen Gegenstand eines anderen Prüfungsverfahrens war und weder vollständig noch in wesentlichen Teilen bereits veröffentlicht wurde. Das in Dateiform eingereichte Exemplar stimmt mit den gebundenen Exemplaren überein.

Tübingen, 25.01.2023

....

Mirjam Bogner

Abstract

Supernova remnants (SNRs) are believed to be cosmic ray acceleration sites. The non-thermal X-ray synchrotron radiation that is emitted by some of them is produced by relativistic electrons and therefore carries information about the particle acceleration proceeding at the SNR shock front. The radiation produced by an SNR is influenced by its interactions with the interstellar medium. In particular, interactions with a non-uniform environment are expected to cause changes in the spectrum across the SNR which can be revealed by a spatially resolved X-ray spectroscopy. For the non-thermal SNR HESS J1731-347, radio emission and X-ray absorption maps indicate the presence of a molecular cloud in its western vicinity. While there are strong observational indications that the remnant is interacting with the cloud, a proof is still missing.

In this Master Thesis work, variations of the absorption and the photon index across HESS J1731-347 are traced in a spatially resolved X-ray spectroscopy using eROSITA survey data. Spectra are extracted from several square regions covering the SNR and nearby background regions. Due to the low counting statistics of the data, in a first approach, the presence of a linear gradient in both the absorption an the photon index was tested. This model turned out not to be a good representation for the absorption variations. Therefore, the absorption was allowed to vary independently between different regions. The resulting absorption pattern shows an increasing trend towards the western part of the remnant and additional variations in north-south direction. Since counting statistics do not allow a fit with also independent photon indices, photon index variations could only be constrained using the linear gradient approximation. Despite the poor counting statistics, a decreasing component in western direction was found at 2.5σ significance.

The relative orientation of absorption and photon index variations is surprising: Towards the western part, where the absorption is increasing and most likely a molecular cloud is present, the spectrum of the remnant appears to be harder. Given that the expansion velocity of the remnant shock is slowed down when interacting with a dense environment, an eventual interaction with the molecular cloud is expected to lead to softer rather than harder spectra. This is because the maximum energy that particles can gain through diffusive shock acceleration is reduced for a slower expanding shock. Thus, the finding for the photon index gradient which indicates harder spectra towards the western part of the remnant cannot be explained in this simple picture.

Zusammenfassung

Supernova-Überreste zählen zu den möglichen Erzeugern galaktischer kosmischer Strahlung. Die nicht-thermische Röntgen-Synchrotronstrahlung, welche von einigen dieser Objekte emittiert wird, ist ein Indikator für die Präsenz relativistischer Elektronen. Daher gibt ihre Untersuchung Aufschluss über die Beschleunigungsmechanismen geladener Teilchen an der Schockfront des Supernova-Überrestes. Die von einem Supernova-Überrest erzeugte Strahlung wird durch seine Wechselwirkung mit der umgebenden Materie beeinflusst. Interaktionen mit einer nicht-homogenen Umgebung spiegeln sich in Veränderungen des Spektrums innerhalb der Quelle wider, welche durch eine räumlich aufgelöste Röntgen-Spektralanalyse untersucht werden können. Im Fall des nicht-thermischen Supernova-Überrests HESS J1731-347 weisen Radio-Emissionsdaten und die Röntgen-Absorption darauf hin, dass sich nahe dem westlichen Teil der Quelle eine Molekülwolke befindet. Zwar gibt es starke Indikationen für eine Interaktion des Supernova-Überrestes mit dieser Wolke, ein Beweis konnte allerdings bisher nicht erbracht werden.
In der vorliegenden Arbeit wird eine räumlich aufgelöste Röntgen-Spektralanalyse von HESS J1731-347 anhand von eROSITA Survey Daten durchgeführt mit dem Ziel, nach Variationen der Absorption und des Photonindex' innerhalb der Quelle zu suchen. Dazu werden Spektren mehrerer quadratischer Unterregionen extrahiert, welche die Quelle sowie angrenzende Hintergrundbereiche abdecken. Angesichts der geringen Zählstatistik der verfügbaren eROSITA Daten wird zunächst die Präsenz eines linearen Gradienten sowohl in den Absorptions-Werten als auch in denen des Photonindex' überprüft. Im Falle der Absorption erwies sich dieses Modell nicht als geeignete Repräsentation, weshalb im weiteren Verlauf die Werte der einzelnen Regionen als unabhängig voneinander angenommen werden. Dabei zeigt sich der Trend einer steigenden Absorption in westlicher Richtung und gleichzeitig Variationen in Nord-Süd-Richtung. Da die geringe Zählstatistik keinen Fit der Spektren mit ebenfalls unabhängigen Photonindex-Werten erlaubt, konnten Photonindex-Variationen nur unter der Annahme eines linearen Gradienten untersucht werden. Trotz der niedrigen Zählstatistik wurde eine in westlicher Richtung abnehmende Komponente mit einer Signifikanz von 2.5σ gefunden.
Die relative Orientierung der Variationen von Photonindex und Absorption ist überraschend: In westlicher Richtung, wo die Absorption zunimmt und sich wahrscheinlich eine Molekülwolke befindet, scheint das Spektrum der Quelle härter zu werden. Da die Ausbreitungsgeschwindigkeit der Schockfront durch Interaktion mit einer Umgebung höherer Dichte verlangsamt wird, erscheint es zunächst naheliegender, dass eine eventuelle Wechselwirkung mit der Molekülwolke zu einem weicheren statt härteren Spektrum führt. Denn die maximale Energie, welche geladene Teilchen durch die Beschleunigung an der Schockfront gewinnen können, wird mit abnehmender Ausbreitungsgeschwindigkeit des Schocks geringer. Folglich lässt sich das Ergebnis des Photonindex Gradienten, welches härtere Spektren im westlichen Teil der Quelle indiziert, in diesem einfachen Bild nicht erklären.

Contents

1. Introduction **1**
1.1. Supernovae . . . 1
1.2. Supernova remnants . . . 2
1.2.1. Classification . . . 2
1.2.2. Evolutionary phases . . . 2
1.2.3. Radiation processes of SNRs . . . 3
1.2.4. HESS J1731-347 . . . 5
1.3. The eROSITA telescope . . . 8
1.3.1. Instrumental properties . . . 9
1.4. Data set considered in the analysis . . . 10

2. eROSITA X-ray image **11**

3. Total remnant spectrum **13**
3.1. Extraction regions for source and background spectrum . . . 13
3.1.1. Point source removal . . . 14
3.2. Background subtracted fit . . . 16
3.2.1. General concept . . . 16
3.2.2. Optimization method and spectral model . . . 18
3.2.3. Fit results . . . 18
3.2.4. Sources of uncertainty . . . 21
3.3. Simultaneous fitting of background and source region spectra . . . 23
3.3.1. Background model . . . 23
3.3.2. Source model . . . 28
3.3.3. Fit of the background spectrum . . . 28
3.3.4. Fit of the source area spectrum . . . 30
3.3.5. Simultaneous fit of source and background area spectra . . . 37

4. Spatially resolved spectral analysis **44**
4.1. Method description . . . 44
4.1.1. Region definition and point source removal . . . 44
4.1.2. Model definition . . . 45
4.2. Results . . . 47
4.2.1. Fit with linked N_H and constant, frozen Γ_{SNR} . . . 47
4.2.2. Fit with independent N_H and constant, frozen Γ_{SNR} . . . 50
4.2.3. Deviations between linked and independent N_H values for frozen Γ_{SNR} . . . 52
4.2.4. Fit with linked N_H and linked Γ_{SNR} . . . 53
4.2.5. Fit with independent N_H and linked Γ_{SNR} . . . 57
4.3. Fit of spectra from sub-regions adapted to the surface brightness of the source as measured with XMM-Newton . . . 62
4.3.1. Constraining absorptions for a fixed photon index . . . 62
4.3.2. Constraining photon indices for fixed absorptions . . . 64

5. Outlook: Simulating eROSITA spectra with a larger exposure **67**
5.1. Method description . . . 67
5.2. Results . . . 68

6. Summary and conclusions **71**

References **74**

A. Comparison of total remnant spectral fit for different instrumental backgrounds **79**

B. Comparison of background spectra for different extraction regions **81**
B.1. Results of background subtracted fit 82

C. Fit results for simultaneous source and background region fit with TM12346 data only **83**

D. Background modelling fit for left and right half annulus background **84**

E. Comparison of sub-regions fits for constant N_H and N_H linked by gradient **87**

F. Spectra and models for 30 sub-regions with different N_H and Γ relations **88**

G. Angle spanned by N_H and Γ gradient **90**

H. Spectra and models for the 22 regions defined by Doroshenko et al. 2017 **91**

List of Figures

1. eRASS and *XMM-Newton* X-ray images of HESS J1731-347 11
2. Extraction regions for total remnant and background spectrum. 13
3. Match of point sources in eRASS 1 to 4 catalogs with the source region. 15
4. Source spectrum, background spectrum and background subtracted spectrum. 17
5. Background spectra extracted from the left and right half of the background annulus. 19
6. Best-fitting models of the background subtracted fits using the background spectrum extracted from different regions. 19
7. Contour plot and interval projection plot for the background subtracted fit. 21
8. Filter wheel closed data for all 7 telescope modules of eROSITA. 24
9. Best-fitting model for the spectrum extracted from the background annulus. 30
10. Best-fitting models for the source region spectrum with background model parameters frozen to the best-fitting values for the background region and a frozen (red) and thawed (blue) absorption and photon index. 32
11. Best-fitting models for the source region spectrum with thawed background model parameters and a frozen (red) and thawed (blue) photon index. 33
12. Background model re-fit with the temperatures and normalizations of the thermal cosmic X-ray background components frozen to the best-fitting values of the source region fit. 34
13. Source and background region spectra for all 7 TMs and only those possessing an on-chip filter, i. e. TM12346. 35
14. Source and background region spectra and best-fitting models for the simultaneous fit of both data sets. 38
15. Comparison of the best-fitting source and background region models for a frozen and thawed photon index. 38
16. Contour plots for the simultaneous fit of the source and background region spectrum. 39
17. Model components for the best-fitting source model of the simultaneous fit. 40
18. Over-plot of the 1σ, 2σ and 3σ contours of the absorption column density and the photon index for background subtraction and background modelling. 41
19. Best-fitting models for the source region spectrum from the simultaneous source and background region fit when excluding the CCO from the source region with different exclusion radii. 43
20. Definition of the sub-regions for the spatially resolved spectral analysis. 45
21. Color map visualization of the N_H gradient across the SNR with frozen photon index. 47
22. Two figures from H. E. S. S. Collaboration et al. (2011) that indicate the presence of a molecular cloud in front of the western part of HESS J1731-347. 48
23. Independent, best-fitting N_H values for all 30 sub-regions included in the fit with frozen photon index. 50
24. Deviations between independent N_H values and linear gradient model. 52
25. Plot of independent and linked N_H values as a function of the region number, including uncertainties to assess the significance of the differences. 53
26. Differences in the normalization of the remnant power law for the source regions for linked and independent N_H. 53
27. Visualization of the N_H and Γ_{SNR} gradients. 55
28. Visualization of the independent N_H values and the Γ_{SNR} gradient for the N_H independent, Γ_{SNR} linked fit. 57
29. Comparison of the independent N_H values obtained from the fit with a frozen photon index from the fit with a linked photon index. 59
30. Comparison of N_H and Γ_{SNR} values obtained from fits with different linking relations. 61

31. Comparison of two pairs of sub-region spectra, where the orange ones are extracted from the eastern part of the remnant and the blue ones from the eastern part. There are clear differences in the count rate decrease from east to west for different energy ranges. 61
32. Left panel: N_H values from the eRASS:4 data analysis for the 18 source and 3 background regions defined by Doroshenko et al. (2017). Right panel: *XMM-Newton* results from Doroshenko et al. (2017). 63
33. Comparison of N_H values obtained from eRASS data for the regions defined by Doroshenko et al. (2017) with the results of their analysis. 63
34. Color map visualization and plot of the photon index values obtained for fixed absorptions for the regions defined by Doroshenko et al. (2017). 65
35. Estimated photon index gradient uncertainties for simulated eROSITA spectra with larger exposure. 69
36. Estimated absorption gradient uncertainties for simulated eROSITA spectra with larger exposure. 69
A1. Plot of source and background spectra of the 7 TMs and best-fitting models for different instrumental background models. 81
B1. Two different background annuli and corresponding spectra. 82
C1. Source and background region spectrum best-fitting models for the simultaneous fit of both data sets, using only data of TM 12346. 84
D1. Best-fitting source region model with frozen and thawed photon index for the left and right half background annulus spectrum. 84
D2. Best-fitting model for the left and right half annulus background spectrum. 85
D3. Background models for the left half annulus and right half annulus after the source region fit. 86
E1. Best-fitting models of five example regions for a simultaneous fit of all 30 regions with constant and linked N_H. 87
F1. Best-fitting models for all 30 sub-regions from the simultaneous fit with different N_H and Γ linking relations. 89
G1. Spectra and best-fitting models for the 22 regions defined by Doroshenko et al. (2017). 92

List of Tables

1. Best-fitting values and 1σ confidence bounds for the source model parameters in the background subtracted fit. 20
2. Best fitting parameters for the background fit. 30
3. Best-fitting parameters for the source region spectrum with the background parameters frozen to the results of the background region fit. 31
4. Best-fitting parameters for the fits of the source region spectrum with thawed background model parameters. 33
5. Best-fitting parameters for the simultaneous fit of the source and background region spectrum. 41
6. Best-fitting parameters for the N_H gradient fit with Γ_{SNR} = 2.66 frozen. 49
7. Best-fitting parameters for the fit of the 30 sub-regions considered in the analysis with independent N_H values and a frozen photon index of 2.66. 51
8. Best-fitting parameters for the simultaneous fit of the spectra of the 30 sub-regions shown in Fig. 20 with both N_H and Γ linked by a 2-d gradient relation each between individual regions. 54
9. Best-fitting parameters for the simultaneous fit of the spectra of the 30 sub-regions shown in Fig. 20 with independent N_H and linked Γ_{SNR}. 58

10. Fit results using eRASS:4 data for the 22 regions defined by Doroshenko et al. (2017) when fixing the photon index to 2.66 for all regions. 64
11. Photon index and power law normalization results for the 22 regions defined by Doroshenko et al. (2017) when fixing the absorption for each region to their analysis result. 66
A1. Best-fitting source model parameters for different instrumental backgrounds. 79
B1. Results of background-subtracted fit for different background annuli. 82
C1. Best-fitting parameters for the simultaneous fit of the source and background region spectrum, using only the data of TM12346. 83
D1. Best-fitting parameters of the simultaneous source and background region fit for the left half annulus background. 85
D2. Best-fitting parameters of the simultaneous source and background region fit for the right half annulus background. 86

1. Introduction

1.1. Supernovae

A supernova marks the end of a star's lifetime. These events can be divided in two major categories: thermonuclear supernovae and core-collapse supernovae. A thermonuclear supernova, or type Ia supernova, occurs when a White Dwarf in a binary system accretes matter from its companion star and consequently exceeds the Chandrasekhar mass limit. This limit is about $1.4\,M_\odot$ and corresponds to the maximum mass that can be stabilized by degenerate electron pressure against gravity. Thus, White Dwarfs heavier than the Chandrasekhar mass collapse in a type Ia supernova. These events play an important role in distance determination: They are *standard candles*, meaning that their intrinsic brightness is uniform and well constrained. Therefore, their distance can be determined from the observed brightness.

Thermonuclear supernovae do not leave behind a compact object such as a Neutron Star or a Black Hole. This is an important characteristic that distinguishes them from the second category: core collapse supernovae. Such events occur when stars more massive than about $8\,M_\odot$ reach the point where iron starts to form through nuclear fusion in their core. At this point, their energy supply is nearly exhausted, since iron is the chemical element with the highest binding energy and therefore it cannot be processed further to release energy through nuclear fusion. As a consequence, the radiation pressure within the star decreases and is no longer able to stabilize the star against its own gravity. The star is no longer in hydrostatic equilibrium and starts to contract. The iron core becomes denser and is consequently stabilized by the pressure of the degenerate electron gas. When the core does not reach a mass greater than the Chandrasekhar limit ($\sim 1.4\,M_\odot$), the star ends up being a White Dwarf. Exceeding this limit, it can no longer be stabilized by the degenerate electron pressure and collapses. Then, it forms a proto-neutron star or a black hole if it is more massive than the Oppenheimer-Volkoff limit (about $1.5 - 3\,M_\odot$). During the collapse, a large amount of gravitational energy is set free, $E \gtrsim 10^{53}$ erg (e. g. Cioffi et al. 1988, Vink 2012). As a comparison, this is many orders of magnitude higher than the total energy radiated by the Sun that hit our Earth during its entire lifetime of ~ 4.5 billion years: $E_{\rm tot} \sim 10^{35}$ erg.[1]

The reason for the massive energy release during a core collapse is that the star contracts rapidly from its former size to that of a neutron star which is much smaller, $R_{\rm NS} \sim 10^4$ m. A major part of this released energy is carried by neutrinos, namely on the order of 10^{53} erg. The fraction released as kinetic energy, i. e. in the form of the matter from the outer layers of the progenitor star that are ejected during the supernova explosion, is two orders of magnitude lower $\sim 10^{51}$ erg. When the stellar core has formed a compact object, the contraction of the star comes to a sudden end and a shock wave forms as the infalling material from further out hits the dense matter of the compact object and is reflected outwards. However, numerical simulations have shown that this shock wave cannot drive the supernova explosion without further energy input. The exact mechanism how the released gravitational energy is used to drive the supernova explosion is still a matter of ongoing research. Different theories have been tested in simulations, for example the one that the shock wave absorbes some of the gravitational energy carried by the neutrinos and therefore keeps expanding (Janka et al., 2007).

Supernovae play an important role in the evolution of the Universe and influence the properties of stellar populations: They enrich the interstellar medium with heavy elements formed through nuclear fusion during the lifetime of the star. As a consequence, with the increasing age of the Universe

[1] The calculation is based on the approximation that the Sun radiated away the same amount of energy per unit time as it does right now during the Earth's entire lifetime. Further, the distance between Sun and Earth is assumed to be constant, as well as the Radius of the Earth. Solar constant: $S_0 \approx 1.36 \cdot 10^{10}\,{\rm erg}/({\rm m^2 s})$; Earth radius $R_E \approx 6.4 \cdot 10^3$ m $\implies E_{\rm tot} = S_0 \cdot \pi R_E^2 \cdot (4.5 \cdot 10^9 \cdot 365 \cdot 24 \cdot 3600)\,{\rm s} \approx 2.5 \cdot 10^{35}$ erg

(corresponding to a larger number of supernova incidents), metal-rich stars can form which were not present in the early Universe. Since planet formation is much more efficient in a metal-rich environment, which is indicated by the fact that planets occur more frequently around metal-rich stars (e. g. Wang and Fischer 2015), supernovae also contribute to the formation of planetary systems and therefore of (potentially) habitable worlds in the Universe.
What is left of the star after the supernova explosion is not only the compact object (in the case of a core-collapse supernova) but also the ejected former stellar material that is expanding into the interstellar medium and can emit radiation at a wide wavelength range from γ-rays over X-rays to radio wavelengths. This expanding accumulation of matter is called the *supernova remnant* (SNR). Analysing the X-ray spectrum of such an object, namely HESS J1731-347, is the purpose of this Master Thesis work. The main goal is to examine the spectra of several sub-regions in order to trace variations of the spectral parameters across the remnant.

1.2. Supernova remnants

In the following, the key properties of supernova remnants are summarized. This section is based on a review on the topic, written by Vink (2012).

1.2.1. Classification

Since it is not straight-forward in many cases to infer the category of the supernova that left behind a particular SNR, it is commmon to categorize SNRs on the basis of their morphology. There are four major groups: *shell type SNRs*, *plerions*, *composite SNRs* and *mixed morphology SNRs*. The outstanding characteristic of a shell-type SNR is, as the name suggests, a shell-type morphology with bright emission especially at the outer bounds where the expanding matter forms a shock wave and is heated from interactions with the interstellar medium. In contrast, plerions do not have a shell. Instead, they exhibit bright emission in the center. This is caused by a shock originating from plasma acceleration due to the relativistic particle wind generated by a rapidly rotating neutron star in the center of the plerion. Therefore, they are also called *pulsar wind nebulae* (PWN). They fall within the category of SNRs, even though the shock is not driven by the supernova explosion but by the wind of the rotating neutron star.
Composite SNRs combine the characteristics of the previous two types: They consist of a pulsar wind nebula emission in the center, as well as radiation from the outer shell. An early example for a composite SNR in the literature is G326.3-1.8, for which radio observations indicating a composite structure have been analysed by Milne et al. (1979).
The fourth type, mixed morphology SNRs, shows deviating characteristics when observed in different wavelength ranges: In X-rays, these objects are bright at the center, resembling a plerion. However, the central emission is not generated by a pulsar wind, but it is thermal emission produced by interactions of the expanding matter. This is a key difference between mixed-morphology and composite SNRs. In the radio regime, mixed morphology SNRs exhibit a shell-type morphology. They were proposed by Rho and Petre (1998) to form a separate class of SNRs next to the other three discussed above.
The SNR analysed in this Thesis, HESS J1731-347, is a shell-type SNR.

1.2.2. Evolutionary phases

In general, the evolution of an SNR is driven by the interaction of the ejected former stellar matter with the ISM. As they evolve with time, SNRs go through four different evolutionary phases (Woltjer, 1972). However, since they are extended objects and their surroundings are not necessarily homogeneous, the transition from one phase to the next is not always clearly recognizable. Different parts of an SNR can be in different evolutionary phases.

As a starting point of the SNR evolution, the supernova explosion leaves behind a density disturbance which is propagating faster than the speed of sound in the local medium. Therefore, a shock front is formed at the boundary where the expanding ejecta encounter surrounding material. The exact expanding behaviour of an SNR depends on the mass of the progenitor star on the one hand and on the structure of the surrounding medium on the other hand. During the lifetime of the progenitor star, its stellar wind can induce a region of lower density around the star. At the beginning of its evolution, the SNR expands into this lower-density circumstellar matter (CSM). At this stage, the shock speed is slowed down less than later when the remnant is expanding into the denser interstellar medium (ISM), e. g. Berezhko and Völk (2008).

In the first evolutionary phase, called the *ejecta-dominated phase*, the emission of the SNR predominantly comes from the matter ejected during the supernova explosion, i. e. the matter that the progenitor star was composed of or, to be precise, including the elements this matter was transformed to in the course of the supernova. The mass of this ejected matter is also larger than that of the swept-up matter. The age at which young SNRs transition to the second evolutionary phase, the *Sedov-Taylor phase*, depends on many parameters such as the density of the surrounding medium and the mass of the progenitor star. Therefore, only a rough estimate can be given which is on the order of few 100 yr, e. g. Woltjer (1972), Table 4 or Truelove and McKee (1999), Table 1. In the Sedov-Taylor phase, the mass of the interstellar and circumstellar matter swept up by the expanding SNR shock has gotten larger than the mass of the ejected stellar matter. Still, energy loss by radiation makes up only a negligible fraction of the total energy loss. Radiative cooling becomes important as a loss mechanism only in the third evolutionary stage, the *pressure-driven snow plough phase*. However, this does not mean that no radiation is observed from SNRs in the first two phases.
The fourth and last step in the evolution of an SNR is its merging with the ISM. In this phase, a sufficient amount of energy has been transferred from the remnant to the ISM that the originally high expansion speed and temperature of the ejected and swept-up matter have adapted to the properties of the surroundings. Thus, the SNR loses its characteristic features which distinguished it from the interstellar matter around it and is merging with it. The mechanisms through which energy in form of radiation is released from the SNR and supplied to the ISM are described in the following Sect. 1.2.3, along with the characteristics of the corresponding emission.

1.2.3. Radiation processes of SNRs

One reason why SNRs are interesting objects to study is that they are believed to be one of the main sources of galactic cosmic rays (CRs). These highly energetic rays consist of protons and heavier nuclei (and to a small fraction $\sim 1\%$ also electrons and positrons) which are accelerated to relativistic velocities. The cosmic sources of this acceleration are subject to current research, including for example measurements with the Alpha Magnetic Spectrometer (AMS, Kirn 2022) at the International Space Station (ISS).
Besides potentially accelerating cosmic rays, SNRs release energy in form of electromagnetic radiation and transfer kinetic energy to the ISM by heating it. Since the focus of this Thesis work is to analyse the X-ray spectrum of the SNR HESS J1731-347, the main attention in the following paragraphs describing radiation production mechanisms in SNRs will lay on the X-ray regime. In general, the radiation production in SNRs is determined by the interaction of matter accelerated during the supernova explosion and the swept-up circumstellar and interstellar matter in the surroundings. The high kinetic energies that particles carry from the explosion and additionally gain through acceleration at the shock front enable a number of mechanisms to generate electromagnetic radiation with various characteristics. In general, one distinguishes between two types of radiation: Thermal radiation on the one hand, which is emitted by any matter that has a temperature greater than 0 K and has characteristics that are essentially shaped by the temperature of the medium. On the other hand, there is non-thermal radiation which originates from processes that are not related to the thermal energy of the matter.

One important difference between thermal and non-thermal radiation is the velocity distribution of the particles that produce the radiation. Since this velocity distribution influences the energy distribution of the radiated photons, the same physical process, e. g. the deceleration of electrons in an electric field, can produce emission with either a thermal or a non-thermal spectrum. If particle velocities follow the Maxwell-Boltzmann distribution, the resulting radiation has a thermal spectrum, while for velocities distributed as a power-law, the spectrum is non-thermal. For the special case that radiation and matter are in thermodynamic equilibrium, a thermal spectrum can be modelled as a black body using the Planck function. Non-thermal emission, on the other hand, can be described by a power law, meaning that the flux density of photons as a function of the energy, $A(E)$, can be described by an exponential function:

$$A(E) = KE^{-\Gamma} \tag{1}$$

where Γ is the dimensionless photon index and K is the normalization constant. When considering non-thermal X-ray radiation, this normalization constant is commonly given in units of photons/keV/cm^2/s at an energy of 1 keV.[2] Thus, the larger Γ, the more rapidly the flux decreases for higher energies, meaning that the spectrum becomes softer. The power law given in Eq. 1 is specifically used to model non-thermal X-ray emission. Since up to now, no thermal X-ray emission was detected from the SNR HESS J1731-347, Eq. 1 will be used in the analysis to model the emission of the source (additionally considering the absorption).

For completeness, the ways to produce thermal X-ray emission are also discussed here briefly: The most prominent mechanism are free-free interactions of charged particles. If for example an electron moves in the electric field of an ion, it experiences the Coulomb force and emits *bremsstrahlung* since it is decelerated by a force that acts parallel to its direction of motion. Additional mechanisms to produce thermal radiation are free-bound interactions, i. e. a free electron is captured by an ion, and two-photon emission, where an electron de-excites from a meta-stable quantum state by emitting two photons. All these mechanisms can produce continuum thermal X-ray emission. Besides that, sharp emission lines, which are also of thermal nature, are caused by ions excited in electron-ion collisions when they transition back to the ground state.
As mentioned above, the X-ray spectrum of HESS J1731-347 has been characterized so far as purely non-thermal. Therefore, the mechanisms producing non-thermal X-ray emission in SNRs will be described a little more detailed than the thermal radiation mechanisms in the following. One form of non-thermal radiation can be bremsstrahlung, which has already been described above since it can also be of thermal nature, depending on whether the velocity distribution of the decelerated particles follows the Maxwell-Boltzmann distribution or not.
Other mechanisms to produce non-thermal X-ray emission are related to charged particles moving in a magnetic field and being accelerated by the Lorentz force, which is perpendicular to their direction of motion. If the charged particles are moving at non-relativistic velocities, they emit cyclotron radiation. In the case of relativistic speed, synchrotron radiation is produced. The latter is believed to be the predominant process through which non-thermal X-ray emission is generated in SNRs. Synchrotron radiation is not restricted to X-ray wavelengths, but can be emitted in a wide range, starting at the radio band and possibly extending to highly energetic GeV Gamma-rays. The X-ray spectra resulting from synchrotron radiation in young SNRs can be described by a power law (see Eq. 1) with photon indices in the range of $\Gamma = 2 - 3.5$. The production of synchrotron radiation requires charged particles moving at significant fractions of the speed of light. The process through which they gain these high kinetic energies is called *diffusive shock acceleration*. It is a first order Fermi process which generally is based on charged particles being trapped at the front of a blast wave, in this case the shock front of the expanding SNR. At both ends of this front, turbulent magnetic fields restrict the motion of the charged particles which leads to repeated elastic reflections. Bouncing back and forth in this setting, particles can be accelerated to relativistic velocities. The maximum kinetic energy they can gain through diffusive shock acceleration is influenced by the shock expansion velocity. This means that a

[2] `https://heasarc.gsfc.nasa.gov/xanadu/xspec/manual/XSmodelPowerlaw.html`, accessed 2022-08-10

slower expanding shock leads to a softer X-ray synchrotron spectrum since the maximum energy of the electrons is lower and therefore also the maximum frequency of the synchrotron photons. However, the maximum velocity of charged particles is not only determined by the shock propagation speed. There are two other limiting factors: First, the time during which particles can be accelerated at the shock front, which is related to the age of the SNR (age-limited case). From this point of view, the X-ray spectrum would be expected to become harder with increasing age of the SNR since electrons would steadily gain more kinetic energy. However, their maximum velocity is also limited by continuously ongoing loss processes, in particular radiative cooling. This is the so-called loss-limited case: While moving in the magnetic field of the SNR, electrons lose energy by emitting synchrotron radiation. At higher velocities, they cool faster, so that above some threshold, energy is radiated away just as fast as it is gained through acceleration. Therefore, there cannot be electrons with energies above this threshold, which also implies a cutoff energy in the synchrotron spectrum.
For the loss-limited case, which dominates over the age-limited case after the SNR has reached a certain age, the maximum frequency $\nu_{\rm max}$ of emitted synchrotron photons depends on the expansion velocity $v_{\rm shock}$ as $h\nu_{\rm max} \propto (v_{\rm shock}/5000\,{\rm km/s})^2$ keV (Vink, 2012).
The same relativistic electrons that are responsible for X-ray synchrotron emission can also produce high-energy γ-rays by transferring energy to photons through inverse Compton scattering. This is the so-called *leptonic scenario* for γ-ray production in SNRs. An alternative possibility for the origin of TeV emission is the *hadronic scenario*: A pair of γ-ray photons is produced through the decay of a neutral pion (π^0) which originates from collisions of high-energy nuclei (hadrons). This scenario requires that not only electrons but also nuclei are accelerated efficiently at the shock front, which might not be the case. The two origin scenarios for γ-ray emission are mentioned here briefly since it is a topic of ongoing research to disentangle their contribution if such highly energetic radiation is detected from an SNR. Observations in other wavelength ranges, thus also in the X-ray regime, can provide important information in this context since it strongly depends on the properties of the surrounding medium how efficient both mechanisms operate. The hadronic scenario is based on collisions, thus its efficiency grows in regions with higher density. These areas show a higher absorption than low-density regions, which can be constrained – amongst other methods – through X-ray spectral analysis.
To sum up, diffusive shock acceleration of electrons to relativistic velocities in SNRs enables the production of X-ray synchrotron emission and higher energy emission through inverse Compton scattering. Besides that, it is also believed to be responsible for cosmic ray acceleration (e. g. Bell et al. 2013), i. e. relativistic particles themselves escaping from the remnant. Therefore, studying X-ray and γ-ray radiation from SNRs allows to draw conclusions on the origin of cosmic rays, since the underlying particle acceleration mechanism is the same. This makes the research in this field particularly interesting.

1.2.4. HESS J1731-347

The SNR analysed in this Thesis, HESS J1731-347, was first detected in TeV γ-rays with the High Energy Stereoscopic System (HESS), a Cherenkov Telescope located in Namibia, during its Galactic Plane Survey (The H. E. S. S. Collaboration 2007, Aharonian et al. 2008). X-ray observations of the source region with the ROSAT telescope (Truemper, 1982) have been consulted by Aharonian et al. (2008) to identify possible X-ray counterparts. Tian et al. (2008) discovered a faint radio and X-ray source with a shell-type morphology, G353.6-0.7, in spatial coincidence with the HESS source. They claimed G353.6-0.7 to be an old SNR, given its size and the faint X-ray emission, and to be the radio and X-ray counterpart of HESS J1731-347. In the course of this discovery, they modelled the ROSAT X-ray spectrum of the source with a thermal model. At this stage, the insights to the properties of the X-ray counterpart were strongly limited by low counting statistics.
After its first detection in TeV γ-rays, the source was observed again with HESS in 2007 and 2009 to more thoroughly investigate its morphology in this wavelength range (H. E. S. S. Collaboration et al., 2011). The corresponding study confirmed the association of the radio and X-ray emitting SNR

G353.6-0.7 with the TeV source HESS J1731-347. To better constrain the properties of the X-ray counterpart, follow-up observations have been conducted with several X-ray observatories, namely *Chandra*, *XMM-Newton* and *Suzaku*. Tian et al. (2010) analysed *XMM-Newton* and *Suzaku* observations from 2007. Bamba et al. (2012) also studied the *Suzaku* data, including the observation of 2007 and a later one from 2010, covering an additional part of the remnant. Still, no complete coverage in X-ray observations was achieved at this point. The first study having access to X-ray observations that cover the whole remnant was the one of Doroshenko et al. (2017) who used several *XMM-Newton* data sets obtained between 2007 and 2014 with a total observation duration of 314 ks. The effective exposure is $\sim$ 240 ks for the EPIC MOS1 camera, $\sim$ 250 ks for MOS2 and $\sim$ 100 ks for EPIC PN. This is the total exposure of all observations, which covered different parts of the remnant. Thus, the exposure is not uniform across the source (see Fig. 2 middle of Doroshenko et al. 2017). Nevertheless, these observations provide excellent counting statistics. This is indicated by the fact that the authors extracted 167 spectra with an average exposure of 42 ks for their 22 sub-regions from the different observation campaigns.

The X-ray emission of the remnant was so far characterized as purely non-thermal in all studies (except Tian et al. 2008 who fitted the ROSAT spectrum with a thermal model in the very first attempt), i. e. the spectrum is well represented by an absorbed power law. The search for thermal emission from the source, e. g. by Bamba et al. (2012), did not yield any detections at a significant level.

Since the remnant has a shell-type morphology in both the radio and X-ray band (e. g. Tian et al. 2008), it is classified as a shell-type SNR. The fact that it emits in the high-energy TeV regime makes HESS J1731-347 particularly interesting to study since this is only the case for a limited number of shell-type SNRs: Currently, only 14 of them are listed as high-energy γ-ray sources in the TeVCat[3] (Wakely and Horan, 2008), an online Catalog listing γ-ray sources with energies > 50 GeV. The TeV emission of these remnants is a sign that they are capable of accelerating particles to relativistic energies. Thus, they are potential sources of cosmic rays (see Sect. 1.2.3), which makes them interesting objects of research.

The fact that a central compact object (CCO) is located within HESS J1731-347 (e. g. Acero et al. 2009, Tian et al. 2010) allows the conclusion that the remnant originated from a core-collapse supernova. The X-ray spectrum of the CCO has been analysed in several studies, e. g. Tian et al. (2010) and Klochkov et al. (2013). The latter conclude that the object is likely to be a neutron star (NS), covered by a carbon atmosphere since the fit results for a simple black body model enforce a distance of $\sim$ 30 kpc which considerably exceeds all current estimates for the SNR (see below). Landstorfer et al. (2022) confirmed the presence of a dust-scattering halo around the CCO which was suspected to be present already by Halpern and Gotthelf (2010) based on the *Chandra* image of the source. Doroshenko et al. (2016) analysed the optical and infrared emission of a second star located at an apparent separation of $25''$ to the CCO and came to the conclusion that the two sources have possibly formed a binary system earlier in their evolution which was then disrupted by the supernova explosion. Studies searching for pulsations of the CCO yielded no result so far (e. g. Tian et al. 2010, Klochkov et al. 2013, Doroshenko et al. 2022), suggesting that the NS is emitting radiation uniformly across its surface. (Or, alternatively, that the direction of an eventual beam is nearly parallel to the NS's rotation axis.) Doroshenko et al. (2022) constrained the mass and radius of the CCO from X-ray spectral analysis and the *Gaia* distance, finding that it is either the lightest neutron star known up to date or a different kind of object (i. e. a 'strange star' candidate).

The SNR HESS J1731-347 has a diameter of about $30'$ as seen in the radio regime (Tian et al. 2008). Until recently, unambiguously constraining its distance was a matter of ongoing research. Doroshenko et al. (2017) argue that the TeV emission observed from the remnant makes it unlikely that it has a distance beyond that of the galactic center ($\sim$ 8.5 kpc). Given that the apparent brightness of an object decreases with increasing distances (for an unchanged intrinsic luminosity), if the SNR was located farther away, the TeV emission would have to be intrinsically very bright. Doroshenko et al. (2017) consider it likely that the remnant is located in one of the three galactic spiral arms that cross the

[3]`http://tevcat2.uchicago.edu/`, accessed 2023-01-18

line of sight in front of the galactic center (i. e. the Scutum-Crux arm, which would imply a distance ~ 3 kpc, the Norma arm corresponding to $d \sim 4.5$ kpc or the 3 kpc arm, meaning d $\sim 5-6$ kpc). The assumption that it is located within a spiral arm of the Milky Way is based on the fact that the number of massive stars per unit volume and therefore also of core-collapse supernova progenitors is higher there, thus the probability for a type II supernova event is increased (e. g. H. E. S. S. Collaboration et al. 2011). Tian et al. (2008) give a likely distance of 3.2 kpc for HESS J1731-347 which they inferred from a spectral analysis of the compact HII region G353.42-0.37. The region is spatially coincident with the remnant. This distance estimate for HESS J1731-347 involves the assumption that the HII region is actually (i. e. in 3-d space) next to the remnant and that the alignment is not just a 2-d projection on the celestial sphere. Tian et al. (2008) argue that bright HII regions are found in the vicinity of several HESS sources which might suggest an association rather than a series of chance projections. H. E. S. S. Collaboration et al. (2011) derived a lower limit of 3.2 kpc for the distance of the remnant by comparing the absorption obtained from X-ray spectral fitting of *XMM-Newton* data to ^{12}CO and HI maps of the same sky region. These maps indicate the amount of absorbing matter when integrating over a particular distance. Maxted et al. (2018a) performed a similar analysis using CO data of the Mopra Galactic Plane CO survey and HI data from the Southern Galactic Plane Survey. They concluded that the absorption derived from X-ray spectral analysis of HESS J1731-347 is consistent with the CO and HI observations only until the Scutum-Crux arm, but not for larger distances, thus supporting a distance of ~ 3.2 kpc for the remnant. Also Klochkov et al. (2013) state that their spectral analysis of the CCO with a carbon atmosphere model is consistent with a distance of 3.2-4.5 kpc. A more recent analysis of Klochkov et al. (2015) comes to the conclusion that spectral modelling involving a carbon atmosphere favours a distance of ~ 3 kpc over 4.5 kpc, while distances larger than $\sim 5-6$ kpc are incompatible with the data under the assumptions made by the authors. The most accurate and probably most reliable distance estimates are derived in two recent studies already mentioned above that also dealt with the CCO at the center of the remnant: Landstorfer et al. (2022) obtained a distance of 2.79(62) kpc for the CCO. Doroshenko et al. (2022) used a distance of 2.5(3) kpc in their analysis, which was derived from the *Gaia* parallax of the CCO's optical counterpart by Bailer-Jones et al. (2021). These two values suggest that the actual distance of the remnant is somewhat below 3 kpc.

Assuming a distance of 3.2 kpc, the angular diameter of $0.5°$ of the source in the radio band corresponds to a physical diameter of ~ 28 pc (Tian et al. 2008).

Cui et al. (2016) simulated the evolution of HESS J1731-347 assuming different masses for the progenitor star, ranging from $8\,M_\odot$ to $25\,M_\odot$. They came to the conclusion that the remnant is most likely still expanding into the low-density bubble carved by the stellar wind of the progenitor star while it was in the main sequence phase. This scenario provides an explanation how the remnant could have achieved its current size in a considerably shorter time period than it would have needed when expanding into a denser environment. Therefore, the classification as an old SNR by Tian et al. (2008) is not a necessary consequence of the large size of the remnant, given that in the meantime an alternative evolution scenario has been suggested.

There are two HII regions present in the surroundings of the SNR, both in western direction, which are seen in radio observations (H. E. S. S. Collaboration et al. 2011). The more distant HII region is in spatial coincidence with an extended TeV γ-ray source, HESS J1729-345. Additionally, ^{12}CO emission indicates the presence of a molecular cloud in the western vicinity of the remnant. The HII region that coincides with the TeV source HESS J1729-345 might be associated with this molecular cloud according to the distance estimates of (H. E. S. S. Collaboration et al., 2011). Cui et al. (2016) found that the γ-ray spectrum of HESS J1729-345 could be produced by cosmic rays escaping from HESS J1731-347 through their interaction with the molecular cloud. Cui et al. (2019) further investigated the interaction and possible collision of the SNR with the nearby cloud. They conclude that the GeV and TeV emission observed from the cloud can be explained by cosmic rays set free in a collision scenario with the remnant. However, for the observed GeV emission, the collision scenario is not necessarily the dominating origin. Maxted et al. (2018b) made use of CO and CS observations to draw conclusions on the structure of the matter surrounding HESS J1731-347. Their analysis also supports the theory that the emission observed from molecular clouds in the vicinity might be caused by cosmic rays escaping from the remnant.

As already mentioned in Sect. 1.2.3, observations in X-rays are also an important method to address these questions since they reveal information about the structure of the surrounding medium of an SNR. In the case of HESS J1731-347, the absence of thermal X-ray radiation allows to determine a general upper limit for the density of the environment (H. E. S. S. Collaboration et al., 2011). Besides, the X-ray surface brightness of the SNR varies strongly: The western half is dimmer than the eastern, as reported by Doroshenko et al. (2017). The absorption column density that these authors found from their spatially resolved spectral analysis of *XMM-Newton* data is higher in the less luminous parts, so the brightness decrease is partly related to absorption. However, Doroshenko et al. (2017) calculated the intrinsic surface brightness of the remnant (see their Fig. 10) and found that a dimming towards the western part is also present there, independent of absorption variations. They argue that the decrease of intrinsic X-ray brightness of the remnant is an indication for interaction with dense matter in its surroundings, i. e. a molecular cloud that in fact is present in the western vicinity, as discussed above. If the remnant is indeed interacting with the cloud, the shock expansion velocity is expected to be slowed down faster in the region of interaction than elsewhere. As mentioned in Sect. 1.2.3, this implies a lower maximum energy of the electrons and therefore also a lower cutoff energy of the synchrotron emission spectrum. Thus, X-ray spectra become softer, until for even lower expansion velocities synchrotron radiation is only emitted at longer wavelengths outside the X-Ray regime. This is a possible explanation for the decreasing X-ray brightness in the western part of HESS J1731-347 under the assumption that the remnant is indeed interacting with the molecular cloud in this area and its expansion in that direction is slowed down as a consequence of the interaction. The fact that there is no dimming observed towards the western part of the source in the lower-energy radio band is in agreement with this theory: This frequency range would not be affected by the lower cut-off in the synchrotron radiation caused by a slower shock expansion speed. Also in the high-energy TeV band, no brightness decrease in western direction is observed for HESS J1731-347 (H. E. S. S. Collaboration et al., 2011). In that case, the explanation suggested e. g. by Cui et al. (2019) is that the TeV emission from the remnant can be divided into a contribution of the leptonic scenario from the X-ray bright parts and one of hadronic origin from the X-ray dim parts where the shock speed is too low to drive γ-ray production through inverse Compton scattering, but at the same time, the high density raises the probability of hadron collisions.

1.3. The eROSITA telescope

eROSITA stands for *extended ROentgen Survey with an Imaging Telescope Array* and is an X-ray telescope aboard the Spectrum-Roentgen-Gamma mission (SRG). SRG is a Russian-German cooperation and was launched on July 13, 2019. eROSITA was developed under the lead of the Max Planck Institute for Extraterrestrial Physics Garching (MPE) with contributions by IAAT in electronics, background simulations and proton reflection of the mirrors.[4] Next to eROSITA, SRG hosts a second telescope, the ART-XC (Astronomical Roentgen Telescope X-ray Concentrator), which is more sensitive towards high energies and was developed under the responsibility of the Russian Space Research Institute (IKI, Pavlinsky et al. 2018). The sky is divided in two equally sized hemispheres for which the eROSITA observations are accessible only for the German and only for the Russian consortium members, respectively. SRG is orbiting the Lagrange point L2 of the Sun-Earth system in a 6-months halo orbit.

[4]https://uni-tuebingen.de/en/faculties/faculty-of-science/departments/physics/institutes/astronomy-astrophysics/astronomy-hea/research/prof-santangelo-high-energy-astrophysics-group/participation-to-experiments/erosita/

Originally, the prime goal of the mission was to perform 8 all-sky surveys, i. e. to repeatedly scan the entire sky for X-ray sources in eRASS1 to 8, where eRASS stands for *eROSITA All-Sky Survey*. eRASS1 started on December 11, 2019 after a Calibration and Performance Verification (Cal-PV) phase which included the eROSITA Final Equatorial Depth Survey (eFEDS). Each eRASS takes ~ 6 months. After the completion of eRASS8, the plan was to continue operating eROSITA in pointed ovservation mode, i. e. particularly interesting sources should be monitored with a greater exposure. However, as a consequence of the war against Ukraine that the Russian president Wladimir Putin started on February 24, 2022, all co-operations with Russia were put on hold also in the scientific context. Therefore, eROSITA was put into safe mode on February 26, 2022, roughly 2 months after the beginning of eRASS5, meaning that no more scientific data is recorded. Thus, the original schedule, according to which eRASS8 should have been completed roughly in December 2023, cannot be realized any more. As of today (January 2023), eROSITA is still in safe mode and it is uncertain, if or when scientific operations can be resumed. However, the data of the first for all-sky surveys can still be exploited and offer interesting insights to the X-ray view of the Universe.

Before eROSITA, the ROSAT satellite (Truemper, 1982) which was launched on June 1st, 1990 also performed an X-ray all-sky survey. Adding up the counts of all 8 eRASS surveys – if they will be completed – the observations are expected to be 25 times more sensitive than those of the ROSAT all-sky survey (RASS) in the soft energy band (0.2-2.3 keV). Also, ROSAT was only sensitive to energies up to ~ 2 keV. There have been comprehensive surveys observing in higher energy ranges, for example INTEGRAL and EXOSAT, but eROSITA is providing a greater sensitivity and the first complete all-sky survey in the hard X-ray regime.

1.3.1. Instrumental properties

The summary of the instrumental properties given in this section is based on Predehl et al. (2021). The total eROSITA telescope has a diameter of ~ 1.9 m and a height of ~ 3.2 m and weighs 808 kg. It comprises 7 mirror assemblies, each connected to its own camera assembly, forming the 7 telescope modules (TMs) of the instrument. The field of view (FOV) of the telescope has a diameter of 1.03° and is monitored simultaneously by all 7 TMs. In the survey mode, the satellite rotates with a period of approximately 4 hours around its own axis and thereby scans one ‘stripe’ of the celestial sphere. Then, the observing direction is shifted by approximately $10'$ and the next ‘stripe’ is scanned. The angular resolution of eROSITA is $\approx 18''$ in the on-axis direction and on average $\approx 26''$ over the entire field of view.

Each mirror assembly consists of a Wolter I configuration, i. e. a combination of a parabolic and a hyperbolic mirror. Incoming photons are reflected two times, once at each mirror, and in this way the radiation is focused. In this configuration, photons coming from outside the field of view and therefore having large incoming angles can reach the focal point after a single reflection at the hyperbolic mirror only. Since their path inside the mirror assembly is different from that of a double reflected photon originating from the field of view, their position of origin cannot be reconstructed correctly. This phenomenon can lead to strong systematic features in the image if a bright source is next to the field of view, which is called stray light contamination. To prevent the stray light photons from entering the telescope, baffles are placed in front of the mirror assemblies. Since eROSITA is performing an all-sky survey, it is particularly important to ensure a good stray light protection in order to get reliable data also in regions of high contamination which are expected to be in the field of view multiple times while the whole sky is scanned. This is the main reason why analysing the eROSITA survey data of HESS J1731-347 is interesting, despite the fact that judging by the exposure, the *XMM-Newton* observation is clearly favorable: The stray light contamination is expected to be much less in eROSITA data than in the *XMM-Newton* data analysed by Doroshenko et al. (2017). Besides that, eROSITA also has a larger collecting area in the soft band, which can be beneficial for absorption studies.

In the focus of each eROSITA mirror assembly, a charge-coupled device (CCD) is located where the information carried by the incoming photons is decoded. Each camera has its own filter wheel which allows an independent adjustment of the filter settings. If the wheel is closed, the respective camera only records the instrumental background data since no photons reach the CCD. The instrumental background consists of the particle background caused by highly energetic particles hitting the CCD and of the electronic noise. In the standard observation mode, the filter wheels of all CCDs are in filter mode. For TM 5 and 7, the filter includes an aluminum layer to shield the CCD from optical light. In contrast, for TM 12346, this aluminum layer is placed directly on the CCD. This difference becomes important for data analysis: It was discovered after the launch of SRG that apparently, there is a leak between the filter wheel and the CCD in eROSITA TM 5 and 7. This leads to a light leak contamination of the data recorded by these two modules since optical light cannot be filtered directly at the CCD.

1.4. Data set considered in the analysis

For the spectral analysis of the remnant in this Thesis work, data of the first four eROSITA all-sky surveys was used. As explained in Sect. 1.3.1, for some reason, there is a light leak contamination of the data recorded by TM5 and 7 which cannot be eliminated due to the absence of on-chip filters for these two modules. Therefore, TM5 and 7 data had to be examined carefully before using them in the analysis. Extracting the spectra of the SNR for TM5 and 7 and comparing them to those of the other 5 TMs with on-chip filters lead to the conclusion that the pollution of the data does not have a bad influence on the fit results in this case (see Sect. 3.3.4 and Appendix C for more detailed information). Also, the X-ray image that includes the data of TM 5 and 7 (see Sect. 2), does not show any suspicious features. Thus, TM5 and 7 data were included in the analysis in order to improve the counting statistics. For the spectrum extraction, as well as for the image creation, the data of all TMs and all eRASS surveys were merged. Event files created with the c946 pipeline processing were used since as of mid-April 2022 only eRASS1 data was available in the 947 processing. The eventlists were merged and filtered using the *evtool* command which is part of the eROSITA Science Analysis Software (*eSASS*). The eSASS EDR4 version was used as it is provided for all IAAT users. Events were filtered by setting the *flagsel* keyword to 0xE000F000 as recommended in the eSASS cookbook[5] to exclude corrupt events. The *pat_sel* keyword is set to 15 by default which excludes all invalid patterns[6].
For spectrum extraction, the *srctool* routine of eSASS was used with the *exttype* option set to *TOPHAT*. The source and background spectrum were produced in two separate extractions. This is the recommended procedure for extended sources. Extracting both spectra in one step implies using the same source-specific good time intervals (GTIs) and Ancillary Response File (ARF) for the source and background region, which can be inaccurate for large extraction areas.[7]
Spectral fitting and modelling was performed using the *sherpa* package provided with the *Chandra* Interactive Analysis of Observation (CIAO v4.14).
According to the entry in the fits header[8] of the merged eRASS:4 spectrum of the total remnant, the effective, dead-time corrected exposure at each location of the SNR is ≈ 2.02 ks. Thus, the *XMM-Newton* observations analysed by Doroshenko et al. (2017) have a much longer exposure and therefore better counting statistics, even though in this case there are large differences between different parts of the remnant. The average exposure of all spectra the authors extracted was ~ 42 ks (see Sect. 1.2.4). An advantage of the eROSITA data is, however, the absence of stray light contamination, as explained in Sect. 1.3.1. Another, less important advantage is also that the exposure is uniform across the remnant.

[5] `https://wiki.mpe.mpg.de/eRosita/CookBook`, accessed 2022-07-05
[6] `https://erosita.mpe.mpg.de/internal/eROdoc/tasks/srctool_doc.html`, accessed 2022-12-19
[7] `https://erosita.mpe.mpg.de/internal/eROdoc/tasks/srctool_doc.html`, accessed 2022-12-19
[8] keyword ‘EXPOSURE’

2. eROSITA X-ray image

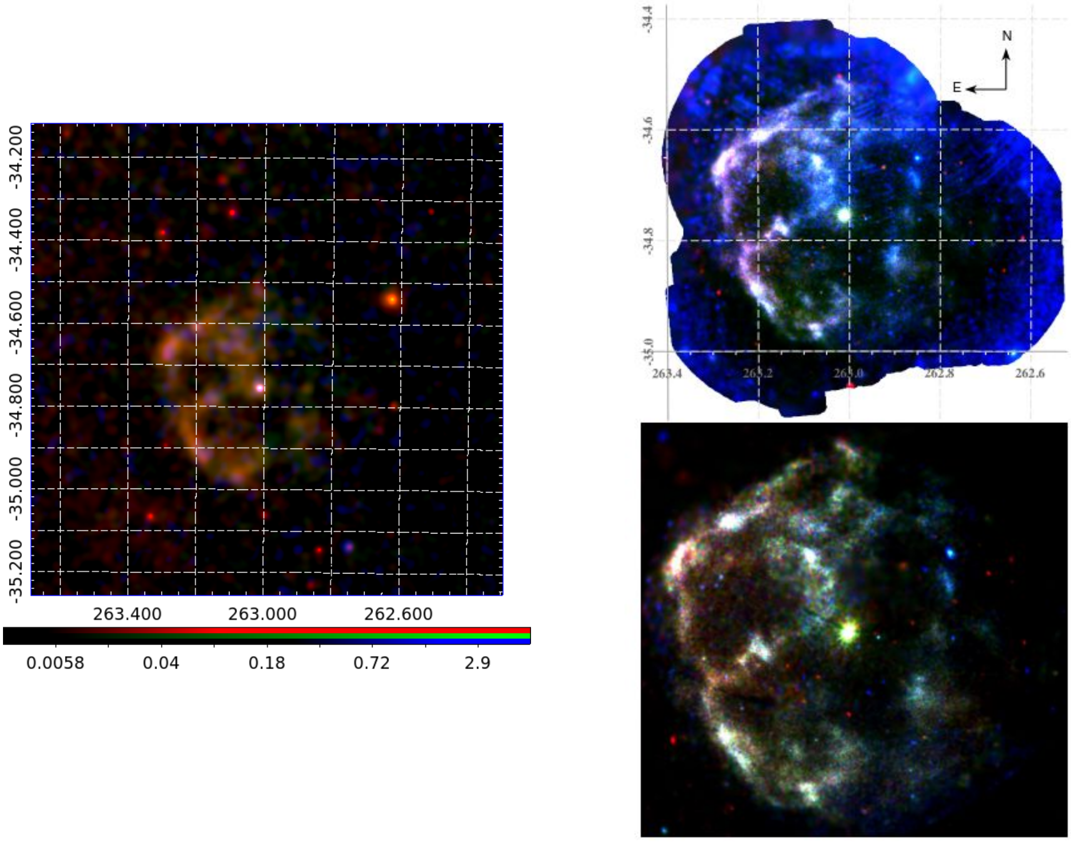

Figure 1: X-ray images of the SNR HESS J1731-347. *Left panel:* Image produced in this Thesis work from eRASS 1 to 4 data of all 7 TMs combined. The RGB colors represent 3 different energy ranges. Red: 0.3-1.8 keV, green: 1.8-2.8 keV, blue: 2.8-10 keV. *Right panel:* Images produced by Doroshenko et al. (2017) from several *XMM-Newton* observation campaigns (see their Fig. 1). The top image illustrates the stray light contamination which manifests in the arc-like structures visible in the upper part of the image. For the bottom right image, contaminated data was removed by Doroshenko et al. (2017). The energy ranges in the bottom right images are the same as those used for the eRASS image. The *XMM-Newton* observations of the remnant provide a considerably longer exposure, which is reflected in the much sharper images with respect to that obtained from the eRASS data.

The left panel of Figure 1 shows the eROSITA X-ray image of HESS J1731-347, created from merged eRASS:4 data of all TMs. Three different energy ranges are overlaid, represented by different colors (see caption for details). For comparison, the images produced by Doroshenko et al. (2017) from *XMM-Newton* data are displayed in the right panel of Figure 1. Comparing the eRASS image to the stray light corrected *XMM-Newton* image of Doroshenko et al. (2017) reflects the clearly better counting statistics of the *XMM-Newton* observations with respect to eRASS:4 (see Sect. 1.4). In the hardest energy band (blue), there is hardly any emission from the remnant in eROSITA data. The highest X-ray emission is detected with eROSITA in the soft 0.3-1.8 keV band (red). The images in all 3 bands were smoothed with a Gaussian kernel using the csmooth routine of the *Chandra* CIAO data analysis package. This routine performs adaptive smoothing, i. e. it calculates the ideal size of the smoothing kernel for each pixel in the image and then smooths each location with its specific kernel.

The maximum width of the kernel, which corresponds to the standard deviation of the Gaussian function,[9] was set to 8 pixels. For reference: The dimension of the image is 1024 times 1024 pixels. The minimum standard deviation of the Gaussian kernel kernel was ≈ 0.7 pixels and was applied for pixels with particularly bright emission like point sources.[10] In sky coordinates, one pixel corresponds to a distance of $\approx 4.0''$, in both x- and y-direction.[11] Thus, the kernel width in arseconds ranges from $\sim 2.8''$ to $\sim 0.53'$, where the latter is applied in regions that do not show small-scale structures.
From the image, it is evident that the remnant is much brighter in X-rays in the left half (i. e. in its eastern hemisphere) than in the right half. This is in agreement with the image Doroshenko et al. (2017) derived from *XMM-Newton* observations.

[9] `https://cxc.harvard.edu/ciao/ahelp/csmooth.html`, accessed 2022-12-19

[10] This is the minimum standard deviation of the Gaussian kernel for the image in the 0.3-1.8 keV energy band. The minimum values in the 1.8-2.8 keV band and 2.8-10 keV band are larger: ≈ 0.8 pixels and ≈ 2.8 pixels, respectively. The maximum standard deviation was set to 8 pixels for all 3 images.

[11] The CDELT1 and CDELT2 keywords in the fits header give the change in the right ascension or declination, respectively, that corresponds to a difference of one pixel in x- or y-direction, starting from a reference pixel. Since the coordinate system is defined on the celestial sphere and not on a plane, this value can change slightly across the image. The values were taken from the unsmoothed image.

3. Total remnant spectrum

3.1. Extraction regions for source and background spectrum

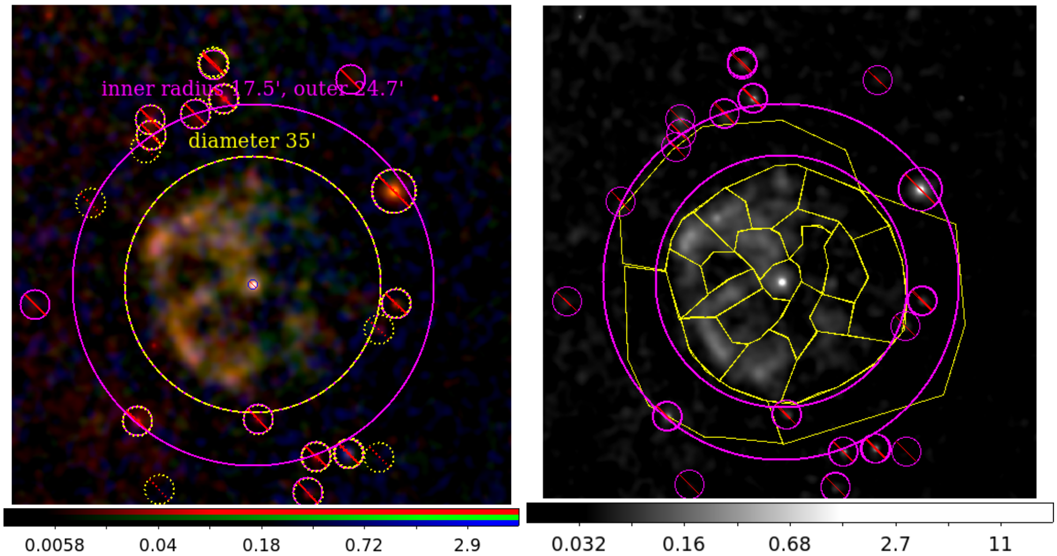

Figure 2: *Left panel:* Extraction region for the spectrum of the total source (yellow) and annulus for background extraction (magenta). The smaller circles mark point sources subtracted from the background region with a radius of 2′ if the source has less than 100 counts and 3′ if the source has 100 counts or more. Yellow dashed circles are point sources from the eRASS 1 to 4 catalogs, magenta circles are sources found when running the eSASS source detection procedure. Several point sources outside the background region are also displayed in the image since the background was extracted also for a larger annulus for the sake of comparison (see Appendix B). Including these sources in the region file does not influence the spectral extraction procedure for the smaller annulus. Within the source region, only the CCO is subtracted with a radius of 40″. *Right panel:* Comparison with the extraction regions used by Doroshenko et al. (2017) in their analysis of *XMM-Newton* data of the remnant, displayed in yellow.

Figure 2 shows in the left panel the extraction region for the total source spectrum and the annulus used to extract the spectrum of the local background. According to Tian et al. (2008), the remnant has an angular diameter of about 30′ in the radio band. Based on that information and under consideration of the eROSITA X-ray image, to extract the spectrum of the whole source, a circular region with a diameter of 35′ (i. e. a radius of 17.5′) was used. Choosing a smaller radius would exclude parts of the emission from the upper left part of the source. The source and background extraction regions are centered on the central compact object (CCO). To precisely determine its position in the X-ray image, the source region was matched with the eRASS1 source catalog[12]. The resulting RA and DEC of the CCO are 263.01417089581287°, -34.75550026824143°. The background annulus has an inner radius of 17.5′ and an outer radius of 24.7′. The inner radius of the background annulus was selected to directly border on the source region since the absorption varies significantly across the supernova remnant (Doroshenko et al., 2017). Thus, it might also vary outside the remnant. Selecting a background region as close as possible to the source (while not including any source emission) increases the probability that, on average, the background spectrum extracted from the annular region is a good representation for the background that underlies the source emission. Figure 2 suggests that

[12] version all_e1_201008_poscorr_mpe_clean

the background emission in the soft energy range (0.3-1.8 keV, red) is increasing towards the lower left corner (better visible on the screen than in print). In Appendix B, the background spectrum extracted from a larger annulus with 20′ and 30′ radii is compared to the one extracted from the annulus shown in Figure 2. Using the spectrum of the larger annulus in the background subtracted fit lead to a lower fit quality and significantly different best-fitting source model parameters which are also given in Appendix B. The differences are only slightly significant, but still the background spectrum from the 20′ to 30′ annulus shows a suspicious behaviour in this fit. Therefore, the narrower annulus directly next to the source region was used in the final analysis. The outer radius of the background region was selected such that the source and background region are of roughly equal area: $A_{\rm src} \approx A_{\rm bkg} \approx 0.27\,{\rm deg}^2$ without considering point source removal in the background region. After removing the point sources following the procedure described in the following Sect. 3.1.1, the background area turned out to be only ~ 90% of the source area.[13]
In the right panel of Figure 2, the extraction regions used in this Thesis work are compared to those used in the *XMM-Newton* study of Doroshenko et al. (2017). The source and background areas agree reasonably well.

3.1.1. Point source removal

In order to remove point source emission from the background annulus region, first the background region was matched with the eRASS 1 to 4 source catalogs[14]. A tolerance of +2′ and -2′ was added at the outer and inner edge of the annulus, respectively, to remove also emission from point sources located right outside the border of the annulus. The match with the 4 eRASS catalogs revealed 36 point sources. Many of them are detected in multiple eRASS surveys. The point sources were then excluded from the background annulus using a radius of 2′ around each source that has less than 100 counts and a radius of 3′ for sources that have more than 100 counts.[15] The larger exclusion radius for brighter sources is motivated by the fact that the absolute flux amount comprised by the wings of the point spread function (PSF) is larger in this case. Thus, even the flux in the PSF wings that makes up only a small percentage of the total source flux might contaminate the background spectrum for very bright point sources. In general, the selected exclusion radii of 2′ or 3′ are fairly large, but since the background extraction area is of sufficient size to preserve good counting statistics, it has no negative impact on the analysis to exclude point sources with a larger radius than it is expected to be necessary. In this way, it is made absolutely sure than no significant part of the emission is left over.
As a further indication where point sources might be located within the background region, the eSASS source detection routine was applied, adopting some of the settings described for the 947 pipeline processing on the eROSITA wiki[16]. As input, an unbinned image of the eRASS 1 to 4 data of all TMs was used with the energy range set to 0.2 to 10 keV, the pattern selection set to 15 (i. e. all valid patterns) and the flag selection set to 0xE000F000 as explained in Sect. 1.4. During the procedure, 14 point sources were detected. A majority of them coincides with sources listed in the eRASS catalogs. Only two additional sources were found (see left and top right magenta circles in Figure 2). On the other hand, the match with the eRASS catalogs yielded 5 sources without a corresponding source detection result (see yellow dashed circles without magenta counterpart in Fig. 2). The source detection is an iterative process with many adjustable parameters. Therefore, investigating the reasons for these discrepancies is beyond the scope of this work. Since the background extraction region is large and assumed to be homogeneous, subtracting regions even without being absolutely sure if they indeed contain point sources is not expected to have a negative impact on the shape of the background spectrum or the counting statistics. This is only true, of course, to a certain extent were not a major part

[13]The ratio was determined from the 'REGAREA' keyword values in the fits headers of the two spectra.
[14]versions all_e1_201008_poscorr_mpe_clean, all_e2_201221_poscorr_mpe_clean, all_e3_210707_poscorr_mpe_clean, all_e4_211223_poscorr_mpe_clean
[15]Sources detected in multiple eRASS surveys would be excluded with a 3′ radius as soon as they exceed 100 counts in one survey. However, there has been no such case.
[16]`https://wiki.mpe.mpg.de/eRosita/PipeProc947`, accessed 2022-04-27

of the background region is covered by suspected point sources. Figure 2 shows that the subtracted regions do not make up a major part of the background region. For this reason, the point sources found in the eRASS catalogs as well as in the source detection were all excluded without further investigation before extracting the background spectrum.
Masking out point sources within the source region is, of course, way more critical than in the background region since unnecessarily losing source photons has to be avoided - especially in cases like this where the counting statistics are not that good in general. The search for point sources within the remnant is complicated by the fact that the dense filament structures in its eastern part are misidentified as point source emission at many locations. Figure 3 illustrates this problem. All point source detections within the remnant region from the eRASS 1 to 4 catalogs are plotted, and it is evident that they trace the filament structures of the shell emission. Besides erroneously reducing the counting statistics of the remnant emission, removing all the suspected point sources would quite likely distort the shape of the remnant spectrum. The spectra of bright filaments, which are at many locations misidentified as point sources, are expected to have a different shape than those of dimmer source regions. Point source removal without extensive further investigation would introduce a bias towards removing these brighter contributions.

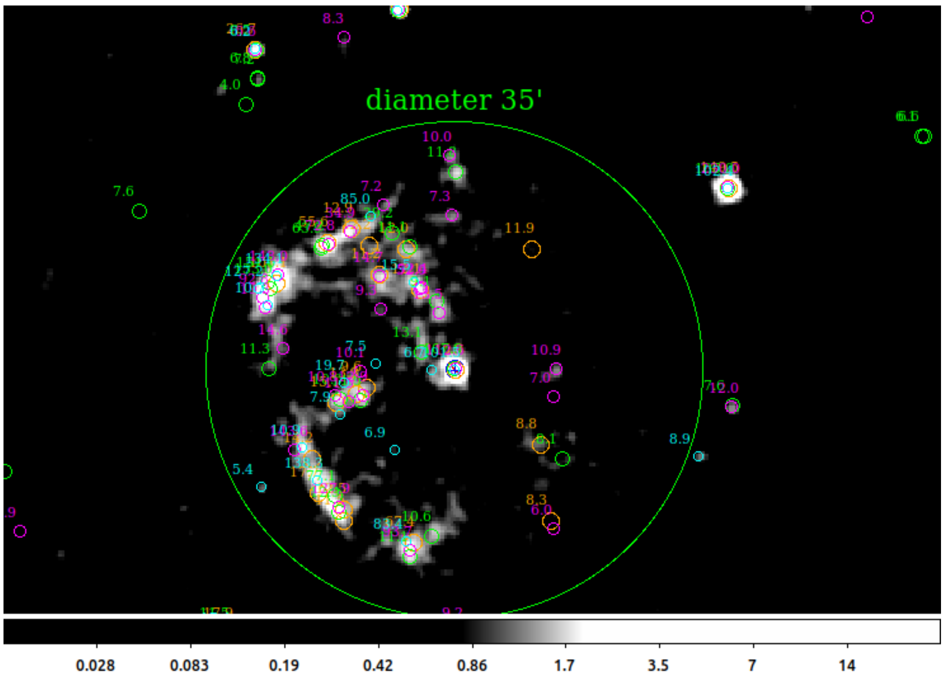

Figure 3: Match of point sources in eRASS 1 to 4 catalogs with the source region. The image is meant to give a qualitative overview about how many detections trace the filament structures of the remnant and are therefore no real point sources but part of the source emission. Labels denote the counts in the respective eRASS catalogs. Colors: cyan - eRASS1, magenta - eRASS2, green - eRASS3, orange - eRASS4. For the image, photons of eRASS1 to 4 from all TMs are summed up in a 0.3-10 keV energy range. Different colors for different energy bands are avoided to increase the visibility of the point sources. The image was smoothed with ds9.

For the above-mentioned reasons, within the source region, the only point source that was excluded is the CCO. In this case, an exclusion radius of $40''$ was used, attempting to find a good balance between minimizing the risk of contamination and losing as little source photons as possible. The selection of the CCO exclusion radius involved an analysis with APETOOL, which is also part of the eSASS software package. Based on a fits image of a certain sky area, this routine determines for each detected source the aperture radius in units of arcseconds that comprises a certain fraction of the energy emitted by the source (the so-called energy encircled fraction or EEF). To get a benchmark for the exclusion radius of point sources, the APETOOL routine was applied to the sources found in the source detection (see above) in the sky tile 264126 containing the SNR HESS J1731-347. As a result, a fraction of 95% of the source energy was found to be on average comprised within an aperture radius of ~ 31.4″, while an EEF of 75% corresponds to a mean aperture radius of ~ 11.8″. The results for all sources are distributed in a narrow range around these mean values: The maximum value found for EEF=95% was ≈ 31.7″ and the minimum ≈ 30.9″. The range is similarly small for EEF=75%. Based on these results, > 95% of the energy emitted by the CCO is expected to be comprised by an exclusion radius of 40″. Counts and energy are linearly related by the energy conversion factor (ECF).[17] Thus, determining the counts of the source region in sherpa and comparing this number to 5% of the CCO counts listed in the eRASS catalogs gives a conservative estimate on whether the remaining CCO emission influences the remnant spectrum. For the spectrum of the total source, this is clearly not the case: The source region spectrum (circle of radius 17.5′ around the CCO) has a total of 12256 counts when summing up all 7 TMs and the eRASS 1 to 4 observations in the energy range of 0.2 to 10 keV.[18] The CCO has ~ 100 counts in the broad energy band[19] of each eRASS, thus in total ~ 400 counts. Less than 5% (=20 counts) are expected to remain after masking out the CCO with 40″. Thus, the ratio of contaminating CCO emission to source photons is on the order of 1-2‰ and therefore negligible. This becomes a bit less obvious when the remnant is divided in several sub-regions for the spatially resolved spectral analysis in section 4. Since the smaller sub-regions have less counts, the impact of the remaining CCO emission might become more noticeable.

3.2. Background subtracted fit

3.2.1. General concept

A simple approach to deal with the background contribution when fitting the source spectrum is to subtract the background emission before the fit. This is an alternative to fitting the source and background spectrum simultaneously which requires a model representation of the background (see Sect. 3.3). In the case of background subtraction, no background model is needed because the contribution of the background to the source spectrum is removed. Of course, for the emission in the source region, source and background radiation cannot be disentangled. Therefore, the background spectrum is extracted from a separate region. Before subtracting the two data sets, the counts of the background spectrum are renormalized using the exposure ratio and the BACKSCAL ratio[20] of the source to the background extraction area, respectively.[21] Fig. 4 shows the background-subtracted spectrum together with the background spectrum and the total spectrum extracted from the source region. The corresponding extraction regions are the ones described in Sect. 3.1. The background spectrum displayed in Fig. 4 was extracted from an area which is about 90% the size of the source region (see Sect. 3.1) and was not renormalized before plotting. Therefore, it does only represent the background spectrum used for the subtraction in its shape, not in the absolute count rate, which is modified by renormalization. However, the difference between the source and background area is not that large and the plot is only intended to give a qualitative comparison between the shape of the combined source and background spectrum, background spectrum and background subtracted

[17] According to the eROSITA wiki (see `wiki.mpe.mpg.de/eRosita/eROSITA%20ECF`), the ECF is defined as the ratio between count rate and flux, which is the same as the ratio of counts to energy per unit area. In this case, to get the energy, an additional factor of $4\pi d^2$ is needed, where d is the distance of the object.

[18] The value corresponds to the sum of the counts of all channels that lie within the considered energy range: np.sum(get_counts(src_spec)[np.where(np.logical_and(get_data_plot(src_spec).x>0.2,get_data_plot(src_spec).x<10))]) in sherpa, where get_data_plot().x returns an array with the energy values for all 1024 channels.

[19] i. e. in the band with suffix "_0" ranging from 0.2 to 10 keV

[20] The BACKSCAL keyword of a spectrum contains the average intersection area of the source region with the total detector area during the source-specific good time intervals (GTIs) of the observations, in units of square degrees. It can differ from the geometrical extraction area in case the source is not always completely covered by the field of view during the source-specific GTI, which is expected to happen for extended sources.

[21] `https://cxc.cfa.harvard.edu/sherpa/ahelp/subtract.html`, accessed 2022-12-19

spectrum. It can be seen in the plot that the error bars towards the high and low energy end increase for the background subtracted spectrum since there is only a very low number of events left.

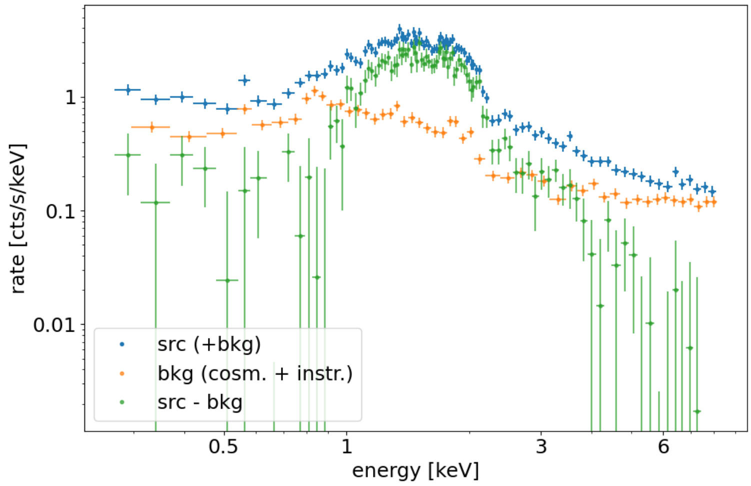

Figure 4: Illustrative plot for background subtraction. Blue: total spectrum extracted from the source region. Orange: spectrum extracted from the background annulus (inner radius 17.5′, outer radius 24.7′). Green: background subtracted spectrum of the source region. All spectra are grouped to at least 100 counts per bin. The background extraction area is about 90% of the source area. None of the spectra have been renormalized for the plot.

The approach of background subtraction has two caveats: First, the *cstat* statistics (Cash, 1979) is not applicable to background subtracted data sets since it requires the counts in each bin to be Poisson distributed. This is true for the source and background spectra themselves, but subtracting two Poisson distributed data sets does not result in another Poisson distributed data set.[22] Thus, χ^2 statistics has to be applied which uses Gaussian errors for the spectral data (i. e. assumes that the counts in each bin are normally distributed). This is only true for a sufficiently large number of counts per bin which is not expected to be fulfilled for the eRASS:4 data of HESS J1731-347. When performing a background modelling fit, the *cstat* statistics can be used which is more adequate since it assumes a Poissonian distribution of the counts. A second disadvantage of the background subtracted fit is that it leaves no possibility to understand in detail the properties and shape of the background spectrum and control the way it is treated in the fit. If, for instance, the background spectrum in the source region has different features than the one extracted from the background region, this remains completely unnoticed when performing background subtraction. Especially in the case of HESS J1731-347, there is indication that the shape of the background spectrum might not be completely locally uniform in the sky area around the source: As the *XMM-Newton* study of Doroshenko et al. (2017) showed, the absorption is varying across the source region, thus it is changing locally on a small scale. It might therefore also be different on average for the background annulus and the remnant region. This implies that the shape of the background spectrum underlying the source emission might be slightly different from the one extracted from the background annulus. Finding a solution to such a problem is also not guaranteed to succeed when modelling the background. However, one is at least more aware of the properties of the background radiation and eventual issues arising from the background treatment and there are more possibilities to react.
For the above-mentioned reasons, the simultaneous fit is the preferred approach, especially in cases like HESS J1731-347 where the counting statistics of the eROSITA observations are not good and where there is indication for small-scale changes in the spectra due to absorption. An advantage of the background subtracted fit is, however, that while it leaves no possibility to control background

[22] `https://heasarc.gsfc.nasa.gov/xanadu/xspec/manual/XSappendixStatistics.html`, accessed 2022-12-19

treatment, in return it does not require any assumptions on the shape of the background spectrum as input. These assumptions influence the fit results of the source region spectrum in the case of the simultaneous fit and thus the source model parameters.

3.2.2. Optimization method and spectral model

Since it can be useful to compare the results to those of background modelling (and out of curiosity), a background subtracted fit of the HESS J1731-347 spectrum was carried out in the course of this Thesis. The background-subtracted spectrum was grouped such that each bin contains at least 100 counts. The fit statistics used was *chi2gehrels* which is the sherpa default statistic. The *cstat* statistics is not applicable to background-subtracted data sets, as explained above. The fit method applied for the background subtracted fit was the Nelder-Mead simplex optimization method (*neldermead*, Nelder and Mead 1965, sherpa implementation based on Lagarias et al. 1998). Compared to the Levenberg-Marquardt optimization (*levmar*, Levenberg 1944, Marquardt 1963, sherpa implementation based on Moré 1978) it tends to be more robust against getting stuck in local minima of the statistics value which can be mistaken for the final solution of the optimization problem. The two algorithms apply different mechanisms to minimize the fit statistics value: The Levenberg-Marquardt optimization just adds a gradient to the parameter set several times and re-calculates the fit statistics for the resulting slightly changed set of parameters. When the statistics value is lower, it continues to add a gradient pointing in the same direction in parameter space. If it is higher, a different direction is probed. In contrast, the Nelder-Mead optimization method models the shape of the parameter space locally using a combination of 3-dimensional parabolic functions. The algorithm tries to find a direction where the fit statistics decreases based on the parameter space model. As a consequence, the *neldermead* method is more expensive in terms of computational resources. However, the background subtracted fit is not a demanding process in terms of computation time in any case due to the low number of free model parameters and the low counting statistics of the subtracted data set. Thus, the *neldermead* method was selected since its application does not notably increase computation time in this case.
The source emission is modelled by an absorbed power law:

$$\text{source\_emission} = \text{xstbabs.nH} \cdot \text{xspowerlaw.pl\_snr} \tag{2}$$

The xspec model components within sherpa have been used. Absorption is represented by the Tuebingen-Boulder ISM absoprtion model (*tbabs*, Wilms et al. 2000). Therefore, also the abundances were set to the values suggested by Wilms et al. 2000.

3.2.3. Fit results

The background-subtracted spectrum was fitted in the energy range from 0.5 keV to 4 keV since outside this range, it is dominated by background emission.[23]
In order to evaluate the influence of the above-mentioned absorption variations on the background subtracted fit, it was carried out three times, using different extraction regions for the background spectrum: The complete annulus around the source region shown in Fig. 2, only its left half and only its right half as displayed in Fig. 6, left panel. Point sources are removed as described in Sect. 3.1. The corresponding spectra are shown in Fig. 5, right panel. The shape of the spectra differs especially around 1 keV. The background spectrum extracted from the total annulus resembles more the one from the less absorbed left half which can be expected since it is dominated by the larger number of photons from that region.
The results of the background subtracted fit for different background spectra and the plots of the corresponding models are given in Table 1 and Fig. 6. The 1σ confidence bounds are determined

[23] Considering a wider energy range of 0.3-8 keV does not yield significantly different results: $\Gamma_{SNR} = 2.83$ (+0.22 − 0.20), norm_{SNR}= 0.047 (+0.010 − 0.008), N_H = 2.03 (+0.16 − 0.15), χ^2_{red} = 0.84 for the background spectrum extracted from the total annulus.

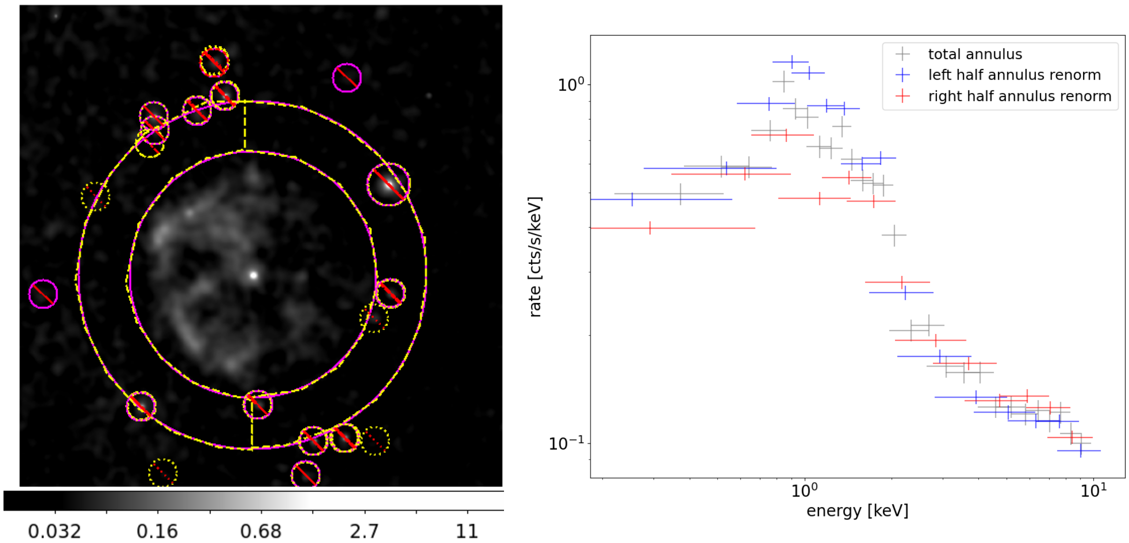

Figure 5: *Left panel*: Background regions used to extract spectra for the background-subtracted fit in order to evaluate the impact of the absorption variations. The two half-annuli are approximated by polygons and displayed with dashed yellow lines. The area ratio of the right to the left region is ~ 95% under consideration of point source removal (i. e. the crossed circles are removed). The magenta annulus is the total background annulus as shown in green in Fig. 2. *Right panel*: Corresponding spectra extracted from the regions in the left panel. The spectra of the left and right half annulus were re-normalized using the area ratio of the respective region to the total annulus. All spectra are grouped to at least 200 counts per bin.

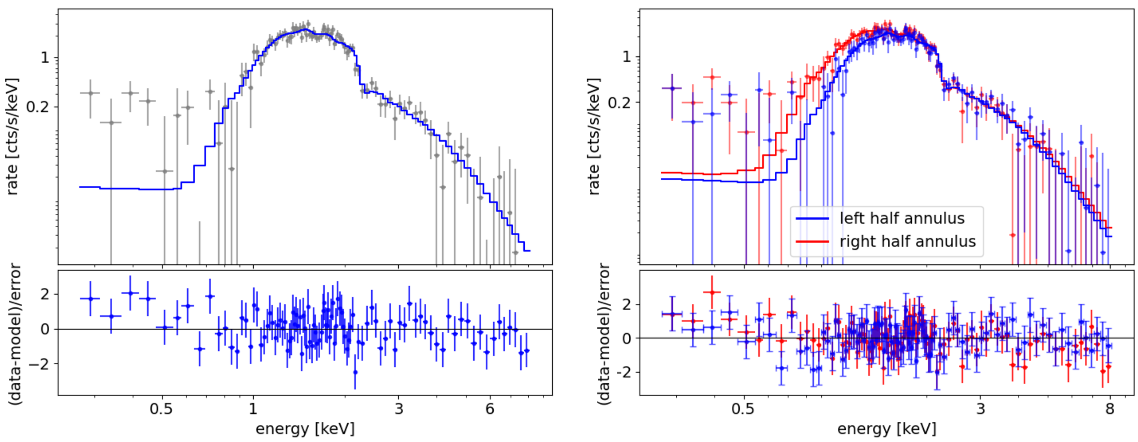

Figure 6: Best-fitting models of the background subtracted fits using the background spectrum extracted from different regions. *Left panel:* using total annulus as shown in magenta in Fig. 5. *Right panel:* using half annuli as displayed in green in Fig. 5. All spectra are grouped to a minimum number of 100 counts per bin before the fit. The bottom panel shows the deviation of model and data, in units of the respective data point errors. Almost all deviations are within the range of 2Δ with Δ being the error of the rate. For the fits, only data points within the 0.5-4 keV energy range were considered. The plots are showing a wider energy range.

with the sherpa *conf()* command. For all 3 background regions, the photon index obtained for the background subtracted spectrum agrees within 1σ uncertainties with the result found by Doroshenko et al. (2017). In general, the best-fitting parameter results for the total background annulus spectrum

Table 1: Best-fitting values and 1σ confidence bounds for the source model parameters in the background subtracted fit. $\Gamma_{\rm SNR}$ is the photon index of the power law used to model the remnant emission, $\rm norm_{SNR}$ its normalization factor and N_H the absorption column density. The last column lists the reduced statistics values for the best fit. The results for three different background extraction regions are shown: the total annulus with inner radius 17.5′ and outer radius 24.7′, the left half of it and the right half of it.

parameter	$\Gamma_{\rm SNR}$	$\rm norm_{SNR}$ [photons/s/cm^2/keV]	N_H [10^{22} atoms/cm^2]	red. stat.
total bkg annulus	$2.77^{+0.23}_{-0.22}$	$0.045^{+0.010}_{-0.008}$	$2.00^{+0.17}_{-0.16}$	0.79
left half	$2.90^{+0.32}_{-0.29}$	$0.056^{+0.019}_{-0.013}$	$2.40^{+0.25}_{-0.23}$	0.71
right half	$2.51^{+0.24}_{-0.22}$	$0.034^{+0.008}_{-0.006}$	$1.59^{+0.15}_{-0.14}$	0.66

(first row in Table 1) lie in between the values for the left and right half which can be expected since the total annulus is in some sense an average of the left and right half. The difference in Γ_{SNR} for the left and right background spectrum is not significant at 1σ. That in $norm_{SNR}$ is hardly significant. However, the absorption in the background subtracted source spectrum fit is significantly higher when using the background spectrum from the less absorbed left half annulus. This is because the less absorbed spectrum leads to a higher estimated background emission in the source region, which is then subtracted, leaving behind an apparently stronger absorbed source spectrum than when using the stronger absorbed background spectrum from the right half annulus. The shape of the models for the two cases differs notably below $\sim$ 1 keV (see Fig. 6). However, the large error bars of the spectra in this energy range relativize the meaning of the deviations.

The reduced statistics values of all best fits are below 1 (see Table 1) which indicates a good agreement of model and data since it implies that the average deviation is within data point uncertainties.
Besides the reduced statistics value, two other methods to evaluate the quality of the fit are firstly contour plots where the 1σ, 2σ and 3σ confidence bounds are displayed in a 2d plot for a pair of model parameters and secondly interval projection plots that show the fit statistics value as a function of one model parameter. An example for both is given in Fig. 7 for the case of the background spectrum extracted from the total annulus. The contour plot in the left panel displays the regions in the parameter space within which the best-fitting value lies with a probability of 68% (1σ confidence, innermost ellipse), 95% (2σ confidence, middle ellipse) and 99.7% (3σ confidence, outermost ellipse). In the example in Fig. 7 left, the photon index and the absorption are varied within a certain range while the other fit parameters (in this case only the normalization) are re-fit for each (N_H,Γ) pair. In the plot, a clear correlation between the two quantities is evident: A higher Γ in combination with a higher N_H can lead to a comparably good fit.
The interval projection plot in the right panel of Fig. 7 shows the statistics value when varying $\Gamma_{\rm SNR}$ in certain steps. The other free parameters are re-fit in each step and the statistics values of these fits are plotted. Looking at such plots, one can reassure that the fit indeed converged to the global minimum of the statistics value which is clearly true in this case. It is evident that the 1σ ranges for Γ and N_H in the contour plot are wider than the ones given by the *conf()* method (see Table 1). This is probably due to the different approach used to determine the confidence limits in both cases: The *conf()* method varies only one parameter at a time in certain steps and re-fits all the other free parameters, just like the interval projection. For the contour plot, however, two parameters are varied at the same time and only the remaining ones are re-fitted.

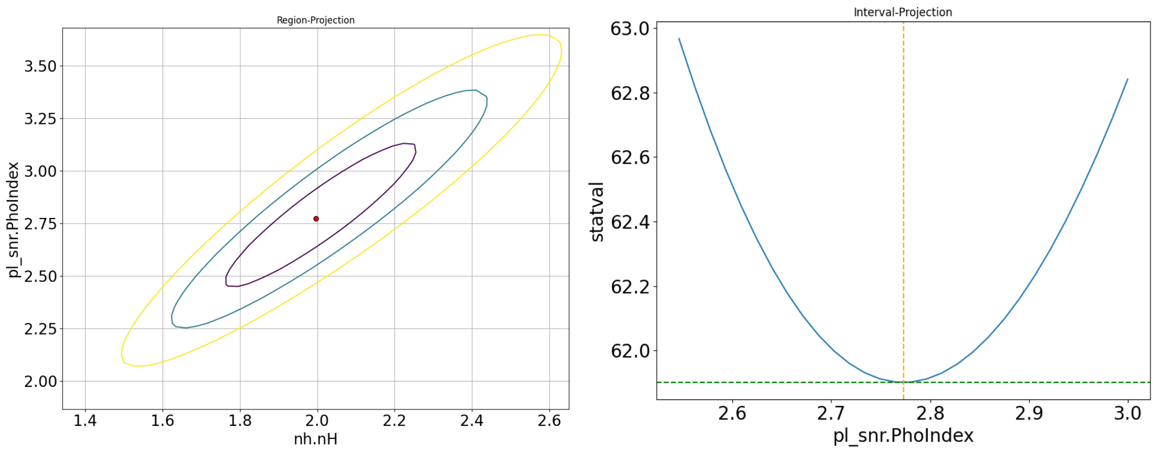

Figure 7: Two example plots to evaluate the quality of the fit. *Left panel:* Contour plot with the absorption column density N_H on the x-axis and the photon index of the remnant emission Γ_{SNR} on the y-axis. There is a clear correlation of the parameters visible from the inclination of the ellipses: A higher photon index in combination with a higher absorption results in a similarly good fit for the same data set. This is a well-known problem in X-ray spectral analysis. *Right panel:* Interval projection plot. The statistics value is plotted versus Γ_{SNR}.

As mentioned above, the photon indices of the remnant power law obtained from the background subtracted fits for all 3 background regions agree well with the value found by Doroshenko et al. (2017). In contrast to this, the absorption column density N_H resulting from the background subtracted fit is higher than what can be expected based on the *XMM-Newton* analysis results, at least when using the total background annulus spectrum and that extracted from the less absorbed left half. Although the values cannot be compared directly since Doroshenko et al. (2017) did not conduct a fit of the total remnant with a uniform N_H, the absorption column densities they obtained for their sub-regions of the source span a range from (1.02 ± 0.01) to $(1.95 \pm 0.09) \cdot 10^{22}$ atoms/cm^2. Thus, the result of the background subtracted fit in this work for the total background annulus ($N_H = (2.00 \pm 00.16) \cdot 10^{22}$ atoms/cm^2) corresponds to the N_H that Doroshenko et al. (2017) found for the sub-region with the highest N_H within the source area. This is a bit surprising since the N_H obtained from the background subtracted fit can be considered an average value as it is assumed to be constant over the whole remnant. Therefore, one would expect it to lie at least in the middle of the range spanned by the results of the *XMM-Newton* analysis if not even close to the values of the less absorbed sub-regions. The latter expectation is motivated by the fact that the spectrum of the total remnant is dominated by the radiation from the bright left half of the source since way more photons originate from this area than from the dim right half. Only the background subtraction using the background spectrum from the stronger absorbed right half annulus results in an absorption column density that is according to the expectations.

3.2.4. Sources of uncertainty

One source of uncertainty that can be expected to cause higher N_H values for the analysis conducted in this Thesis with respect to the study of Doroshenko et al. (2017) is the selection of the absorption model and in this context particularly of the abundances. The abundances determine the composition of the light absorbing interstellar medium, thus they form the basis for the determination of N_H. Doroshenko et al. (2017) used the *wabs* absorption model which applies the abundance values of Anders and Ebihara (1982, henceforth *aneb*). For this Thesis, the *tbabs* model has been used which requires the abundances of Wilms et al. (2000, henceforth *wilm*). Performing the background subtracted fit for

the total background annulus with the *wabs* model and the *aneb* abundances results in a significantly lower absorption column density than that given in Table 1: $N_H = (1.47 \pm 0.12) \cdot 10^{22}$ atoms/cm^2 while the photon index ($\Gamma_{wabs} = 2.81^{+0.24}_{-0.22}$) and the normalization factor ($\text{norm}_{wabs} = 0.048^{+0.011}_{-0.009}$) are in agreement with the values obtained with the *tbabs* model and *wilm* abundances (Table 1). The goodness of fit is also equal ($\chi^2_{\text{red}} = 0.79$). Since both the *tbabs* and the *wabs* model require one specific absorption choice, which is different between the two of them, it is difficult to distinguish whether the differences are caused by the absorption models themselves or by the abundance selection. Testing *tbabs* with other abundances than the recommended ones cannot be expected to produce reliable results and for *wabs*, it is not even possible since it uses Anders and Ebihara (1982) regardless of the *set_xsabund()* command[24]. However, the background subtracted fit with the total background annulus was then conducted using the *phabs* absorption model with different abundances to test the effect on the N_H result. The *wilm* abundance values lead to $N_H = (1.97 \pm 0.07) \cdot 10^{22}$ atoms/cm^2 and for *aneb*, the result was $N_H = (1.50 \pm 0.05) \cdot 10^{22}$ atoms/cm^2. The photon indices and remnant power law normalizations are compatible within 1σ bounds with the result of the *tbabs* model and *wilm* abundances in both cases.
To sum up, there seems to be a systematic uncertainty in the absorption column density of about $\Delta N_H = 5 \cdot 10^{21}$ atoms/cm^2, mainly arising from the selection of the abundances.

An additional systematic uncertainty arises from the selection of the background region since the spectral shape is not exactly the same for different regions (see Fig. 5). The background subtracted fit necessarily assumes that the background emission in the source region has the exact same properties as that in the background region. Thus, to get reliable results, also the average absorption of the background emission in the source region has to be very similar to the average absorption in the background region. This assumption could be wrong, especially when considering that the total spectrum is always dominated by the emission from the least absorbed sub-regions.
In order to get a quantitative idea of the difference in the absorption, the spectra of the left and right half annuli were fitted with the background model described in Sect. 3.3.1. This cross-check anticipates parts of the fitting procedure and described in Sect. 3.3 and also some of the best-fitting parameters found in this section. However, it is useful to quote these results here and apply the background model in order to quantify the differences in the spectra extracted from the left and right background half annulus. This can help to better understand the different parameter results for different background spectra in the background subtracted fit.
The spectra extracted from the left and right half annulus were both fitted simultaneously, freezing the APEC temperatures and the normalizations of all components to the values obtained for the total annulus in Sect. 3.3.3, see Table 2, and putting a constant factor as a free parameter in front of the total model.[25] The resulting absorption column densities from the fit were $N_H = (0.92 \pm 0.04) \cdot 10^{22}$ atoms/cm^2 for the left, less absorbed region and $N_H = (1.16^{+0.07}_{-0.06}) \cdot 10^{22}$ atoms/cm^2 for the right region. For the total annulus, the result is close to that from the left half: $N_H = (0.98^{+0.12}_{-0.14}) \cdot 10^{22}$ atoms/cm^2 (anticipated from Sect. 3.3.3).[26] Looking at the results of Doroshenko et al. (2017) for the absorption in various sub-regions across the remnant, see their Fig. 2 right panel, the average absorption for the source region is expected to be higher than $(0.92 \pm 0.04) \cdot 10^{22}$ atoms/cm^2

[24] https://heasarc.gsfc.nasa.gov/xanadu/xspec/manual/XSmodelWabs.html, accessed 2022-12-19

[25] Rescaling the model with a fixed parameter corresponding to the area ratio of the half-annuli to the total annulus did not result in a reasonable fit. The results for the scaling factor are 0.60 ± 0.03 for the left half annulus and 0.45 ± 0.03 for the right. This does not reflect the area ratio of the two half annuli, which is $A_{\text{right}}/A_{\text{left}} \approx 0.95$. Possibly, the difference in the observed counts is only partly due to a stronger absorption in the right half and there is an additional intrinsic decrease in the surface brightness towards the western direction. Doroshenko et al. (2017) found this for the remnant. It might also be true for its surroundings, even though the background radiation is in principle assumed to be locally uniform. Since all normalizations were frozen in the simultaneous fit of the two half-annuli and only N_H and a constant factor in front of the model were free fit parameters, the constant factor might account for the intrinsic brightness difference and therefore not reflect the area ratio.

[26] The uncertainties are larger in this case since all normalizations and temperatures of the cosmic X-ray background model components were thawed in this fit.

and probably also higher than $N_H = (1.16^{+0.07}_{-0.06}) \cdot 10^{22}$ atoms/cm^2. This holds especially if it is considered that the *tbabs* model used in this Thesis work tends to result in higher absorptions than the *wabs* model used by Doroshenko et al. (2017). When fitting only the emission of the source region, the best-fitting value for the absorption is $N_H = (1.84^{+0.06}_{-0.08}) \cdot 10^{22}$ atoms/cm^2 (see Table 4). Given the circumstance that the absorption varies so strongly, the disability of the background subtraction method to assume a different absorption for the source and background region is a major disadvantage that is expected to distort the fit result.
Besides that, background subtraction also involves an inaccuracy in the scaling of the background: Both the cosmic and the instrumental background are re-scaled by the same factor, namely by the BACKSCAL and exposure ratio (since the re-normalization is performed in terms of counts).[27] The drawback in this approach is that the signal of the instrumental background is not subject to the effective area of the TMs and therefore it scales differently with the extraction area than the cosmic X-ray background[28] (see Sect. 3.3.1 for more information). This can be an additional reason to take the results of the background subtracted fit with care, in case the ratio of the BACKSCAL and REGAREA values between two regions are different. For the source region defined in Fig. 2 and the background annulus also shown there, the ratio of the BACKSCAL values is src/bkg=1.47 and of the REGAREA values src/bkg=1.10.
In general, when comparing the best-fitting parameters of the background subtracted eROSITA spectral fit to the results of the *XMM-Newton* study of Doroshenko et al. (2017), one should keep in mind that first, these authors performed a fit with background modelling which is a different approach. And second, they did not fit the total source spectrum with uniform parameters but divided the remnant into 19 sub-regions (plus 3 background regions) and the absorption column density N_H was allowed to vary between different regions. These two differences limit the meaning of a comparison of the results. In principle, deviating results can also arise from the different calibration and sensitivity of the two instruments. However, the values for the photon index are in good agreement and the limiting factor in constraining and comparing N_H is quite clearly the large influence of the abundance selection. In general, fitting the spectrum of the total source area with a constant N_H is not accurate given the strong local variations found by Doroshenko et al. (2017).

Given the various caveats described above and at the beginning of the section, conducting the fit with background modelling as described in the next sections is clearly the preferable approach to background subtraction. However, the background subtracted fit was taken as a starting point to get familiar with the fitting procedure and as a different approach to compare results with background modelling. In the following Sect. 3.3, the simultaneous fit of source and background region spectrum using a background model is performed for the total remnant. After that, the source is divided into sub-regions as described in Sect. 4 in order to analyse the changes of absorption column density and photon index.

3.3. Simultaneous fitting of background and source region spectra

3.3.1. Background model

To get meaningful information about the source emission when fitting all photons of source and background radiation simultaneously, one has to give as input several assumptions about characteristics of the background spectrum: the background model. In this way, it is possible to distinguish the contribution of the source from the background radiation. In general, the X-ray background model consists of two components: the instrumental background and the cosmic X-ray background.

[27] `https://cxc.cfa.harvard.edu/sherpa/ahelp/subtract.html`, accessed 2022-10-20
[28] `https://wiki.mpe.mpg.de/eRosita/XWP%20Background%20Modeling`, accessed 2022-10-20

Instrumental background

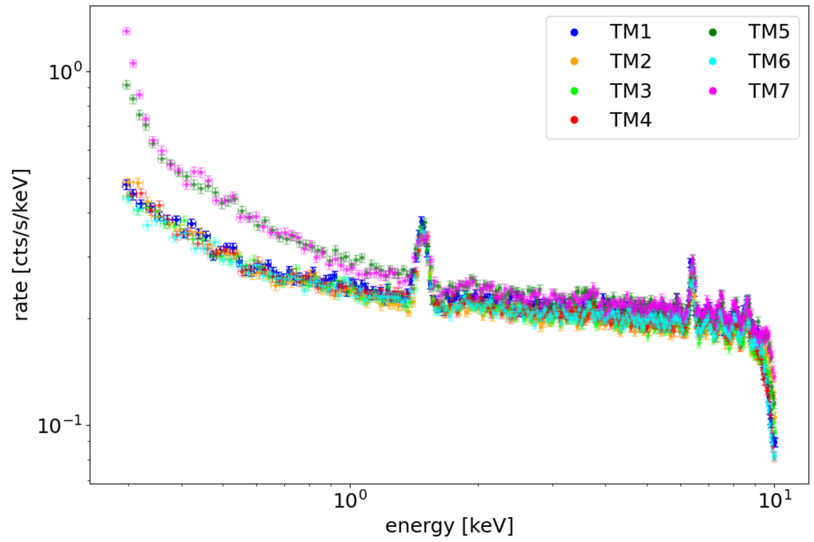

Figure 8: FWC data for all 7 telescope modules of eROSITA. The spectra were grouped to at least 1000 counts per bin for the plot.

The instrumental background is the signal the telescope records when no photons enter, i. e. when the filter wheel is closed. Therefore, it is also called filter wheel closed (FWC) data. The signal arises from electronic noise on the one hand and from ionizing particles entering the detector and inducing charges on the CCDs on the other hand. To constrain the instrumental background of eROSITA, many FWC measurements have been taken in the time from the launch of the instrument in July 2019 until October 2020. The resulting (merged) event lists and spectra are available on the eROSITA webpages[29]. The instrumental background has been measured for each TM separately and separate FWC models are available under the same link as the spectra. During this Master Thesis, revised FWC models were provided by Michael Yeung, a member of the eROSITA SNR working group. The new models are available on the eROSITA wiki[30] and were used in the analysis of this Master Thesis. The background model consists of 14 Gaussian components to represent emission lines. On top of that, the product of an exponential component with the sum of a broken power law and two ordinary power laws is added. The instrumental background component has no free parameters except for a constant factor by which the whole model is multiplied to account for different extraction areas. For a larger extraction area, also information from a larger area on the CCDs is used, which leads to a higher instrumental background. The scaling factor also has to take into account that potentially only a certain fraction of the region of interest is in the detector field of view during the good-time interval (GTI)[31]. For the cosmic X-ray background radiation (see next paragraph), this is considered by folding the model through the Anncillary Response File (ARF). The ARF stores the product of quantum efficiency and effective detector area for a given energy.[32] Since the instrumental background is not a signal caused by photons entering the detector, the instrumental background model is not folded through ARF. Instead, it has to be rescaled for different extraction areas by the BACKSCAL value in the fits header.[33, 34] The BACKSCAL value is the average intersection area of the extraction region

[29] `https://erosita.mpe.mpg.de/edr/eROSITAObservations/EDRFWC/`, accessed 2023-01-23

[30] `https://wiki.mpe.mpg.de/eRosita/New%20FWC%20Models%20in%20c946%20processing`, accessed 2022-04-27

[31] The source-specific GTI is the time during which the telescope is operating correctly and the source is in the field of view.

[32] `https://cxc.cfa.harvard.edu/ciao/dictionary/arf.html`, accessed 2022-07-12

[33] `https://wiki.mpe.mpg.de/eRosita/XWP%20Background%20Modeling`, accessed 2022-10-20

[34] `https://erosita.mpe.mpg.de/internal/eROdoc/tasks/srctool_doc.html`, accessed 2022-10-20

with the detector field of view during the GTI. In the analysis conducted here, the scaling factor of the instrumental background not only has to account for the size of the extraction area, but additionally for the fact that the analysed spectra combine the data of all 7 TMs (see Sect. 1.4). This made it difficult to constrain the scaling factor of the instrumental background a priori using the BACKSCAL value and therefore it was decided to leave it as a free fit parameter. It was constrained for the background annulus from the simultaneous fit of the source and background region and rescaled for other extraction areas using the BACKSCAL in the further analysis. Using the provided FWC models in the analysis, which are based on measurements taken in 2019 and 2020 (see above), involves the assumption that the flux of the particle background is constant over time. Therefore, eventual changes, e. g. related to the alternating solar magnetic activity during the solar cycle, are not considered. The particle background of eROSITA has been estimated before the launch and the actual measurements turned out to be 5 times higher than these estimates, as explained in an internal document.[35] This is partly explained by the fact that the pre-launch estimates assumed the case of a solar maximum, while the FWC measurements were taken at the solar minimum (Predehl et al., 2021). At the maximum, the magnetic field of the Sun is at its strongest state, which implies a better shielding of space telescopes against cosmic rays. Also for *XMM-Newton*, the particle background at the solar minimum exceeds the pre-launch estimate by a factor of 2.3.[32] Another source of inaccuracy might be the mass models used to estimate the instrumental background before the launch, which turned out to represent the instrument not quite accurately. However, apart from the not fully explained deviation from the pre-launch estimates, the eROSITA particle background is quite well understood and was found to be more stable over time than that of *XMM-Newton* (Predehl et al., 2021). No background flares were observed in the background of the *Ultra-Deep Survey area* (UDS), which indicates that the contamination by soft protons should be negligible for eROSITA.[36]

The modelling of the instrumental background as it is done in this Thesis is based on an approximation: For simplicity and to reduce computation time, the TM1 FWC model is used to represent the instrumental background of the merged TM 1 to 7 data. The updated FWC models are generally only provided for TM12346. The FWC models of these TMs are quite similar (see Figure 8), so using the TM1 model for all of them is not expected to cause problems. The TM5 and 7 FWC models, however, differ especially at the low-energy end. According to the eROSITA Early Data Release site[28], they are only valid for energies above 1 keV, while the models for TM12346 are valid between 0.3 and 10 keV. Thus, modelling the instrumental background of merged data including TM5 and 7 with the TM1 model introduces an inaccuracy. Even if the spectra of each TM were fitted separately with the appropriate FWC model, there would be no model representation for the TM 5 and 7 background below 1 keV since the respective models are only valid above this threshold.
The extent of the inaccuracy that arises from the use of the TM1 FWC model for the merged spectra of all TMs in the energy range of 0.3 to 8 keV was estimated, see Appendix A. This was done by fitting the spectrum of the total remnant with the appropriate FWC model[37] and energy range for the data of each TM. Nevertheless, all data was fitted simultaneously. The results were compared to those obtained when using the new TM1 FWC model for all TMs. They were found to be compatible within 1σ uncertainties. Thus, the TM1 FWC model describes the instrumental background of all TMs reasonably well. Therefore, the approximation of using the TM1 model for the merged data of all TMs is used in the further analysis. This reduces the computational effort and simplifies the fitting procedure, especially when it comes to the spatially resolved spectral analysis (Sect. 4). As already stated in Sect. 1.4, also the data of TM 5 and 7 were included in the analysis. The beneficial effect of improved counting statistics is expected to surpass potential inaccuracies related to the higher instrumental background on the low energy end.

[35]`https://wiki.mpe.mpg.de/eRosita/XWPBackground?action=AttachFile&do=view&target=tiger_report_251019.pdf`, accessed 2022-10-17

[36]`https://wiki.mpe.mpg.de/eRosita/XWPBackground`, accessed 2022-10-17

[37]The old FWC models were used in this case since the new ones are not provided for TM 5 and 7

Cosmic X-ray background

The second background component is the cosmic X-ray background that consists of X-ray radiation originating not from the source of interest but from objects that lie behind it or in front of it. There is no universal answer to the question which combination of model components and set of parameters provides the most appropriate representation of the cosmic X-ray background. Thus, the model has to be adjusted for each particular case within certain limitations that are imposed by the request to represent the cosmic X-ray background radiation by reasonably meaningful and sane components from a physics point of view. The aim is to find a model that is sufficiently flexible to represent the important features in the spectrum. At the same time, it should be as simple as possible to avoid over-fitting. If the model has too many degrees of freedom, it meets the requirement of fitting the data well, but the resulting parameter values become arbitrary.
On the one hand, thermal black body radiation of different temperatures, which is represented by the Astrophysical Plasma Emission Code (APEC, Smith et al. 2001), contributes to the cosmic X-ray background. Radiation described by this model is a combination of thermal bremsstrahlung and emission lines produced through electron shell transitions in thin plasma which is in collisional equilibrium. On the other hand, the cosmic X-ray background also comprises radiation that can be modelled as a power law, i. e. the flux decreases exponentially with increasing energy. This model is also used to model the remnant emission itself, see Sect. 1.2.3 and in particular Eq. 1. In the case of the cosmic X-ray background, either non-thermal radiation or emission from hot, highly ionized plasma which does not exhibit prominent line emission from electron transitions can be represented by a power law model.
All cosmic X-ray background model components are described in greater detail in the following paragraph, which is based on Sect. 8.2 in the ESAS cookbook[38]. According to that, the model should comprise an unabsorbed thermal component to account for emission from the Local Hot Bubble that is expected to have a temperature of $kT \sim 0.1$ keV. Further more, there is an absorbed thermal component that represents emission from the hotter halo for which kT is expected to lie between 0.25 and 0.7 keV. Possibly, the emission from the cooler halo has to be modelled with an additional absorbed component ($kT \sim 0.1$ keV). The non-thermal contribution arises predominantly from unresolved background AGN and is represented by an absorbed power law with an index of $\Gamma \sim 1.46$. The cosmic X-ray background was studied in detail by Cappelluti et al. (2017) in the 0.3-7 keV energy range using *Chandra* observations. They found that the AGN emission is best represented by a power law with $\Gamma = 1.45 \pm 0.02$ and a normalization of 10.91 ± 0.16 photons/cm^2/s/sr/keV at 1 keV. According to Doroshenko et al. (2017), this corresponds to a value of $4.6 \cdot 10^{-7}$ photons/cm^2/s/arcmin^2/keV. Since the latter authors used a photon index of 1.46 which is also recommended in the ESAS cookbook, this value was also adopted for the current work. It lies within the uncertainties of the Cappelluti et al. (2017) result. In any case, a difference of ± 0.01 in the photon index does not notably change the shape of the model and is therefore not relevant, especially in background modelling given the large systematic uncertainties related to not precisely constrained temperatures and normalizations of the thermal components. In theory, since the normalization per arcmin^2 is constrained for the AGN power law, this component could just be included as a constant with fixed index and normalization. This was not done for two reasons: First, measurements of the cosmic X-ray background by different instruments differ for various reasons. Consequently, the overall normalization of the cosmic X-ray background is still not undoubtedly constrained (Cappelluti et al., 2017). And second, since HESS J1731-347 is located near the Galactic plane, the Galactic Ridge X-ray Emission (GRXE) is also expected to contribute to the cosmic X-ray background. E. g. Revnivtsev (2003) found that the bulge component of the GRXE in the 3-20 keV range is a power law with an index of $\Gamma \approx 2.1$. Thus, there is indication that the GRXE can be modelled by a power law with a photon index reasonably close to that of the unresolved background AGN radiation ($\Gamma = 1.46$). Fixing the normalization of the AGN power law

[38] `https://heasarc.gsfc.nasa.gov/docs/xmm/esas/cookbook/xmm-esas.html`, accessed 2022-04-28

to the value that was found by Cappelluti et al. (2017) might introduce a systematic uncertainty given that it was derived from data of a different instrument. Another aspect is that it is favourable to keep the background model as simple as possible. Since the photon indices of the unresolved AGN power law and of that representing the GRXE are similar and no precise value for the GRXE index could be found without extensive investigation, the components were represented by one common power law in order to simplify the model. Therefore, the normalization of the AGN power law was left free for the background fit in order to include both the AGN radiation and the GRXE. The photon index was frozen to 1.46 (see above). When fitting only the spectrum of the source region (see Sect. 3.3.4), the norm had to be frozen to the result of the background region fit[39], since it was not possible to disentangle the contribution of the AGN and GRXE power law from the remnant emission, which has a similar photon index. In an internal document on the eROSITA wiki[40], written by Dominique Eckert, the cosmic X-ray background in eROSITA TM6 observations of the *Ultra-Deep Survey area* (UDS) is also modelled by an absorbed power law with index 1.46 and free normalization, an absorbed thermal component for the Hotter Halo which has $kT \approx 0.26$ in the best fit and an unabsorbed thermal component with $kT \approx 0.09$ in the best fit for the Local hot Bubble. These values are in agreement with those suggested in the ESAS cookbook (see above). Similar values were also reported by Cappelluti et al. (2017) who found $kT \approx 0.27$ keV for the absorbed hotter halo emission and $kT \approx 0.07$ keV for the Local Hot Bubble.

All in all, the references discussed above give a pretty clear picture at least of the background model components used. Also, the temperatures of the thermal emission are pretty consistent. It might of course well be that the results are influenced by one another. However, digging deeper into background modelling is beyond the scope of this Thesis and the prime goal is to find a model which gives a good representation of the background without relying on obviously unphysical parameters.

Since there are several possibilities for setting up the cosmic X-ray background, several attempts were made, also including a second absorbed thermal component for the cooler halo as suggested in the ESAS cookbook. However, the background spectrum turned out to be already well represented by a model without this component. Thus, it was dropped to reduce the number of free parameters and keep the model reasonably simple. The fitting procedure of the background spectrum with the total background model including the instrumental component is described in detail in Sect. 3.3.3. The fitting is only mentioned here since the results influenced the model selection for the cosmic X-ray background. The final model used to represent the cosmic X-ray background emission is therefore:

$$\text{cosmic\_bkg} = \underbrace{\text{apec\_kt01}}_{\text{local hot bubble}} + \text{nh\_bkg}(\underbrace{\text{apec\_kt03}}_{\text{hotter halo}} + \underbrace{\text{pl146}}_{\text{AGN+GRXE}}) \tag{3}$$

where *apec_kt01* is a thermal model component with a temperature of $kT \sim 0.1$ keV, represented by the XSPEC APEC emission spectrum of a collisionally ionized gas. *apec_kt03* is the same with an expected temperature of $kT \sim 0.3$ keV, *nh_bkg* is the absorption, again using the *tbabs* model as for the background subtracted fit in Sect 3.2, and *pl146* is the power law with index frozen to 1.46.

Total background model

Having defined the instrumental background and the cosmic X-ray background model earlier in this section, now the total background model can be settled:

$$\text{total\_bkg} = \text{instrumental\_bkg} + \text{cosmic\_bkg} \tag{4}$$

[39] and rescaled accordingly

[40] `https://wiki.mpe.mpg.de/eRosita/ScienceRelatedStuff/Background?action=AttachFile&do=view&target=uds_background_171019.pdf`, accessed 2022-07-12

with the definition of *cosmic_bkg* in Eq. 3. As mentioned in the respective paragraph, the instrumental background is scaled with a constant factor named *scaling.factor* to account for the fact that the extraction area of the analysed spectra is smaller than the total field of view of eROSITA. Thus, not the total information collected by the CCDs is considered which leads to a lower instrumental background. Further, the cosmic background has to be convolved by the Ancillary Response File (ARF) produced during spectrum extraction while the instrumental background does not. This is realized by using the sherpa *set_full_model()* command following an article in the sherpa manual[41] which gives an example of fitting a data set with model components convolved by different response files. The instrumental background was convolved with a unit ARF and the cosmic background with the unchanged ARF file produced during spectrum extraction.

3.3.2. Source model

The emission of the supernova remnant HESS J1731-347 is thought to be purely non-thermal (as already mentioned in Sect. 1.2.4) and can therefore be described by an absorbed power law:

$$\text{source\_emission=nh\_src} \cdot \text{pl\_snr} \quad (5)$$

The absorption *nh_src* is again represented by the *tbabs* model and XSPEC model components provided within sherpa are used. The photon index of the power law, averaged over the entire source, was found to be $\Gamma_{SNR} = 2.66 \pm 0.01$ by Doroshenko et al. (2017). As a simplification, it was assumed that the absorption is dominated by the matter between the source and the observer, meaning that in the source region, source and background can be modelled with the same absorption. This would not be true for the local hot bubble, which is a low-density region in space containing the solar system and therefore its emission is much less absorbed than that of the remnant. However, the contribution of the local hot bubble is modelled as a completely unabsorbed APEC and thus not affected by the assumption of equal absorption for source and background radiation in the source region.
When fitting the background spectrum extracted from the annular region around the source (see Fig. 2), the absorption might be different from that in the source region. Doroshenko et al. (2017) found spatial variations of N_H from $1.1 \cdot 10^{22}$ to $3.0 \cdot 10^{22}$ atoms/cm^2 in the sky region comprising the source and its immediate surroundings. Therefore, two different absorption column densities were used for the source and background area.

3.3.3. Fit of the background spectrum

The statistics used for the fit of the background spectrum as well as for the simultaneous fit of source and background was the *cstat* statistics. It is better suited for data with low counting statistics than the χ^2 statistics. The latter requires that the distribution of the counts in each bin after grouping follows a normal distribution. For a sufficiently high number of counts, this request is fulfilled: According to the central limit theorem of probability theory, for a sufficiently high number of counts, each probability distribution tends towards a normal distribution. There is no universal guideline on how many counts are required that χ^2 statistics can be applied and give a reliable result. In doubtful cases or cases of clear low number statistics like the merged eRASS 1 to 4 spectrum of HESS J1731-347, the *cstat* statistics yields more reliable results. It is adapted to the counts in each bin not being normally distributed but following a Poisson distribution as it is the case for low number statistics.

The background model has 6 free parameters (a normalization and temperature for each of the 2 APECs, the normalization of the AGN/GRXE power law and the absorption column density) and some of them are correlated (e. g. a higher absorption in combination with a higher normalization can lead to a comparably well-fitting model). Setting the parameters to meaningful values at the beginning

[41] `https://cxc.cfa.harvard.edu/sherpa/threads/manual_source/`, accessed 2022-07-14

helps the fitting procedure to find the minimum of the statistics value faster and therefore decreases the probability to get stuck in a local minimum. To get a feeling for the effect of thawing different parameters, the fitting procedure was repeated several times, unfixing more and more parameters. At the beginning, the APEC temperatures were frozen to $kT = 0.3$ keV for the absorbed component and $kT = 0.1$ keV for the unabsorbed component and the absorption fixed to $N_H = 1.5 \cdot 10^{22}$ atoms/cm^2. The value for the absorption is motivated as follows: Doroshenko et al. (2017) found for their two background regions next to the remnant in eastern direction similar values of $N_H \approx 1.1 \cdot 10^{22}$ atoms/cm^2 and for the one background region to the right of the remnant $N_H \approx 3.0 \cdot 10^{22}$ atoms/cm^2. So, as a side remark, there are clearly strong local variations of N_H also in the sky region surrounding HESS J1731-347. The spectrum of the background annulus illustrated in Fig.2 is expected to be dominated by emission from the less absorbed left part. Thus, N_H should be close to $1 \cdot 10^{22}$ atoms/cm^2. The *tbabs* model is used in the analysis of this Thesis, which requires the abundance values of Wilms et al. (2000), while Doroshenko et al. (2017) used the *wabs* model with the abundances of Anders and Ebihara (1982). For the background subtracted fit in Sect. 3.2, the abundances of Wilms et al. (2000) yielded a higher absorption, and therefore, a slightly larger starting value of $N_H = 1.5 \cdot 10^{22}$ atoms/cm^2 was selected. So, in the first step, only the normalizations of the two thermal components and of the power law representing the unresolved background AGN emission and the GRXE were left as free parameters. Since the fit showed strong residuals on the low-energy end, in the next step, the temperature of the *apec_kt01* component was thawed. Since the correspondence between model and data was still poor below $\approx$ 1 keV, the temperature of *the apec_kt03* temperature was also thawed. To adjust the fit further, also the absorption was allowed to vary in the last step. For this final fit, the method was set to *simplex* and the uncertainties of the parameters have been calculated with the *conf()* method. For the previous steps, no error calculation was carried out and the fit method used was *levmar* since it is faster and these were just intermediate steps.
Figure 9 shows the final fit of the background spectrum. The results and errors for all free parameters are listed in Table 2. The errors correspond to the 1σ confidence intervals. The absorption is smaller than expected from the considerations explained above ($N_H = 0.98^{+0.12}_{-0.14}$). It is in fact in good agreement with the results Doroshenko et al. (2017) found for their background regions (assuming that the less absorbed regions dominate the total background emission). However, a larger value was expected due to the different abundances. The temperature of the absorbed APEC converged to $kT \approx 0.65 \pm 0.04$ which is close to the maximum expected value according to the ESAS cookbook ($kT \leq 0.7$). A detailed interpretation of the background parameter results is beyond the scope of this Thesis. Judging from the plot in Fig. 9, the model represents the data reasonably well with some deviations around 2 keV and 0.6 keV. The best fit has a reduced statistics value of 0.97. According to the sherpa documentation, a reduced statistics value on the order of 1 indicates a good fit also for the *cstat* statistic[42]. Therefore, the prime requirement of finding a reasonable model representation for the background is fulfilled and paves the way to move on with the combined source and background emission fit in the next section.

[42] `https://cxc.cfa.harvard.edu/sherpa/statistics/#cstat`, accessed 2022-07-14

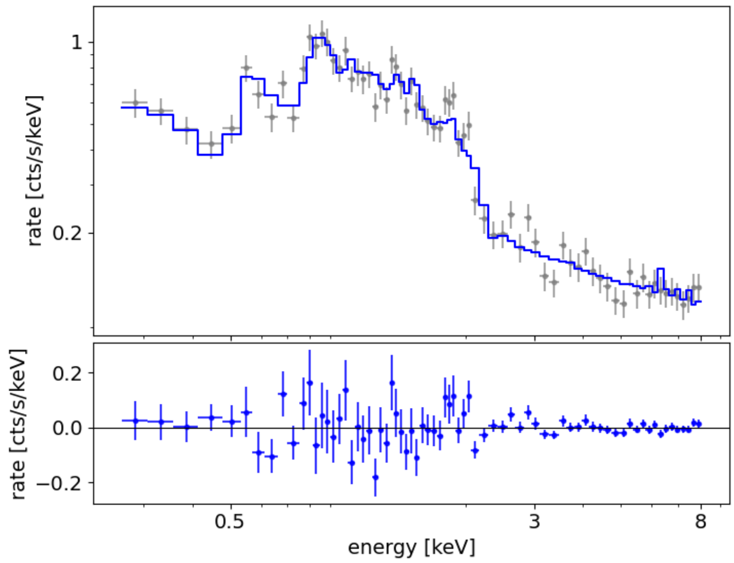

Figure 9: Best fit of the background spectrum extracted from an annulus with inner radius 17.5′ and outer radius 24.7′, centered on the CCO of HESS J1731-347. The data is grouped to 70 counts per bin for the plot. The fit was carried out with the data grouped to 1 count per bin (minimum request of *cstat* statistics). The spectrum was fitted in the energy range of 0.3-8.0 keV since in all this range, there is background emission, even though there is only a low count rate dominated by the instrumental background above ~ 5 keV. The lower panel shows the deviation between model and data in units of counts/s/keV. A plot of the weighted residuals, i. e. (data-model)/error as displayed in Fig. 6 for the background subtracted fit, is not available for the *cstat* statistic.

Table 2: Best fitting parameters for the background fit.

parameter	value	lower error	upper error
apec_kt01.kT$^{(a)}$	0.20	-0.01	+0.01
apec_kt03.kT$^{(a,*)}$	0.65	-0.04	+0.04
nh_bkg.nH$^{(b)}$	0.98	-0.14	+0.12
scaling.factor	0.53	-0.01	+0.01
apec_kt01.norm$^{(c)}$	0.00066	-0.00005	+0.00005
apec_kt03.norm$^{(c)}$	0.006	-0.002	+0.002
pl146.norm$^{(c)}$	0.0028	-0.0002	+0.0002
red. stat.	0.97		

$^{(a)}$in units of keV $^{(b)}$ in units of 10^{22} atoms/cm^2 $^{(c)}$ in units of photons/s/cm^2/keV

*The component is expected to have a temperature between 0.25 and 0.7 keV and was named arbitrarily *apec_kt03* before the fit result was known.

3.3.4. Fit of the source area spectrum

The combined source and background spectrum extracted from the source area was also fitted in the 0.3-8.0 keV energy range since background photons are present over this entire range and thus, choosing a larger range than for the background subtracted fit (see Sect. 3.2) helps to better constrain the spectrum. The simultaneous fitting of source and background emission is based on the assumption that the background spectrum in the source region can be described by the same model as the spectrum extracted from the background annulus. However, the cosmic X-ray background might change locally,

which would require a different set of parameters. As already mentioned, the absorption column density is expected to be different for the source and background region. Also, the normalizations of the components might differ due to a different extraction area or intrinsic surface brightness variations. In a first attempt, the cosmic background model parameters were frozen to the best-fitting values found in Sect. 3.3.3, rescaled with a constant factor corresponding to the area ratio of the source and background extraction regions: area(src)/area(bkg)≈ 1.10 (see Sect. 3.1). This ratio was calculated from the REGAREA keywords of both spectra, which contains the geometric area of the extraction region without considering that potentially only a certain fraction of the extraction area is in the field of view during the GTI. This distinguishes the REGAREA from the BACKSCAL, which is used to rescale the instrumental background. The reason for the different scaling is that the partial visibility of the source during the GTI is also accounted for by folding the model with the Ancillary Response File (ARF). Since this is done for the cosmic X-ray background model, but not for the instrumental background model, the cosmic X-ray background model has to be scaled by a factor not including the partial visibility. Otherwise, the effect would be accounted for twice.[43]
The first fit iteration, in which the cosmic X-ray background model parameters were all frozen to the results obtained from the background region fit and rescaled by the REGAREA ratio, had the purpose to to evaluate how well the source region spectrum can be fitted with this approach. The absorbed power law representing the source emission was added with the photon index frozen to $\Gamma_{SNR} = 2.66$ which was the result of Doroshenko et al. (2017). The absorption was also frozen in the first step to a value of $N_H = 1.5 \cdot 10^{22}$ atoms/cm^2. The norm of the source emission power law was left as a free parameter. The instrumental background was rescaled by the BACKSCAL ratio. The plot and residuals of this first fit are shown in Fig. 10 in red. The model already fits the overall shape of the spectrum, but there are several clear residuals. Unfixing N_H did not lead to an improvement of the fit. Also, unfixing Γ_{SNR} while N_H was frozen did not improve the systematic residuals between 1 and 2 keV. Therefore, in the next step, Γ_{SNR} and N_H were thawed. The fit and residuals are displayed in Fig. 10 in blue. Just below 2 keV, the residuals are still prominent. The best-fitting parameters of the fits in Fig. 10 are given in Table 3. The result for Γ_{SNR} is not compatible within the 1σ confidence range with the result of Doroshenko et al. (2017) as well as with the result of the background subtracted fit ($\Gamma_{SNR} = 2.77^{+0.23}_{-0.22}$). N_H is also significantly lower at 1σ than in the background subtracted fit and $norm_{SNR}$ is just half the value of the background subtracted fit.

Table 3: Best-fitting parameters for the source region spectrum with the background parameters frozen to the results of the background region fit, see Table 2.

	N_H, Γ_{SNR} frozen			N_H, Γ_{SNR} thawed		
parameter	value	lower err.	upper err.	value	lower err.	upper err.
pl_snr.PhoIndex	2.66	–	–	2.15	0.08	0.08
pl_snr.norm$^{(b)}$	0.035	0.001	0.001	0.023	0.002	0.002
nh_src.nH$^{(a)}$	1.5	–	–	1.29	0.03	0.03
red. stat.	1.10			1.06		

$^{(a)}$in units of 10^{22} atoms/cm^2 $^{(b)}$ in units of photons/s/cm^2/keV

In principle, both methods should give comparable results since the same physical phenomenon is described. However, both of them have caveats that can explain the deviations. For the background subtracted fit, possible sources of systematic errors have been described in Sect. 3.2. For the simultaneous fit, there is an increased number of model parameters due to the inclusion of the background model. Since many of these parameters are correlated with the source model parameters, the fit result is highly affected by the choice of the background model parameters. Therefore, in the first approach the cosmic X-ray background model parameters were frozen to the values found for the spectrum of the background region. However, the downsides of this approach are that first, the best-fitting parameters of the background model also have uncertainties which are not accounted for when they are fixed in

[43] `https://wiki.mpe.mpg.de/eRosita/XWP%20Background%20Modeling`, accessed 2022-10-20

the source region fit. And second, there might be a quite different set of parameters describing the background spectrum similarly well and leading to different results in the simultaneous fit since the count statistics of the background spectrum are not that good and the model has 7 free parameters, some of which are correlated.

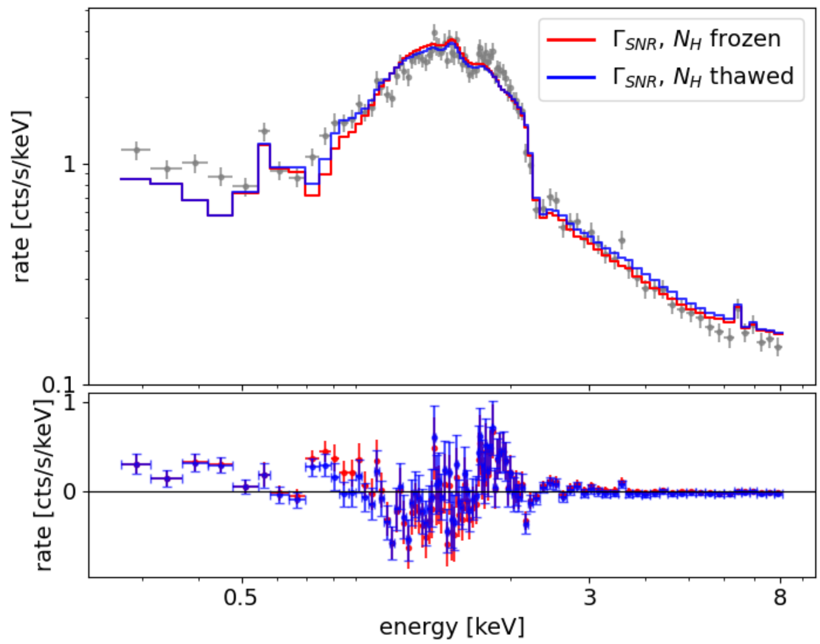

Figure 10: Over-plot of the first two fits of the source region spectrum with the cosmic X-ray background model parameters frozen to the values given in Table 2, rescaled to the source area by using the area ratio of the two extraction regions. The instrumental background was renormalized by the BACKSCAL ratio. The normalization of the source emission power law is thawed in both fits. *Red model:* The photon index is frozen to $\Gamma_{SNR} = 2.66$, the absorption to $N_H = 1.5 \cdot 10^{22}$ atoms/cm^2. Details see Sect. 3.3.4. *Blue model:* Γ_{SNR} and N_H are thawed. These initial fits are meant to evaluate how good the background model found in Sect. 3.3.3 is in agreement with the combined source and background emission in the source region under the assumption that the source emission can be described by and absorbed power law.

Since it is not guaranteed that the background model found in Sect. 3.3.3 is a uniquely good representation of the background and there are still clear residuals in the fit of the source region spectrum even for a thawed photon index and absorption (see blue model in Fig. 10), the fit of the source region was re-done with unfixed temperatures and normalizations of the two thermal background components and the scale factor of the instrumental background[44]. Unfixing the normalization of the *pl146* representing the unresolved background AGN and the GRXE in the source region fit was not feasible since it converged to 0 for the best fit. The reason is that disentangling the contribution of this component from the remnant power law which has a similar index is very difficult in general and especially for low count statistics as in this case. Thus, the remnant power law accounts for both the remnant emission and the non-thermal background component if the normalization of

[44]The FWC scaling factor in the source region was linked to that in the background region via the BACKSCAL ratio. Therefore, to make the parameter results of the source and background region easily comparable, the background region scaling factor was added to the source region model, multiplied by 0. In this way, it is optimized during the fit of the source region, even though it is not a direct part of the source model. The same formalism was also applied in the spatially resolved fit to link parameters between regions, see Sect. 4.2.1.

the latter is kept free. Therefore, it was frozen to the value of the background spectrum fit (see Table 2).

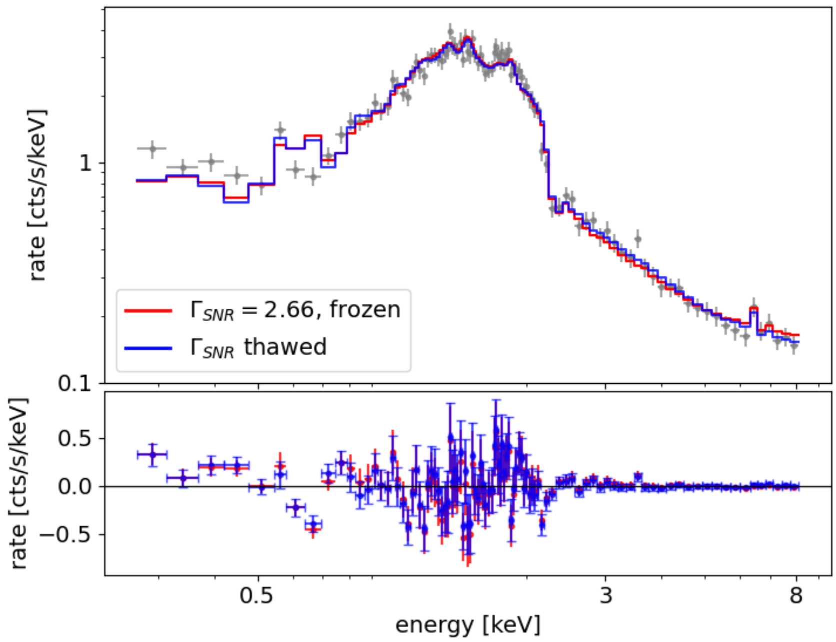

Figure 11: Fit of the source region spectrum when leaving the temperatures and normalizations of the thermal cosmic X-ray background components and the scale factor for the instrumental background free. For the red model, the Photon index is frozen to the result of Doroshenko et al. (2017). For the blue model, the photon index is allowed to vary. N_H is a free parameter in both fits. The best-fitting parameters are given in Table 4. The residuals for a frozen and free photon index are nearly identical. Thus, the characteristics of the source region spectrum are in agreement with the photon index found by Doroshenko et al. (2017).

Table 4: Best-fitting parameters for the fits of the source region spectrum shown in Fig. 11. Errors correspond to the 1σ confidence bounds, calculated with the *conf()* command in sherpa.

	N_H thawed, Γ_{SNR} frozen			N_H thawed, Γ_{SNR} thawed		
parameter	value	lower error	upper error	value	lower error	upper error
nh_src.nH$^{(b)}$	1.86	-0.06	+0.06	1.69	-0.12	+0.09
pl_snr.PhoIndex	2.66	–	–	2.22	-0.14	+0.12
apec_kt01.kT $^{(a)}$	0.25	-0.01	+0.01	0.23	-0.01	+0.01
apec_kt03.kT $^{(a)}$	0.72	-0.05	+0.05	0.68	-0.06	+0.05
pl_snr.norm$^{(c)}$	0.036	-0.001	+0.001	0.027	-0.003	+0.002
apec_kt01.norm$^{(c)}$	0.00092	-0.00005	+0.00005	0.00090	-0.00005	+0.00005
apec_kt03.norm$^{(c)}$	0.029	-0.006	+0.007	0.026	-0.006	+0.007
scale_bkgreg.factor	0.51	-0.01	+0.01	0.48	-0.02	+0.02
red. stat.	1.02			1.00		

$^{(a)}$in units of keV $^{(b)}$ in units of 10^{22} atoms/cm^2 $^{(c)}$ in units of photons/s/cm^2/keV

The fits and residuals for unfixing the parameters of the thermal background components in the source region fit are shown in Fig. 11. For the red model, the photon index is still frozen to Γ_{SNR} = 2.66. The absorption is thawed since it considerably reduced the residuals. For the blue model, Γ_{SNR} is also thawed. The best-fitting parameters for both cases are given in Table 4. Errors correspond to the 1σ confidence ranges of the parameters, calculated with the sherpa *conf()* command and the *simplex* method. The residuals are more balanced in Fig. 11 than in Fig. 10, i. e. a good fit seems only possible when thawing the normalizations and temperatures of the background APECs. Particularly, the peak right below ∼2 keV is reflected better by the model with thawed background parameters. The residuals do not increase notably for the photon index frozen to $\Gamma_{SNR} = 2.66$ (see Fig. 11). The value of the reduced fit statistics is also equal at an accuracy of two decimal places. This means that the source region spectrum is roughly in agreement with the photon index of the remnant found by Doroshenko et al. (2017) and therefore also with the result of the background subtracted fit (Sect. 3.2) when the background model parameters are adjusted accordingly. This illustrates the difficulty of the simultaneous fitting of source and background emission: There are many free parameters that influence each other and make it hard to constrain the characteristics of the source emission without considering the results of previous studies or other methods as indication.

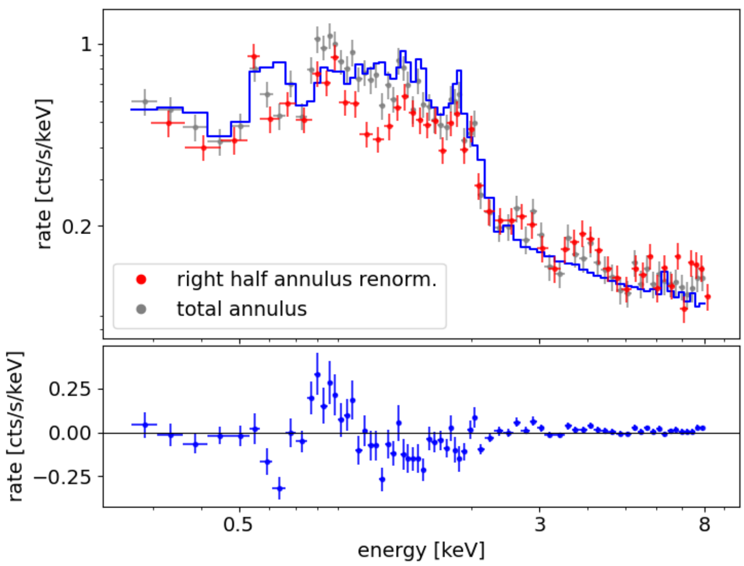

Figure 12: Blue: background model re-fit with the temperatures and normalizations of the thermal cosmic X-ray background components frozen to the best-fitting values of the source region fit (see Table 4). The parameter values for the thawed Γ_{SNR} are used. However, the result is not much different when using those for the frozen Γ_{SNR}. The only free parameter is the absorption column density N_H. The scale factor of the instrumental background was also frozen to the best-fitting value of the source region fit, under consideration of the BACKSCAL ratio. The model is clearly not representing some parts of the spectrum very well. The spectrum plotted in grey is that extracted from the total background annulus shown in magenta in Fig. 5, which is the basis for the fit. Over-plotted in red is the spectrum extracted from the stronger absorbed right half annulus (see also Fig. 5), renormalized to the area of the total annulus. The purpose is to compare the shape of the background spectrum for different absorptions.

The fact that the residuals are more balanced in Fig. 11 than in Fig. 10 clearly indicates that the background model found in Sect. 3.3.3 is for some reason not a good representation of the background in the source area under the assumption that the model for the source emission is appropriate. This rises a related question: Does the background model with the best-fitting parameters of the source region fit represent the background spectrum reasonably well? To evaluate this, the background spectrum was

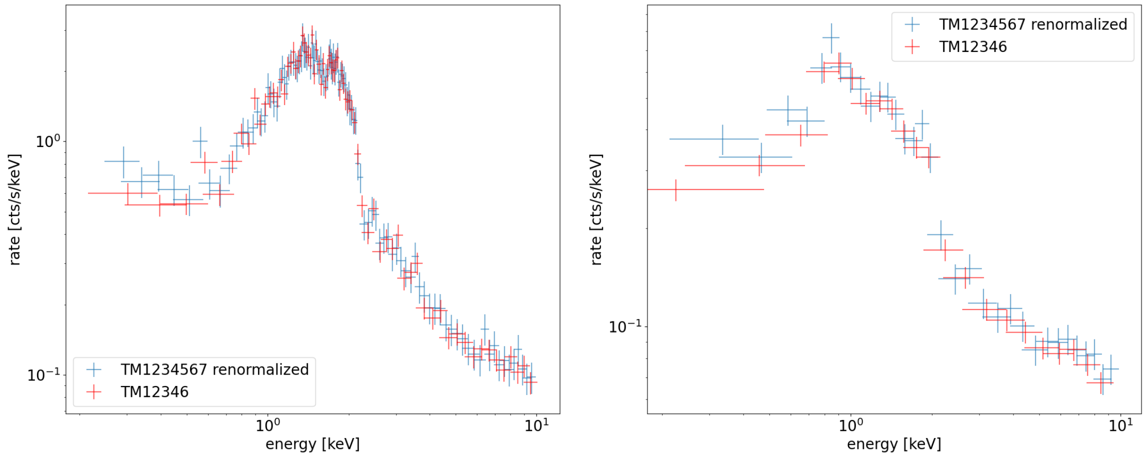

Figure 13: Source (left) and background (right) spectrum for all 7 TMs and only those possessing an on-chip filter (namely TM12346). The background spectrum is grouped to at least 70 counts per bin, the source spectrum to at least 100 counts per bin. The spectrum of all TMs is renormalized by a factor of 5/7 for better comparison. There are no major differences in the shapes of the spectra. However, an excess at the soft energy and can be observed, especially in the source spectrum, when TM5 and 7 are included. This is probably due to the fact that for these two TMs the instrumental background is more prominent in the soft energy regime (see Figure 8).

re-fit with the temperatures and normalizations of the cosmic X-ray background APECs frozen to the results of the source area fit (see Table 4 right). Only the scaling of the instrumental background and the absorption were left free. The resulting best-fit model is shown in Fig. 12. There are prominent residuals around 1 keV. Around ~ 0.8 keV, the model systematically underestimates the count rate. Also for energies above 3 keV, the model count rate is too low. Since the spectrum is dominated by the instrumental background in this energy range, there seems to be a small inaccuracy when scaling the instrumental background from the source to the background extraction region. This is also indicated by Fig. 10, where the source model count rate is too high in the same energy range when freezing the scale to the background region result. Overall, the spectrum extracted from the background annulus cannot be represented accurately by the model with the best-fitting parameters of the source region fit - even for a different absorption. The absorption converged to $N_H = 1.76^{+0.03}_{-0.02} \cdot 10^{22}$ atoms/cm^2 which is a significantly higher value than that obtained for the initial background fit in Sect. 3.3.3. According to the different results of the background subtracted fit that were caused by the abundance selection required for the *wabs* and the *tbabs* absorption model (Sect. 3.2), the *wabs* model tends to result in lower N_H values. For the background subtracted fit, the difference was $\approx 5 \cdot 10^{21}$ atoms/cm^2. Therefore, the larger value of $N_H = 1.76^{+0.03}_{-0.02} \cdot 10^{22}$ atoms/cm^2 for the background spectrum is in better agreement with the fact that Doroshenko et al. (2017) found an absorption of $N_H \sim 1.1 \cdot 10^{22}$ atoms/cm^2 even for the less absorbed background area in the eastern vicinity of the remnant. Nevertheless, the fit in Fig. 12 with the APEC temperatures and normalizations and instrumental background scaling frozen to the best-fitting values of the source area fit[45] clearly does not represent the background spectrum as well as the one in Fig. 9. This indicates that the emission that is present in the source region besides the radiation from the remnant itself somehow differs from the radiation in the background region. One possible difference is likely the absorption in the two regions which is expected to affect the various components of the background model in different ways. The emission of the local hot bubble, for example, which is modelled by an unabsorbed APEC with a temperature of ~ 0.2 keV, is not affected at all, while the shape of other model components is changed. To get an idea how

[45] and rescaled accordingly

a stronger absorption might change the shape of the background spectrum, the spectrum extracted from the stronger absorbed right half annulus (see Fig. 5) is over-plotted in Fig. 12 in red. It was renormalized to the area of the total annulus using the BACKSCAL ratio. As it can be expected from the considerations above, the background spectrum does not simply differ by showing a lower count rate for a higher absorption. In fact, at the high and low energy end, the count rate is not lower at all, since it is dominated by the instrumental background and, at the low end, also the unabsorbed APEC representing the local hot bubble emission. These components are not affected by a higher absorption. In contrast to that, the shape of the background spectrum extracted from the stronger absorbed right half annulus differs considerably from that of the total annulus between ~ 0.7 and ~ 1 keV. Around 0.8 keV, the background model with all parameters but the absorption frozen to the best-fitting values of the source region fits the right half annulus background spectrum better that the total one, since the latter shows a peak that is not reflected in the model. However, approximately between 0.8 and 1 keV, the model count rate is considerably higher than that of the right half annulus spectrum. Therefore, it is not the case that the model clearly represents the red spectrum better than the grey one. As remark, the difference in the shape could also be caused by local variations in the background radiation not related to the absorption. Actually, different absorption column density for the source and background region is already introduced in the model, which should account for absorption-related effects. Thus, at this point, there is no definite answer why the best-fitting background model of the source region considerably deviates from that of the background region. In general, fitting the source and background area spectrum each with a constant absorption is only an approximation since the absorption varies strongly as a function of the location (Doroshenko et al., 2017).
In order to find a background model which agrees as well as possible with both spectra, the source and background region spectra were fitted simultaneously in the following Sect. 3.3.5.

When looking again at the source models shown in Fig. 11, it stands out that both of them still overestimate the count rate around 0.6 keV. On the other hand, the rate is underestimated below ~ 0.5 keV. From looking at the instrumental background of the 7 eROSITA telescope modules in Figure 8, this might be related to the fact that the TM1 FWC model is used to describe the instrumental background of the merged data set. The contribution of TM5 and 7 to the background below ~ 1.5 keV is clearly stronger than that of TM1. This could be the reason for the excess at soft energies in the merged spectrum that is not accounted for by any model component. In fact, when comparing the source and background spectra with and without the contribution of TM 5 and 7 as shown in Figure 13, there is a notable excess in the source spectrum at the low-energy end when TM5 and 7 are included. In the background spectrum, the difference is not so clearly visible by eye. This might be due to the low number of counts and therefore large error bars in the low energy regime. In principle, if the effect is indeed due to the higher instrumental background of TM 5 and 7, it is expected to manifest to the same extent also in the background spectrum.

Some further investigations were conducted in order to find further indication that the soft excess of the source spectrum with respect to its model could be related to the stronger instrumental background of TM5 and 7 in the corresponding energy range. This is described in Appendix C. The effect of that phenomenon on the best-fitting parameters was also evaluated by performing the fit on TM 12346 data only. However, it was not done for the fit of the source region only, but for the simultaneous fit of the source and background region spectra that is explained in the following Sect. 3.3.5. The reason is that the values for the cosmic X-ray background parameters that were used in the spatially resolved spectral analysis (Sect. 4) were the ones obtained from the simultaneous fit of the source and background region spectra. Therefore, it is reasonable to investigate those results in closer detail. To anticipate the key results of the comparison: First, the excess of the data with respect to the source model is indeed less prominent when excluding TM 5 and 7 data (see Fig. C1). Second, no significant differences in the parameters of the source or cosmic X-ray background model were found at the 1σ

level for including or excluding TM 5 and 7.

3.3.5. Simultaneous fit of source and background area spectra

Fitting the two spectra extracted from the source and the background area simultaneously has the advantage that the photons from both regions are considered to constrain the background model parameters. This is expected to result in a higher accuracy since the counting statistics are improved. The cosmic X-ray background model with the resulting parameters should enable a good representation of both the background spectrum (see Sect. 3.3.3) and the the source area spectrum (Sect. 3.3.4), provided that the model selection is appropriate. One has to keep in mind, however, that the result of the simultaneous fit is dominated by the agreement with the source area spectrum since it has a higher number of counts which makes it favourable for the model to represent its characteristics better than those of the background spectrum.

The model used for the background spectrum is the one described in Eq. 4. The one for the source region spectrum is the same as in Sect. 3.3.4, explicitly:

$$\text{srcreg\_model} = \text{scale\_cosmic} \cdot \text{cosmic\_bkg} + \\ +\text{scale\_fwc} \cdot \text{instrumental\_bkg} + \text{source\_emission} \quad (6)$$

where *scale_cosmic* is the the area ratio of source to background region[46] and *cosmic_bkg* and *source_emission* are defined in Eq. 3 and 5, respectively. *scale_fwc* is the BACKSCAL ratio of the source to background region, which is used to scale the instrumental background since it is not folded by the ARF.
It should be noted that two different absorption column densities are allowed in the model: *nh_bkg* for the cosmic X-ray background emission originating from the background area and *nh_src* for all emission originating from the source area, i. e. the source emission and the underlying cosmic X-ray background radiation. This is justified by the previously mentioned spatial variations of N_H in the field of view found by Doroshenko et al. (2017). In the first fit, the only free parameters are the instrumental background scale in the background region, the two absorption column densities and the normalization of the remnant power law. All other parameters are frozen to the values of the source region fit (see Table 4 left) and rescaled accordingly for the background region. The normalization of the AGN/GRXE power law was still frozen to the result obtained from the background region fit (see Table 2) since it was not possible to disentangle its contribution from the source emission in the source region only fit. Given that the other cosmic X-ray background parameters changed in the source region fit, the normalization of the AGN/GRXE power law was unfixed in the next step to adjust it to the new values. For the simultaneous fit, the result was >0, thus it was possible to distinguish between the *pl146* contribution and that of the remnant emission. In the next step, the normalizations of the thermal cosmic X-ray background components were thawed, followed by the temperatures. Only in the last step, the photon index of the remnant emission Γ_{SNR} was unfixed which has been fixed to 2.66 in all previous fits. The best-fitting models for the first and last iteration are shown in Fig. 14. Since in the first iteration many parameters are frozen to the best-fitting values for the source region, the residuals are not expected to improve between the first and last iteration for the source region spectrum. On the other hand, they do not increase notably either. For the background emission, however, the best-fitting model of the last iteration is clearly a better representation of the spectrum. Thus, by fitting the source and background region spectrum simultaneously, the best-fitting parameters for the model allow a representation of the background spectrum that is much better than that achieved with the result from the source region fit (see Fig.12). At the same time, the agreement with the source region spectrum is not much worse than in the source region only fit (see Fig. 11). Therefore, taking

[46]determined from the REGAREA fits header keyword

advantage of the additional photons from the background region to constrain the background model parameters makes the fit more reliable. The best-fitting parameters for the simultaneous fit are given in Table 5. The model overestimates the count rate for the source region spectrum around 0.6 keV and underestimates it between 1 keV and 2 keV.

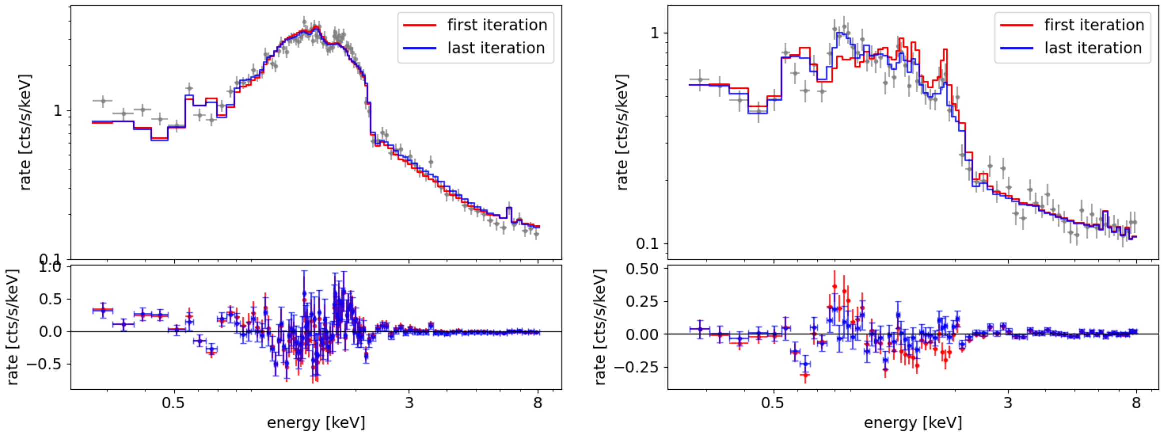

Figure 14: Source region (left) and background region (right) spectrum and best-fitting models for the simultaneous fit of both data sets. In the first iteration (red), all parameters except for the normalization of the remnant power law, the absorption column densities and the scaling factors for the instrumental background are frozen to the best-fitting values of the source region fit (Table 4 left). In the last iteration (blue), all parameters including Γ_{SNR} are thawed. The best-fitting values for the last iteration are given in Table 5 right.

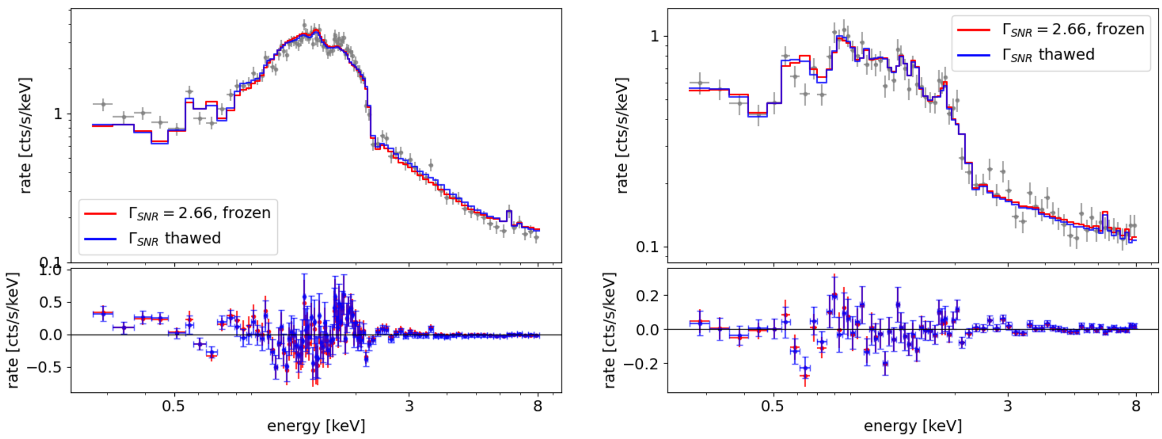

Figure 15: Source region (left) and background region (right) spectrum best-fitting models for the simultaneous fit of both data sets. For the red model, $\Gamma_{SNR} = 2.66$ is frozen. In the blue model, Γ_{SNR} is thawed. The best-fitting parameter values for both cases are given in Table 5. All other parameters are thawed except for the photon index of the AGN and GRXE power law ($\Gamma = 1.46$).

The best-fitting model with Γ_{SNR} frozen to 2.66 in comparison to that for an unfixed Γ_{SNR} is shown in Fig. 15. The agreement of model and data is not considerably worse for the photon index frozen to the result of the XMM study of Doroshenko et al. (2017). Also, the reduced statistics values are almost equal for both cases (see Table 5), so from a statistical point of view, none of the models is clearly preferable to the other. For the parameter results, there are significant differences at the 1σ

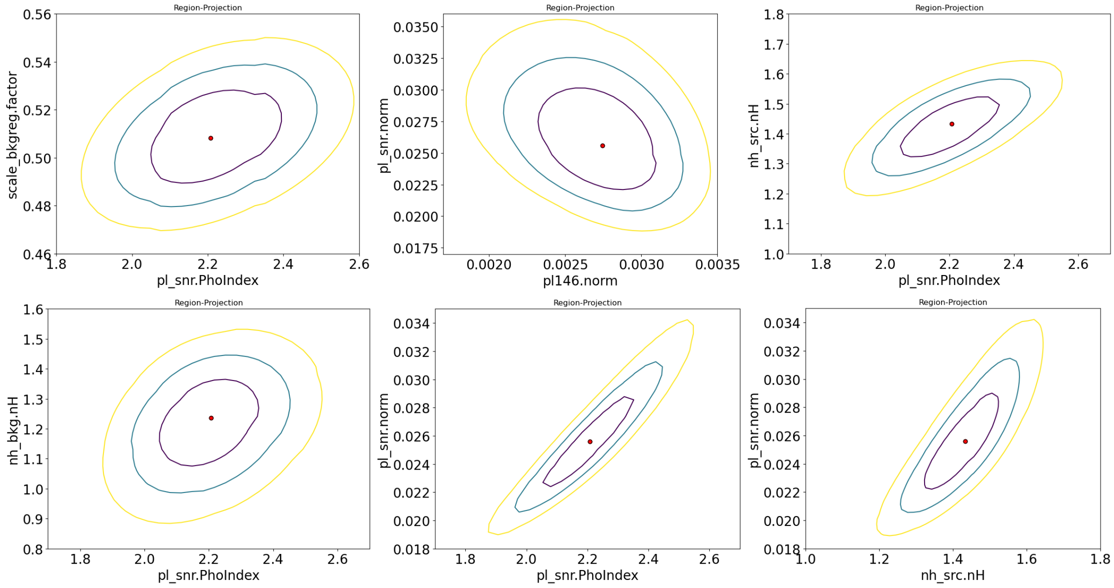

Figure 16: Contour plots for the simultaneous fit of the source and background region spectrum (see Fig. 14 and Table 5) for a thawed photon index Γ_{SNR}. Except for the last plot on the lower right, the quantity on the $x-$axis is always the photon index Γ_{SNR}. Parameters on the $y-$axis from upper left to lower right: FWC scaling for the background region (the scaling for the source region is not a free parameter, see Sect. 3.3), normalization of the GRXE and background AGN powerlaw (*pl146*), absorption column density N_H in the source region and background region and normalization of the source emission power law. The last contour plot on the lower right involves the absorption column density N_H in the source region on the $x-$axis and the normalization of the remnant power law on the $y-$axis. There are at least slight correlations evident between all the parameter pairs shown. The remnant power law photon index is strongly correlated with its normalization (lower middle plot), which is itself strongly correlated with the absorption column density in the source region (lower right). This meets the expectation of a correlation between the absorption and the power law parameters. The normalization of the remnant power law and the AGN/GRXE power law are also correlated (upper middle). This is not surprising since it is hard to disentangle the contribution of two power law like spectra with a similar photon index.

level for N_H in the source region, the normalization of the remnant power law and the scale factor for the instrumental background in the source region (the latter is hardly significant). This indicates again that all parameters of the source emission model are correlated: All of them change significantly when freezing Γ_{SNR} to a value outside the confidence range while the resulting best fit is of almost equal quality as for a thawed photon index.
In order to assess the quality of the fit, contour plots have been produced, like for the background subtracted fit in Sect. 3.2. Fig. 16 shows some examples. Just as for the background subtracted fit, a clear correlation between the source model parameters is visible. In contrast, the photon index Γ_{SNR} is not notably correlated with the FWC scaling factor of the background region model and with the N_H in the background region.
Fig. 17 shows all model components of the best-fitting model for the source region with the photon index frozen to the result of Doroshenko et al. (2017), $\Gamma_{SNR} = 2.66$ (see Table 5 for the parameter values). According to this plot, the source emission (grey curve) dominates over the other components from ~ 1 keV to ~ 3 keV. The instrumental background (purple curve) dominates towards the high and low energy end.

A reasonable representation of the source and background region spectrum with the same model and

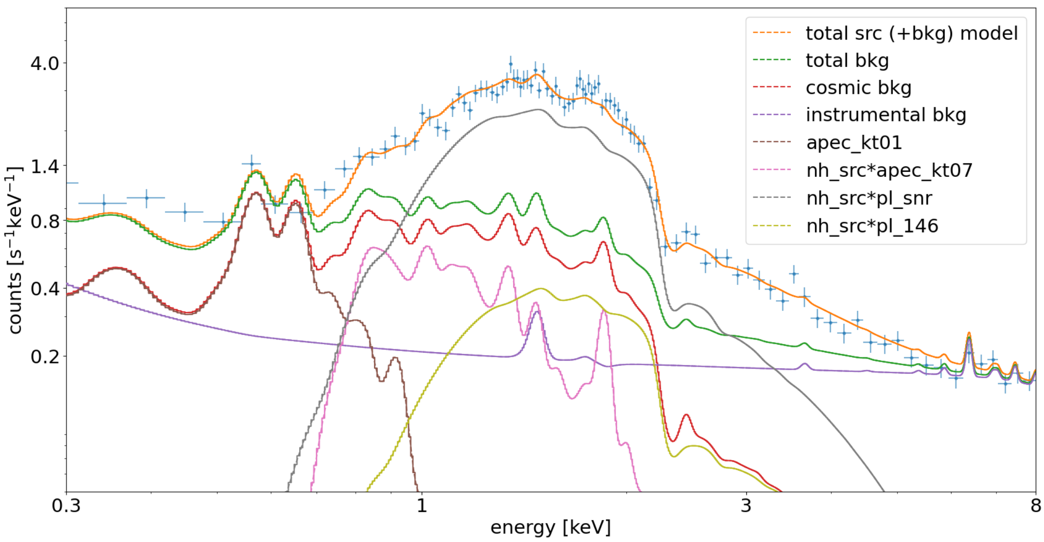

Figure 17: Model components for the best-fitting source model of the simultaneous fit of the source and background region spectrum with the photon index frozen to the result of Doroshenko et al. (2017), $\Gamma_{SNR} = 2.66$ (see red model in Fig. 15, left panel).

parameters has been achieved by introducing two different absorption column densities for the source and background region. The remaining background model parameters were the same for both regions, rescaled by the area ratio for the cosmic components and by the BACKSCAL ratio for the instrumental background.

A remaining caveat of the final source models shown in Fig. 14 is that they underestimate the flux of the spectrum at energies $\lesssim 0.5$ keV. This phenomenon is hardly present when excluding the data of TM 5 and 7 from the fit, as shown in Appendix C and already mentioned in Sect. 3.3.4. Therefore, a major part of the deviation seems to be caused by the higher instrumental background of these two TMs (see Fig. 8) which is not accounted for by the background model since the instrumental background of TM1 is used for the merged data set. Since the FWC models for TM 5 and 7 are only valid above 1 keV, even assigning the appropriate instrumental background model to the data of each TM would not resolve this problem. The only remedy would be to restrict the energy range for the fit accordingly for TM 5 and 7. However, as already mentioned, the differences in the parameters of the source and cosmic X-ray background model when excluding TM 5 and 7 are not significant at the 1σ level (see Appendix C). This allows the conclusion that the fit results are not significantly influenced by the higher instrumental background of TM 5 and 7 for soft energies. Thus, at this point, there is no need to deal with the problem in greater detail. The source region spectrum is dominated by thermal background components in the energy range of the model-data deviation (see Fig. 17). Therefore, the fact that the underestimating model count rate is only present in the source region spectrum and is still slightly visible also in the TM12346 fit could in principle also indicate that there is a faint thermal emission from the remnant. In this case, the X-ray emission detected from it would not be of purely non-thermal nature as it was found in all studies so far. In principle, a thermal component is expected to be there, but it might not be detected e. g. due to absorption. However, on the basis of the analysis conducted in this Master Thesis, it is not possible to give concrete evidence or further indications that thermal emission is indeed seen from the source. For a further investigation of this theory, it would be crucial to precisely consider point source removal within the source region besides the CCO. Since this was not done here, a contribution from point sources (apparently) located within the remnant could be partially responsible for the unaccounted thermal emission from the source region. Apart from that, it is also possible that some components of the cosmic X-ray background differ in their shape between the source and background region and that as a consequence, the background model does not fully account for the background emission in the source region.

Table 5: Best-fitting parameters for the simultaneous fit of the source and background region spectrum. *Left:* Γ_{SNR} is frozen to the result of Doroshenko et al. (2017). Errors correspond to the 1σ confidence bounds. *Right:* Γ_{SNR} is thawed. The corresponding fits are compared in Fig. 15. The last row of the Table lists the reduced statistics value for both fits, indicating that they are of nearly equal quality.

	Γ_{SNR} = 2.66 frozen			Γ_{SNR} thawed		
parameter	value	lower error	upper error	value	lower error	upper error
pl_snr.PhoIndex	2.66	–	–	2.21	-0.09	+0.10
nh_bkg.nH$^{(b)}$	1.34	-0.09	+0.08	1.24	-0.11	+0.09
nh_src.nH$^{(b)}$	1.63	-0.04	+0.04	1.43	-0.08	+0.06
apec_kt01.kT$^{(a)}$	0.23	-0.01	+0.01	0.22	-0.01	+0.01
apec_kt03.kT$^{(a)}$	0.67	-0.04	+0.03	0.65	-0.03	+0.03
pl_snr.norm$^{(c)}$	0.037	-0.001	+0.001	0.026	-0.002	+0.002
pl146.norm$^{(c)}$	0.0027	-0.0002	+0.0002	0.0027	-0.0002	+0.0002
apec_kt01.norm$^{(c)}$	0.00080	-0.00003	+0.00004	0.00078	-0.00003	+0.00003
apec_kt03.norm$^{(c)}$	0.012	-0.002	+0.002	0.010	-0.002	+0.002
scale_bkgreg.factor	0.53	-0.01	+0.01	0.51	-0.01	+0.01
red. stat.	1.01			1.00		

$^{(a)}$in units of keV $^{(b)}$ in units of 10^{22} atoms/cm^2 $^{(c)}$ in units of photons/s/cm^2/keV

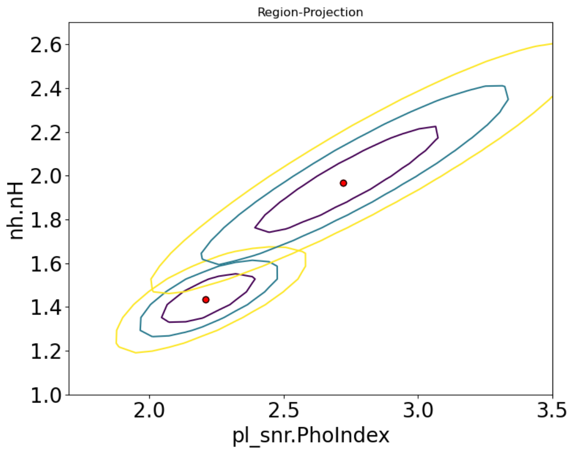

Figure 18: Over-plot of the 1σ, 2σ and 3σ contours of the absorption column density in the source region on the x-axis and the photon index of the remnant power law on the y-axis for the background subtraction (right contours) and background modelling (left contours). The 2σ contours are almost overlapping, the 1σ contours are clearly separated. It is evident that the confidence range for Γ_{SNR} is larger on all levels for the background subtracted fit than for background modelling.

When keeping the photon index free in the simultaneous fit of source and background, it converges to a value for which the result of Doroshenko et al. (2017) as well as that of the background subtracted fit (Sect. 3.2) is outside the 1σ confidence range. However, fixing $\Gamma_{SNR} = 2.66$ results in a fit of equal quality. This indicates that the eROSITA spectrum of HESS J1731-347 is compatible with a photon index of $\Gamma_{SNR} = 2.66$ which is also inside the confidence range of the background subtracted fit result (see Sect. 3.2). On the other hand, fixing $\Gamma_{SNR} = 2.21$ in the background subtracted fit (i. e. using the result obtained for a free Γ_{SNR} in the simultaneous background modelling fit) increases $\chi^2_{\rm red}$ from 0.79 to 0.86. Even the upper confidence bound of $\Gamma_{SNR} = 2.31$ yields $\chi^2_{\rm red} = 0.84$. Thus, the background modelling fit is more compatible with the Γ_{SNR} result of Doroshenko et al. (2017) and therefore with the result of the background subtracted fit than the other way round. Fig. 18 shows an over-plot of the N_H versus Γ_{SNR} contours for background subtraction (right contours) and background modelling (left contours). The 1σ contours are clearly separated, while already the 2σ contours are almost overlapping. This shows that at least within the 95% confidence range of both results, respectively, the two values seem to be compatible.

It might be due to the poor counting statistics and the larger number of free parameters that a result for Γ_{SNR} that is compatible within 1σ with 2.66 is not obtained straight-forward in the background modelling fit. One strong approximation which is used for both the background subtracted and background modelling fit in this Thesis work, in contrast to the work of Doroshenko et al. (2017), is fitting the entire source area with a uniform N_H. This possibly influences the photon index result. Another potential source of inaccuracy might be contaminating thermal emission from point sources within the source region, given that apart from the CCO no point sources were removed from within that area. However, it seems unlikely that point source emission in the remnant region actually has a notable impact on the fit results: When conducting the simultaneous fit of the source and background region for different exclusion radii of the CCO ranging from no exclusion to $100''$, it becomes clear that even including or excluding the CCO from the source region spectrum has no significant effect on the model parameters. The best-fitting models differ slightly, but not considerably, see Fig. 19. So even for the case of what can be expected to be the brightest point source within the remnant region, the contaminating point source radiation does not significantly affect the spectral analysis of the total remnant. In the view of this fact, it seems questionable whether other point sources within the remnant region can be expected to have a considerable effect on the fit result – at least for the total remnant spectrum. For the spectrum of a smaller extraction region around a contaminating source, the influence can be higher. If contamination from point sources within the source region had a notable effect on the spectral fit, this would be expected to affect also the background subtracted fit since point source emission was removed before extracting the background spectrum. Thus, its removal cannot be expected to be included in the background subtraction. The background subtracted fit would be expected to handle the issue worse than the background modelling, given that the contamination can be accounted for by the background model – at least to an extent where it is still compatible with the background region spectrum.
Since for the background subtracted fit, the best-fitting parameters change for the selection of different background regions (see Sect. 3.2), the simultaneous fit was also conducted with the left and right half annulus background spectrum (see Fig. 5 for the definition of the half annuli and the corresponding spectra).The results are given in Appendix D. For the right half annulus, the results of all source model parameters agree with those of the background subtracted fit for the same background region within 1σ confidence bounds. In contrast to that, for the left half annulus, the deviations of the parameters are larger than for the total annulus. The best-fitting photon indices are $\Gamma_{\text{left}} = 2.18^{+0.10}_{-0.09}$ and $\Gamma_{\text{right}} = 2.28^{+0.10}_{-0.15}$. Thus, there seems to be a systematic uncertainty on the order of 0.1 related to the background region selection in the background modelling fit. The agreement with background subtraction for the right half annulus could indicate that the background radiation in the source region is better represented by the spectrum extracted from the right half annulus. This would imply a higher average absorption in the source region than in the left half or total background annulus. Even though the photon indices obtained from background modelling and background subtraction agree for the right half annulus background, the best-fitting remnant photon index for background modelling is significantly lower than the one obtained by Doroshenko et al. (2017) also in this case.

Even though the XMM-Newton observations analysed by Doroshenko et al. (2017) provide much better counting statistics and therefore more reliable results from a statistical point of view than the eRASS:4 data, one has to keep in mind that the stray light contamination is less for eROSITA than for *XMM-Newton* since the telescope is designed for an all-sky survey which requires a particularly good stray light shielding through X-ray baffles (as already mentioned in Sect. 1.3.1). Doroshenko et al. (2017) introduced a power law with an index of ~ 1.5 in the background model to account for the stray light component (together with the GRXE). They state that since it is hard to disentangle the remnant emission from this component, the stray light contribution might be overestimated for some parts of

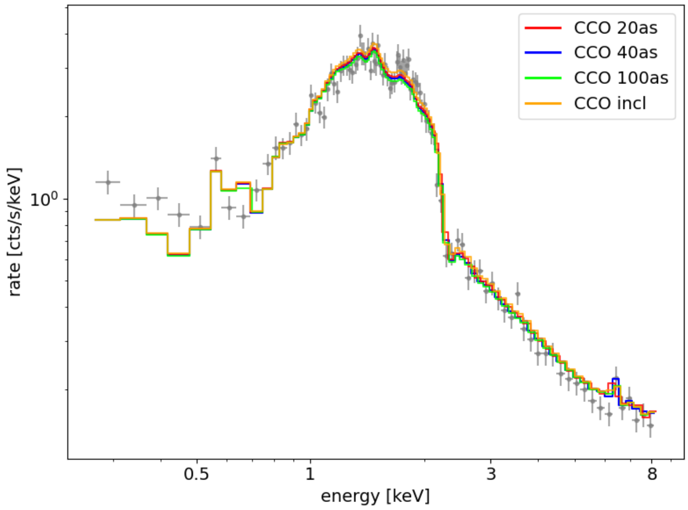

Figure 19: Best-fitting models for the source region spectrum from the simultaneous source and background area fit. Different exclusion radii for the CCO have been tested, ranging from no exclusion at all (orange) to a 100″ radius (green). The free fit parameters are the same as in Table 4, right. There are no significant differences in the best-fitting values. The spectrum plotted in grey is the one for an exclusion radius of 40″ which was used in the analysis.

the remnant in their analysis. It seems possible that this might have affected the result for the photon index of the remnant. They also extracted the spectra of 11 particularly bright circular regions within the remnant, choosing an extraction radius of 50″, see their Fig. 4 top, and performed a background subtracted fit for them. The background was extracted from annular regions with 60″ inner and 80″ outer radius around each source region. For 6 out of the 11 regions, a photon index smaller than 2.3 is within the 1σ confidence range, see their Fig. 4 bottom panel. The average photon index for all 11 regions is slightly below 2.4, thus smaller than the result of 2.66 for the fit of the total remnant divided in sub-regions. Even though this difference is not significant according to the authors, it shows that a photon index harder than 2.66 is not in complete contradiction to the analysis results of Doroshenko et al. (2017).
Bamba et al. (2012) also fitted the spectra from *Suzaku* observations for 13 sub-regions of the SNR. They found photon indices between 1.64 and 3.71, considering the lower and upper 90% confidence bounds of their smallest and largest result, respectively.

4. Spatially resolved spectral analysis

4.1. Method description

Doroshenko et al. (2017) were not able to constrain variations of the power law photon index Γ_{SNR} across the remnant in their *XMM-Newton* study despite the good counting statistics due to stray light issues. For the spatially resolved spectral analysis in this Thesis work, photon index variations were traced by using the approximation of a 2d linear gradient, see Sect. 4.1. The gradient model was also tested for the absorption column density N_H. At the beginning, the photon index was kept constant over the remnant and only variations of N_H were traced (Sect. 4.2.1 and Sect. 4.2.2). N_H variations have already been found by Doroshenko et al. (2017). In the further analysis, the gradient relation for photon index variations was applied (Sect. 4.2.4 and Sect. 4.2.5).
For the spatially resolved spectral analysis, the remnant was divided into sub-regions, as described in the following section.

4.1.1. Region definition and point source removal

For simplicity, the definition of the sub-regions was done much more generic in this Thesis than in the work of Doroshenko et al. (2017). All sub-regions are of equal size and quadratic shape. The grid is defined such that the outermost pixels are background pixels that do not contain any source emission. They frame the source region. Thus, for n by n pixels, the source region, which has a diameter of 35′, is divided into $(n-2)$ by $(n-2)$ sub-regions, framed by one row of background pixels on the top, bottom, left and right, respectively. Pixels are named by their row and column index, starting in the upper left corner with pixel 11 (see Fig. 20). On the one hand, increasing the number of pixels allows a more precise tracing of N_H variations across the remnant. On the other hand, it reduces the size of each single pixel, which leads to lower counting statistics for each spectrum and therefore increases uncertainties and reduces the meaning of the spectral shape for each pixel. The analysis was carried out for a grid of 6 by 6 pixels. For this case, the variations of N_H can be traced and the counting statistics of the sub-regions spectra is still sufficient to perform reasonable fits and not abolish the meaning of a good agreement between model and data. For smaller sub-regions, the shape of the spectra gets more and more blurred until there is only noise left. Since the fit quality is evaluated based on the agreement of all sub-region spectra with their respective model, the fit results become more arbitrary for spectra with only little count rates and correspondingly large uncertainties. For obvious reasons, the spectral shape looses its characteristics sooner for the background regions and dimmer source regions in the western part than for bright pixels containing a large fraction of source emission.

Five of the 36 regions have been excluded from the fit and are crossed out in red in Fig. 20: pixels 11, 12, 51, 61, 62 and 26. The first five of them show a higher background emission in the 0.3-1.8 keV range (color-coded in red) with respect to the other background pixels. They cover the area comprised by the larger background annulus with inner radius 20′ and outer radius 30′ that led to suspicious results in the background subtracted fit (see Appendix B). Pixel 26 was excluded since it contains a bright contaminating source. When removing only a certain area around this source, one cannot be sure that the exclusion radius is sufficient that no significant contribution of the emission is left over. For bright sources, even the signal in the wings of the PSF can contaminate the spectrum. Only a small fraction of the source energy is contained in them, but for a bright source, this can still correspond to a non-negligible absolute value. Also, excluding the contaminating source reduces the area of the pixel and therefore the counting statistics of its spectrum which is expected to be poor anyway since it is a background pixel next to the stronger absorbed right side of the remnant.

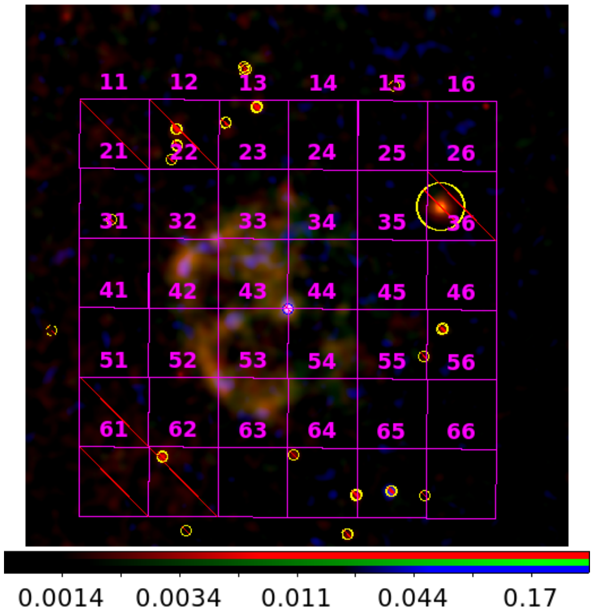

Figure 20: Definition of the sub-regions for the spatially resolved spectral analysis. The regions are named such that the first digit denotes the row and the second the column of each pixel, starting at the upper left with '11'. The regions marked with a red line were excluded from the analysis due to contamination. Point sources are masked out only from the background regions, i. e. from an annulus with inner radius of 17.5′ corresponding to the size of the source region and an outer radius of 37.5′ corresponding to the half diagonal of the 6x6 grid. They are marked by yellow circles. The exclusion radius for contaminating sources has been reduced from 2′ used for the total background annulus to 40″ (see text for further explanations). The circle around the bright source in pixel 26 with more than 100 cts has a radius of 3′, but this region is not included in the analysis.

Just as for the extraction of the total remnant spectrum, the CCO was excluded with a 40″ radius. As mentioned in Sect. 3.1.1, the influence of the remaining $\lesssim$ 5% of the CCO counts is higher in the case of smaller sub-regions than for the total spectrum. On the other hand, the CCO by definition of the regions lies exactly in the middel of regions 33, 34, 43 and 44. Thus, each region contains only one fourth of the total CCO counts (assuming that its radiation is isotropic). The dimmest of the four regions, region 34, has a total of 801 cts. For an exclusion radius of 40″, less than 20 cts are expected to be left from the CCO. This corresponds to a contribution of 5 cts to each region's spectrum. Thus, the count ratio is still ≈0.6%.
The exclusion radius of point sources in the background pixels (i. e.the outermost rows and columns) was chosen to also be 40″, hence smaller than the 2′ used for the total background annulus in Sect. 3.1. However, an energy fraction of >95% is still expected to be included within 40″ (see Sect. 3.1). Since sub-regions with smaller areas are considered here, it becomes important to choose exclusion radii which are not larger than necessary. Otherwise, a considerable fraction of the pixel area is unnecessarily excluded from the analysis. All point sources in background regions considered in the analysis have less than 100 cts in the eRASS catalogs, thus they were all excluded with the same 40″ radius.

4.1.2. Model definition

Since, as mentioned before, the counting statistics of the eROSITA observations available for the remnant are low, a linking relation for the the absorption values and the photon index values between different regions was introduced. This relation was assumed to be a linear gradient in both x (i. e. east-west) and y (i. e. north-south) direction. As the reference point for N_H, pixel 14 was selected since it does not comprise any contaminating point sources. Thus, with *slope_x* and *slope_y* being the parameters describing the gradient relation, the N_H value of the pixel ij in row i, column j can be calculated as

$$N_{H,ij} = N_{H,14} + \text{slope\_x} \cdot (j-4) + \text{slope\_y} \cdot (i-1) \tag{7}$$

The origin of the coordinate system is in the top left corner, *slope_x* denotes the change in N_H when moving one pixel to the right (i. e. to the west of the remnant) and *slope_y* when moving one pixel to the bottom (i. e.towards the south of the SNR). The parameters *slope_x* and *slope_y* were added to the spectral model, multiplied by 0. This is necessary in order to achieve that they are varied during the fit with sherpa.[47] Since they are added with an amplitude of 0, they have no impact on the count rate of the best-fitting spectral model. An analogous gradient relation was also introduced to trace variations of the photon index Γ_{SNR} in a later step, in this case with reference region 22. When applying the linking relation to both the N_H and Γ_{SNR} values, the number of free fit parameters needed to represent absorption and photon index variations is reduced from 46 to 6.[48]

Since the counting statistics are much better for the total source and background spectrum than for the sub-regions and additional free parameters have to be introduced in the spatially resolved fit to model the N_H and Γ_{SNR} variations, the parameters of the cosmic X-ray background model were fixed to the results in Table 5 for the case of $\Gamma_{SNR} = 2.66$ frozen. Γ_{SNR} was also frozen to 2.66 for the spatially resolved fit. This is reasonable since the counting statistics of the XMM study is much better than that of eRASS1 to 4. Additionally, XMM Newton is sensitive in a wider energy range than eROSITA which allows a more reliable constraining of the photon index in spectral analyses. Also, the background subtracted fit of the eROSITA spectrum (see Sect. 3.2) yielded a result which is in agreement with the XMM result of Doroshenko et al. (2017) and the simultaneous fit of the source and background region is not considerably worse when freezing $\Gamma_{SNR} = 2.66$ (see Fig. 15). In order to check whether the choice of the photon index value affects the resulting N_H gradient slopes, the fit was re-done with $\Gamma_{SNR} = 2.12$, i. e. frozen to the lower 1σ bound of the simultaneous source and background region fit. This check revealed that the N_H gradient is not significantly affected by the photon index value (see Sect. 4.2.1).

The cosmic X-ray background model for each pixel was scaled by a constant factor corresponding to the area of the pixel divided by the area of the total background annulus.[49] For the instrumental background, the scaling factor corresponds to the BACKSCAL of the pixel, divided by the BACKSCAL of the background annulus. The normalization of the remnant power law was left free since not all pixels cover an equal fraction of the source, thus the normalizations cannot be assumed to be equal. For the edge pixels that do not contain any source emission, the normalization of the source power law was set to 0.

The fit was carried out using the *levmar* optimization method since the *neldermead* method did not lead to reasonable results. The reduced statistics value was larger for the *neldermead* option (1.44 vs. 0.86 for *levmar* in the case of N_H linked and Γ_{SNR} frozen) which indicates that the fit with *neldermead* did not converge to the global minimum.

The assumption that the absorption and the photon index change according to the 2d linear gradient relation introduced above is an approximation. An interesting question is, of course, how well the gradient model reflects the 'real' behaviour of the two parameters across the observed region. Due to the poor counting statistics, this cannot be fully answered from the eRASS:4 data, which is the reason why the linking relations have been introduced in the first place. However, at least for the absorption column density, physically meaningful results can be obtained also from fits without gradient linking (see Sect. 4.2.2 and 4.2.5) and can be compared to the gradient model. In the following sections, the fit results for different models with various combinations of photon index and absorption column density relations between the sub-regions are discussed and compared to each other.

[47] `https://cxc.cfa.harvard.edu/sherpa/ahelp/link.html`, accessed 2022-1012

[48] For the independent case: 30 absorption plus 16 photon index values. For the linked case: one reference absorption value plus a slope in south-west direction plus a slope in north-south direction and the same for the photon index.

[49] Areas were read out from the REGAREA keyword in the fits header.

4.2. Results

4.2.1. Fit with linked N_H and constant, frozen Γ_{SNR}

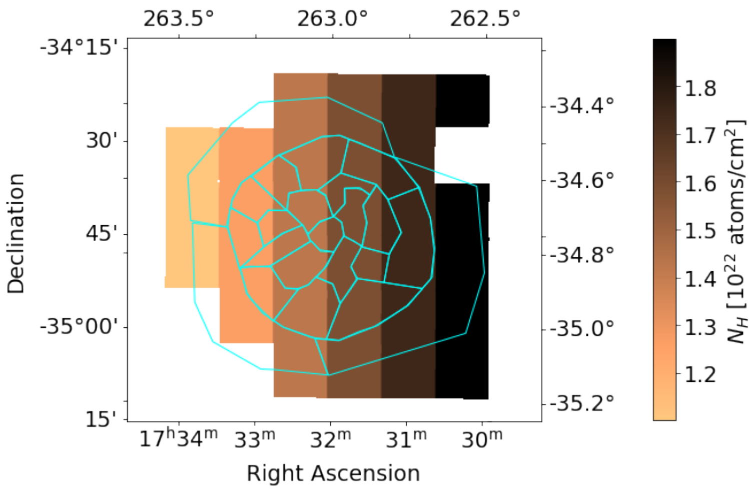

Figure 21: Color map visualization of the N_H gradient across the SNR with frozen photon index. The absorption for each of the 30 sub-regions included in the analysis is color-coded. Except for region 14, the values have been calculated from the gradient relation defined in Eq. 7. The sub-regions defined by Doroshenko et al. (2017) are overlayed in blue.

In order to verify that the spectra of all sub-regions cannot be represented reasonably by a model with constant N_H, the models for some selected regions for a constant N_H and the N_H gradient relation are compared in Appendix E. The outcome of this comparison is that a model with constant N_H clearly underestimates the count rate of background spectra next to the eastern part of the remnant which are less absorbed than the average. On the other hand, count rates of spectra next to the stronger absorbed western part are overestimated. Therefore, it is necessary to allow N_H variations across the SNR, even though the reduced statistics value only decreases from 0.87 for a constant N_H to 0.85 for the gradient relation, see Table 6. The table lists the N_H values in all sub-regions, linked according to Eq. 7. Note that except for the reference region 14, all N_H values were calculated according to the gradient relation and were not introduced as free parameters in the spectral fit. The gradient relation is visualized in a color map in Fig. 21. The absorption changes only when moving in the east-west direction, i. e. perpendicular to the galactic plane. The variations are quantified by the gradient slope resulting from the spectral fit: *slope_nh_x*= $(0.16 \pm 0.01) \cdot 10^{22}$ atoms/cm^2 per pixel. The distance from the center of one pixel to the next is $8.75' \approx 0.15°$. The slope in the east-west direction is significant at more than 3σ. The total change over the 6 columns in east-west direction is $\sim 0.8 \cdot 10^{22}$ atoms/cm^2. In contrast, there is no significant slope in the north-south direction: *slope_nh_y*= $(-0.00 \pm 0.01) \cdot 10^{22}$ atoms/cm^2 per pixel. N_H is increasing towards the western part of the remnant which is closer to the galactic plane. This result is in good agreement with the N_H pattern that Doroshenko et al. (2017) found for the fit of their 18 source plus 3 background regions, see their Fig. 2 right panel and their Table 2. Also, H. E. S. S. Collaboration et al. (2011) derived a ^{12}CO absorption map for the area of the remnant and its surroundings, which is displayed in Fig. 22 (left panel). It shows an increasing integrated brightness temperature of ^{12}CO emission towards the western part of the remnant. This indicates the presence of a molecular cloud in this area since CO line emission is a tracer for molecular clouds. The

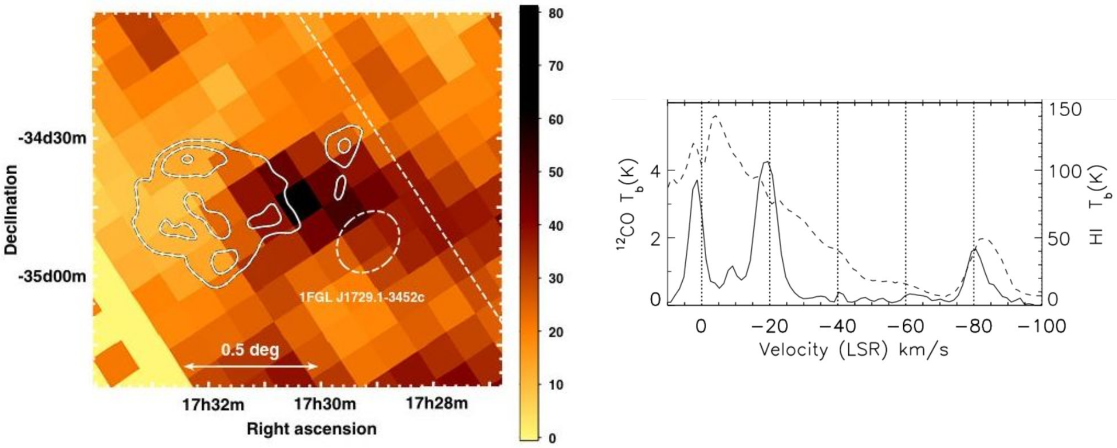

Figure 22: Two figures from H. E. S. S. Collaboration et al. (2011) that indicate the presence of a molecular cloud in front of the western part of HESS J1731-347. *Left panel:* ^{12}CO absorption map derived from data of the CfA survey (Dame et al., 2001), see Fig. 9 top panel of H. E. S. S. Collaboration et al. (2011). The SNR HESS J1731-347 is represented by the contours on the left. The map shows the brightness temperature of the ^{12}CO emission integrated over radial velocities from -13 km/s to -25 km/s in units of K km s^{-1}. *Right panel*: ^{12}CO (solid line) brightness temperature as a function of radial velocity towards the western part of the remnant, see H. E. S. S. Collaboration et al. (2011) Fig. 8 bottom panel. There is a peak of ^{12}CO emission at -18 km/s, indicating the presence of a molecular cloud. According to H. E. S. S. Collaboration et al. (2011), this radial velocity corresponds to a distance of 3.2 kpc using the galaxy rotation model of Hou et al. (2009).

distance of the cloud can be estimated through the Doppler shift observed in the CO emission line. The Doppler shift results from the fact that our galaxy is rotating differentially and not as a rigid body. Consequently, the angular velocity of each object depends on its distance to the galactic center, which leads to a radial movement of molecular clouds with respect to us as observer and thus Doppler-shifted spectra. The presence of a peak in the ^{12}CO brightness temperature towards the western part of the remnant (see Fig. 22 right panel) is an indication that the increasing X-ray absorption in this area is actually caused by a molecular cloud and not by a uniformly distributed denser ISM. Since the peak in ^{12}CO emission occurs at a radial velocity of -18 km/s, H. E. S. S. Collaboration et al. (2011) consider the corresponding distance of 3.2 kpc a lower limit for the distance of the remnant, which is suspected to be located at least partially behind or inside the cloud. An interesting question is in this context whether teh SNR HESS J1731-347 interacts with the molecular cloud in any way or whether it is detached from it. This cannot be answered by looking at the absorption variations. However, observing a change in the photon index might be revealing since an interaction is expected to influence the radiation production of the SNR which would manifest in the spectra of the corresponding areas. Therefore, variations of Γ_{SNR} are traced in Sect. 4.2.4. For now, as mentioned above, the photon index was frozen to the best-fitting result of Doroshenko et al. (2017) ($\Gamma_{SNR} = 2.66 \pm 0.01$) for the N_H gradient fit. Since the background modeling fit of this Thesis work seems to be compatible with this value, but nevertheless yielded a different result ($\Gamma_{SNR} = 2.21^{+0.10}_{-0.09}$, see Sect. 3.3), the N_H gradient fit was also conducted with the photon index frozen to the lower 1σ confidence bound of this result, $\Gamma_{SNR} = 2.12$. The difference in the N_H result for the reference pixel 14 is not significant at the 1σ level: $N_{H,14} = 1.53 \pm 0.03$ for $\Gamma_{SNR} = 2.12$ frozen versus $N_{H,14} = 1.58 \pm 0.04$ with $\Gamma_{SNR} = 2.66$ frozen. N_H is slightly, albeit not significantly, higher for a larger photon index, which reflects the correlation of the two parameters. The change of the absorption from one region to the next, represented by the gradient slopes, is not affected by the choice of the photon index value. The slope results for $\Gamma_{SNR} = 2.12$ are *slope_nh_y*= -0.01 ± 0.01 and *slope_nh_x*= 0.16 ± 0.01. The reduced statistics value is 0.84 and therefore almost equal to the case for $\Gamma_{SNR} = 2.66$ (red. stat.=0.86, see Table 6).

As a conclusion, the obtained N_H gradient is not sensitive to varying the photon index between ~ 2.1 and ~ 2.7. When leaving Γ_{SNR} as a free fit parameter, but constant over all regions, the result is slightly lower than that of the simultaneous fit of the total remnant and background annulus spectrum: $\Gamma_{SNR} = 2.06 \pm 0.06$. The reduced statistics value in this case is 0.84.

Table 6: Best-fitting parameters for the N_H gradient fit with $\Gamma_{SNR} = 2.66$ frozen. The N_H values for all regions except the reference pixel 14 are calculated from the gradient relation according to Eq. 7. Errors are obtained from statistical error propagation:
$\Delta N_{H,ij} = \sqrt{(\Delta N_{H,14})^2 + (\Delta \text{slope\_x} \cdot (j-4))^2 + (\Delta \text{slope\_y} \cdot (i-1))^2}$. For the other parameters, the 1σ confidence bounds are given as uncertainties. The indexing of the N_H parameters corresponds to the region names as defined in Fig. 20. Absorptions are given in units of 10^{22} atoms/cm^2, power law normalizations in units of photons/cm^2/s. The gradient slopes are defined as change per pixel, i. e. over a distance of 8.75′.

par	val	lower error	upper error	par	val	lower error	upper error
nh14.nH	1.58	-0.04	+0.04	nh53.nH	1.41	0.06	0.06
slope_nh_y.factor	0.00	-0.01	0.01	nh54.nH	1.56	0.06	0.06
slope_nh_x.factor	0.16	-0.01	0.01	nh55.nH	1.72	0.06	0.06
nh13.nH	1.42	0.04	0.04	nh56.nH	1.87	0.07	0.07
nh15.nH	1.73	0.04	0.04	nh63.nH	1.40	0.07	0.07
nh16.nH	1.89	0.04	0.05	nh64.nH	1.56	0.07	0.07
nh21.nH	1.10	0.05	0.05	nh65.nH	1.71	0.07	0.07
nh22.nH	1.26	0.05	0.05	nh66.nH	1.87	0.08	0.08
nh23.nH	1.42	0.04	0.04	pl_snr22.norm	0.0008	-0.0001	0.0001
nh24.nH	1.57	0.04	0.04	pl_snr23.norm	0.0031	-0.0002	0.0002
nh25.nH	1.73	0.04	0.04	pl_snr24.norm	0.0014	-0.0001	0.0001
nh31.nH	1.10	0.06	0.06	pl_snr25.norm	0.0002	-0.0001	0.0001
nh32.nH	1.26	0.05	0.05	pl_snr32.norm	0.0039	-0.0002	0.0002
nh33.nH	1.41	0.05	0.05	pl_snr33.norm	0.0054	-0.0002	0.0002
nh34.nH	1.57	0.04	0.05	pl_snr34.norm	0.0017	-0.0001	0.0001
nh35.nH	1.72	0.05	0.05	pl_snr35.norm	0.0004	-0.0001	0.0001
nh36.nH	1.88	0.05	0.05	pl_snr42.norm	0.0025	-0.0001	0.0001
nh41.nH	1.10	0.06	0.06	pl_snr43.norm	0.0033	-0.0002	0.0002
nh42.nH	1.25	0.06	0.06	pl_snr44.norm	0.0022	-0.0002	0.0002
nh43.nH	1.41	0.05	0.05	pl_snr45.norm	0.0011	-0.0001	0.0001
nh44.nH	1.56	0.05	0.05	pl_snr52.norm	0.0006	-0.0001	0.0001
nh45.nH	1.72	0.05	0.05	pl_snr53.norm	0.0036	-0.0002	0.0002
nh46.nH	1.88	0.06	0.06	pl_snr54.norm	0.0013	-0.0001	0.0001
nh52.nH	1.25	0.07	0.07	pl_snr55.norm	0.0001	-0.0001	0.0001
red. stat.	0.86						

Spectral analyses of the CCO candidate XMMUJ173203.3-344518 inside HESS J1731-347 offer a possibility to constrain the absorption column density towards the center of the remnant. Values range from $N_H \approx 1.5 \cdot 10^{22}$ atoms/cm^2 (e. g. Acero et al. 2009, Bamba et al. 2012) to $N_H \approx 2 \cdot 10^{22}$ atoms/cm^2 (Klochkov et al. 2013, Klochkov et al. 2015, Landstorfer et al. 2022). Since the CCO lies exactly in the middle between regions 33, 34, 43 and 44 (see Fig. 20), the preconditions for comparing the N_H values of the spatially resolved spectral analysis performed in this Thesis to the values obtained from CCO spectral fitting are not ideal. The results for the four regions range between $N_{H,33} = N_{H,43} = (1.41 \pm 0.05) \cdot 10^{22}$ atoms/cm^2 and $N_{H,34} = 1.57^{+0.05}_{-0.04} \cdot 10^{22}$ atoms/cm^2. Therefore, they agree well with the results of Acero et al. (2009) and Bamba et al. (2012) and are a bit lower

than the value obtained by Klochkov et al. (2013, 2015) and Landstorfer et al. (2022). Klochkov et al. (2013, 2015) assume the neutron star to have a Carbon atmosphere since the spectral fit for a simple black body model is not compatible with the distance of the remnant, see Sect. 1.2.4. Therefore, their approach is systematically different from that of the other studies cited. Thus, if their assumption is true, their result is expected to better reflect the true absorption towards the CCO. Bamba et al. (2012) found a range of $0.82 \leq N_H/(10^{22}\,\text{atoms/cm}^2) \leq 3.18$ in their spectral analysis of 13 sub-regions of the remnant, covered by *Suzaku* observations, referring to the lower 90% confidence bound of their minimum and higher bound of their maximum column density found, see their Table 2. Doroshenko et al. (2017) found values of $1.01 \leq N_H/(10^{22}\,\text{atoms/cm}^2) \leq 2.04$ for their 18 source regions from *XMM-Newton* spectral data, in this case referring to the 1σ confidence bounds of the smallest and largest result. The N_H values displayed in Table 6 and Fig. 21 are in good agreement with these ranges spanned by literature results.
In Appendix F, the spectra and best-fitting models of all sub-regions are shown and compared to the models for and independently varying N_H with constant Γ_{SNR} (see next section) and for both N_H and Γ_{SNR} linked by a gradient relation (see Sect. 4.2.4).

4.2.2. Fit with independent N_H and constant, frozen Γ_{SNR}

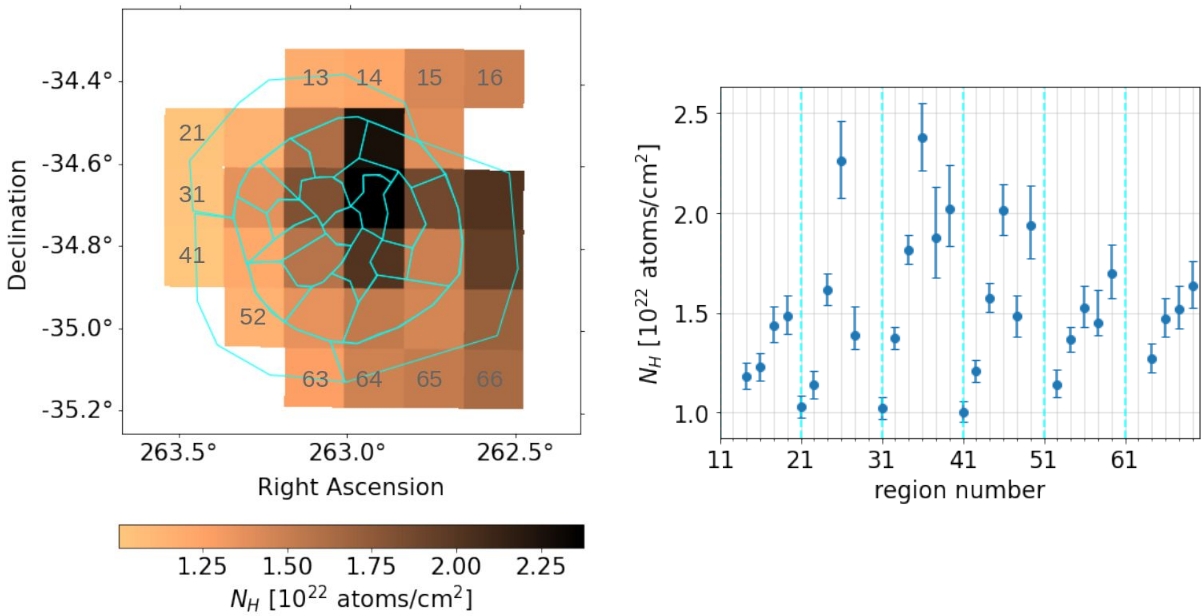

Figure 23: Independent, best-fitting N_H values for all 30 sub-regions included in the fit with $\Gamma_{SNR} = 2.66$ frozen, see Table 7. *Left panel:* Color map visualization. In order to clarify the relation between the left and right plot, some of the region names are over-plotted in grey. The regions defined by Doroshenko et al. (2017) are displayed in cyan in order to indicate the location of the remnant. *Right panel:* Different representation including 1σ uncertainties. The region numbers are the same as in Fig. 20 and indicated in the left panel, starting with '11' in the upper left corner and ending with '66' in the lower right. The vertical, cyan dashed lines indicate the start of a new pixel row.

Fig. 23 visualizes the N_H results for all sub-regions included in the fit when N_H is fitted independently, i. e. without the gradient linking introduced in Eq. 7. The left panel shows a color-map, just as given in Fig. 21 for the N_H gradient fit. A comparison of the two patterns reveals that the variations of N_H across the remnant seem to be more complex than it can be reflected by a simple linear, 2-dimensional gradient. However, from a statistical point of view, the model with independent N_H values is not clearly preferable since the reduced statistics value only decreases marginally from 0.86 to 0.84 with

Table 7: Best-fitting parameters for the fit of the 30 sub-regions considered in the analysis (see Fig. 20) with independent N_H values and a frozen photon index of 2.66 across the remnant. Absorptions are given in units of 10^{22} atoms/cm^2, power law normalizations in units of photons/cm^2/s.'nan' entries mean that the confidence bounds could not be determined (often the case for parameter results close to the allowed minimum or maximum).

par	val	lower error	upper error	par	val	lower error	upper error
nh13.nH	1.18	-0.06	+0.07	nh54.nH	1.53	-0.10	+0.11
nh14.nH	1.23	-0.07	+0.07	nh55.nH	1.45	-0.07	+0.16
nh15.nH	1.44	-0.09	+0.10	nh56.nH	1.70	-0.12	+0.14
nh16.nH	1.48	-0.09	+0.10	nh63.nH	1.27	-0.07	+0.08
nh21.nH	1.03	-0.05	+0.06	nh64.nH	1.47	-0.09	+0.10
nh22.nH	1.14	-0.07	+0.07	nh65.nH	1.52	-0.10	+0.12
nh23.nH	1.61	-0.08	+0.08	nh66.nH	1.64	-0.11	+0.13
nh24.nH	2.26	-0.18	+0.20	pl_snr22.norm	0.0006	-0.0001	+0.0001
nh25.nH	1.39	-0.07	+0.14	pl_snr23.norm	0.0036	-0.0003	+0.0003
nh31.nH	1.02	-0.05	+0.05	pl_snr24.norm	0.0025	-0.0004	+0.0004
nh32.nH	1.37	-0.06	+0.06	pl_snr25.norm	0.0000	nan	+0.0001
nh33.nH	1.81	-0.07	+0.07	pl_snr32.norm	0.0043	-0.0003	+0.0003
nh34.nH	2.37	-0.16	+0.17	pl_snr33.norm	0.0073	-0.0004	+0.0005
nh35.nH	1.88	-0.20	+0.26	pl_snr34.norm	0.0033	-0.0004	+0.0004
nh36.nH	2.02	-0.18	+0.22	pl_snr35.norm	0.0005	-0.0002	+0.0002
nh41.nH	1.00	-0.05	+0.05	pl_snr42.norm	0.0024	-0.0002	+0.0002
nh42.nH	1.21	-0.06	+0.06	pl_snr43.norm	0.0039	-0.0003	+0.0003
nh43.nH	1.58	-0.07	+0.08	pl_snr44.norm	0.0032	-0.0003	+0.0004
nh44.nH	2.01	-0.12	+0.13	pl_snr45.norm	0.0009	-0.0002	+0.0002
nh45.nH	1.48	-0.10	+0.11	pl_snr52.norm	0.0005	-0.0001	+0.0001
nh46.nH	1.94	-0.16	+0.20	pl_snr53.norm	0.0035	-0.0003	+0.0003
nh52.nH	1.14	-0.07	+0.07	pl_snr54.norm	0.0013	-0.0002	+0.0002
nh53.nH	1.37	-0.06	+0.06	pl_snr55.norm	0.0000	nan	+0.0001
red. stat.	0.84						

respect to the N_H gradient model. The purpose of the gradient fitting was to approximately trace the direction in which N_H is increasing or decreasing, using a model with the lowest possible number of free parameters.

The right panel of Fig. 23 shows the independent N_H results including 1σ uncertainties as a function of the pixel number (see Fig. 20). The vertical cyan lines indicate the start of a new pixel row. Even though the N_H variations in the color map differ from the 2-d gradient pattern, there is a tendency of increasing absorption from left to right within each pixel row, i. e. when moving towards the western of the remnant. Just as for the values obtained from the N_H gradient fit, see Sect. 4.2.1, the range of the independent N_H values in Table 7 and Fig. 23 is well within the boundaries of what Bamba et al. (2012) found for their 13 sub-regions covered by *Suzaku* pointings and also in reaosnable agreement with the result of the *XMM-Newton* analysis of Doroshenko et al. (2017). The N_H range for the 4 regions covering the CCO includes higher values for the independent fit than for the gradient fit in Sect. 4.2.1: The lowest value is $N_{H,43} = 1.58 \cdot 10^{22}$ atoms/cm^2, the highest $N_{H,34} = 2.37 \cdot 10^{22}$ atoms/cm^2. Considering the absorption column densities obtained from spectral analyses of the CCO (Acero et al. 2009, Bamba et al. 2012, Klochkov et al. 2013, Klochkov et al. 2015, Landstorfer et al. 2022, see Sect. 4.2.1 for the numbers), the results of the independent N_H fit tend to agree better with the result of Klochkov et al. (2013, 2015) and Landstorfer et al. (2022) than with that of the other two studies. Klochkov et al. (2013) were the first ones to assume that the CCO

is covered by a carbon atmosphere. If this is indeed the case, their N_H result is expected to be more correct than that of the other studies and the better agreement with this result speaks in favour of the independent N_H results. Also, the fits of the spectra extracted from regions 24 and 34 are considerably better for an independent N_H than for the gradient relation, see Fig. F1. However, as mentioned at the beginning of the section, the reduced statistics value barely improves with respect to the N_H gradient fit. Thus, the introduction of 27 additional free parameters (29 free N_H values in addition to that of the reference pixel minus 2 for the gradient slopes) is not justified from a statistical point of view, given the low counting statistics.
In order to check how well the 2-d gradient model agrees with the independent N_H values, the deviations between both data sets were evaluated in the following Sect. 4.2.3.

4.2.3. Deviations between linked and independent N_H values for frozen Γ_{SNR}

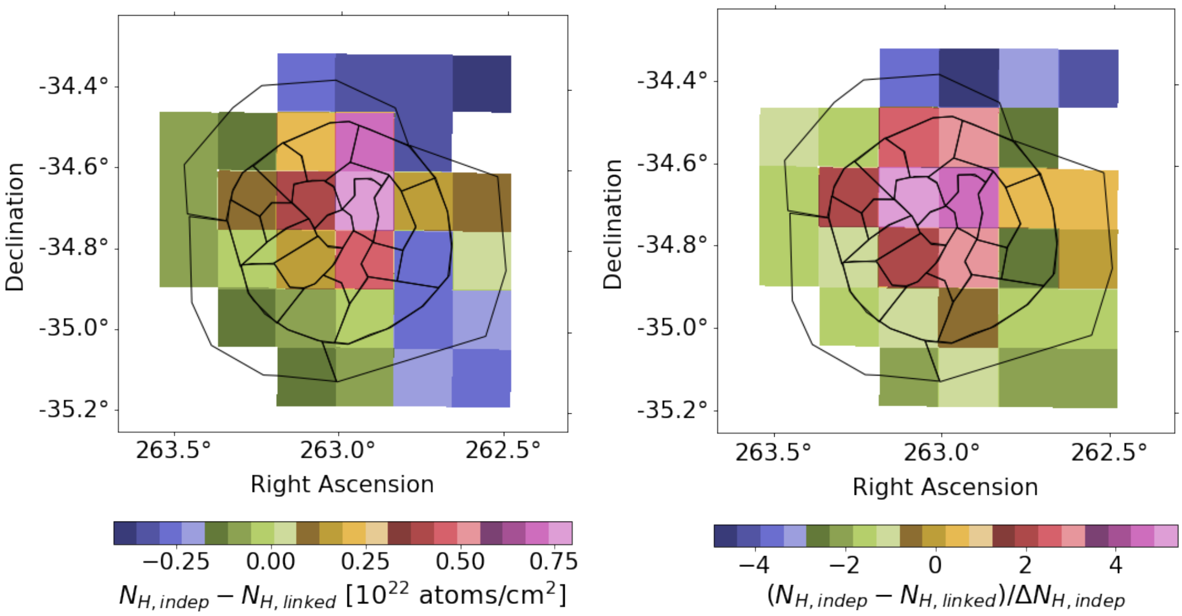

Figure 24: *Left panel:* Residuals of the independent N_H values obtained in Sect. 4.2.2 w. r. t. the gradient relation found in Sect. 4.2.1 (i. e. data-model). *Right panel:* Residuals weighted by the errors of the independent N_H values.

In order to evaluate how well the independent N_H values obtained from the fit in Sect. 4.2.2 are represented by the gradient relation found in Sect. 4.2.1, the residuals and weighted residuals between both data sets are visualized in Fig. 24. Fig. 25 shows the N_H values as a function of the region number, including uncertainties to give an overview on the significance of the deviations. The N_H values calculated from the gradient relation are systematically lower in those areas with the highest independent N_H values. The residuals map resembles the map of the independent N_H values (see Fig. 23 left). The weighted residuals extend quite symmetrically up to roughly $\pm 4.5\sigma$. An interesting question arising from this comparison is: Why was it possible to get reasonable fits for the spectra of all sub-regions with the N_H gradient relations as well as with independent N_H values, even if the N_H pattern is clearly different in these two cases? From looking at Fig. F1, there are only few regions where the model with independent N_H clearly fits the data better, namely regions 24, 34 and 44, which also show the largest residuals in Fig. 24 left. Why is the overall fit quality achieved with the two models equal and why is there almost no difference visible for many other regions? The reason is a problem already mentioned before: the correlation between model parameters. Fig. 26 shows the difference in the normalization of the remnant power law when fitting the spectra of all sub-regions simultaneously with N_H linked by a gradient and with independent N_H values. The norm difference

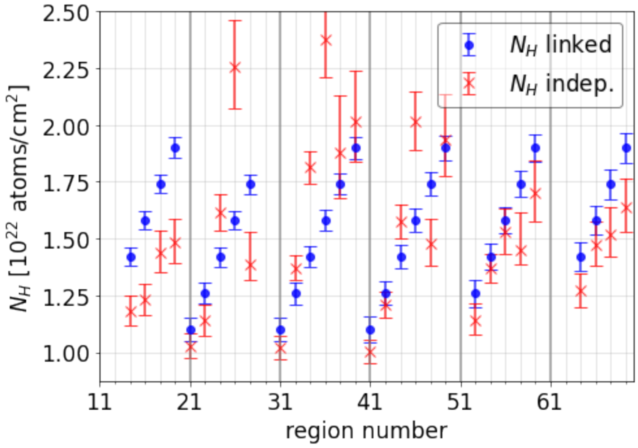

Figure 25: Plot of N_H values as a function of the region number, including uncertainties to assess the significance of the differences. *Blue:* N_H linked (see Sect. 4.2.2). *Red:* N_H independent (Sect. 4.2.2). The thicker grey vertical lines indicate the start of a new pixel row.

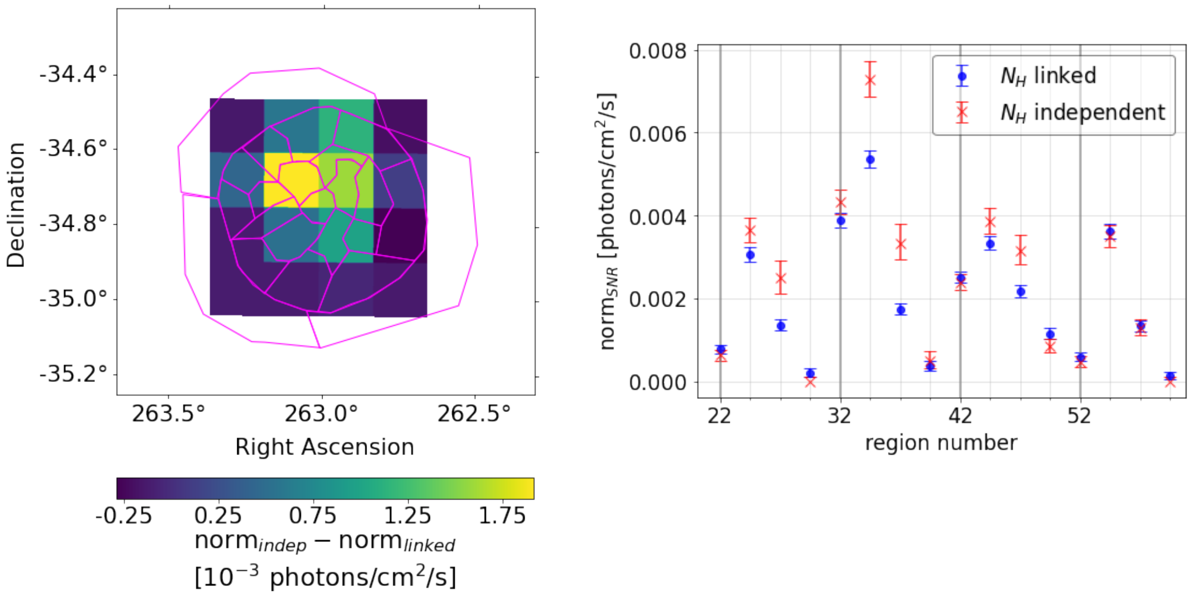

Figure 26: Differences in the normalization of the remnant power law between linked and independent N_H for the source regions, i. e. the inner 4 by 4 pixels in the images in Fig. 24. *Left panel:* Color map visualization for better comparability to Fig. 24. *Right panel:* Plot of normalizations versus region numbers including uncertainties to assess the significance of differences. As in Fig. 25, thick grey lines indicate the start of a new pixel row.

seems to be correlated with the (unweighted) residuals between the N_H values (see Fig. 24 left). Thus, an equally good fit is achieved for the lower absorptions in the N_H linked model in combination with a lower norm of the remnant emission power law. This shows the limits in tracing N_H and Γ variations, which would be less restrictive for improved counting statistics.

4.2.4. Fit with linked N_H and linked Γ_{SNR}

As already mentioned in Sect. 4.2.2, the aim of linking the N_H values by a 2-dimensional gradient is to trace the variations of the absorption along the horizontal and vertical direction across the remnant and reduce the number of free parameters with respect to the independent N_H fit. In this section, the photon index is no longer kept constant across the remnant, but values for different regions are also

Table 8: Best-fitting parameters for the simultaneous fit of the spectra of the 30 sub-regions shown in Fig. 20 with both N_H and Γ linked by a 2-d gradient relation each between individual regions. The N_H and Γ values for all regions except the reference regions were calculated according to Eq. 7 and Eq. 8, respectively. An error propagation for statistical errors was conducted, see caption of Table 6 for details. Absorptions are given in units of 10^{22} atoms/cm^2, power law normalizations in units of photons/cm^2/s. The gradient slopes are defined as change per pixel, i. e. over a distance of 8.75′. 'nan' entries mean that the confidence bounds could not be determined (often the case for parameter results close to the allowed minimum or maximum).

par	val	lower error	upper error	par	val	lower error	upper error
nh14.nH	1.43	-0.03	+0.03	pl_snr52.PhoIndex	2.83	-0.31	+0.31
pl_snr22.PhoIndex	2.15	-0.12	+0.12	pl_snr53.PhoIndex	2.44	-0.28	+0.28
slope_g_y.factor	0.23	-0.06	+0.06	pl_snr54.PhoIndex	2.05	-0.27	+0.27
slope_g_x.factor	-0.39	-0.07	+0.07	pl_snr55.PhoIndex	1.66	-0.28	+0.28
slope_nh_y.factor	0.01	-0.01	+0.01	nh13.nH	1.29	0.04	0.04
slope_nh_x.factor	0.13	-0.01	+0.01	nh15.nH	1.56	-0.04	+0.04
pl_snr22.norm	0.0005	-0.0001	+0.0001	nh16.nH	1.70	-0.04	+0.04
pl_snr23.norm	0.0018	-0.0001	+0.0002	nh21.nH	1.04	-0.05	+0.05
pl_snr24.norm	0.0006	-0.0001	+0.0001	nh22.nH	1.17	-0.04	+0.04
pl_snr25.norm	0.00004	-0.00003	+0.00004	nh23.nH	1.31	-0.04	+0.04
pl_snr32.norm	0.0032	-0.0002	+0.0002	nh24.nH	1.44	-0.04	+0.04
pl_snr33.norm	0.0036	-0.0002	+0.0002	nh25.nH	1.57	-0.04	+0.04
pl_snr34.norm	0.0009	-0.0001	+0.0001	nh31.nH	1.05	-0.05	+0.05
pl_snr35.norm	0.00015	-0.00004	+0.00005	nh32.nH	1.19	-0.05	+0.05
pl_snr42.norm	0.0023	-0.0002	+0.0002	nh33.nH	1.32	-0.04	+0.04
pl_snr43.norm	0.0025	-0.0002	+0.0002	nh34.nH	1.45	-0.04	+0.04
pl_snr44.norm	0.0013	-0.0001	+0.0001	nh35.nH	1.59	-0.04	+0.04
pl_snr45.norm	0.0005	-0.0001	+0.0001	nh36.nH	1.72	-0.05	+0.05
pl_snr52.norm	0.0006	-0.0001	+0.0001	nh41.nH	1.07	-0.06	+0.06
pl_snr53.norm	0.0031	-0.0002	+0.0003	nh42.nH	1.20	-0.05	+0.05
pl_snr54.norm	0.0009	-0.0001	+0.0001	nh43.nH	1.33	-0.05	+0.05
pl_snr55.norm	0.00004	nan	+0.00006	nh44.nH	1.47	-0.05	+0.05
pl_snr23.PhoIndex	1.76	-0.15	+0.15	nh45.nH	1.60	-0.05	+0.05
pl_snr24.PhoIndex	1.37	-0.13	+0.13	nh46.nH	1.73	-0.05	+0.05
pl_snr25.PhoIndex	0.98	-0.15	+0.15	nh52.nH	1.21	-0.06	+0.06
pl_snr32.PhoIndex	2.38	-0.22	+0.23	nh53.nH	1.35	-0.06	+0.06
pl_snr33.PhoIndex	1.99	-0.18	+0.19	nh54.nH	1.48	-0.06	+0.06
pl_snr34.PhoIndex	1.60	-0.17	+0.17	nh55.nH	1.61	-0.06	+0.06
pl_snr35.PhoIndex	1.21	-0.18	+0.19	nh56.nH	1.75	-0.06	+0.06
pl_snr42.PhoIndex	2.60	-0.26	+0.26	nh63.nH	1.36	-0.07	+0.07
pl_snr43.PhoIndex	2.22	-0.23	+0.23	nh64.nH	1.49	-0.07	+0.07
pl_snr44.PhoIndex	1.83	-0.21	+0.22	nh65.nH	1.63	-0.07	+0.07
pl_snr45.PhoIndex	1.44	-0.23	+0.23	nh66.nH	1.76	-0.07	+0.07
red. stat.	0.84						

linked by a 2d linear gradient. The goal is to compare the directions of the N_H and Γ_{SNR} gradient. From this, one can investigate a connection between the hardness of the spectrum and the density of the surroundings, which can be an indication for eventual interactions with a nearby molecular cloud. This involves the assumption that the higher absorption is caused by a matter accumulation in the immediate vicinity of the remnant and not somewhere else between the source and the observer.

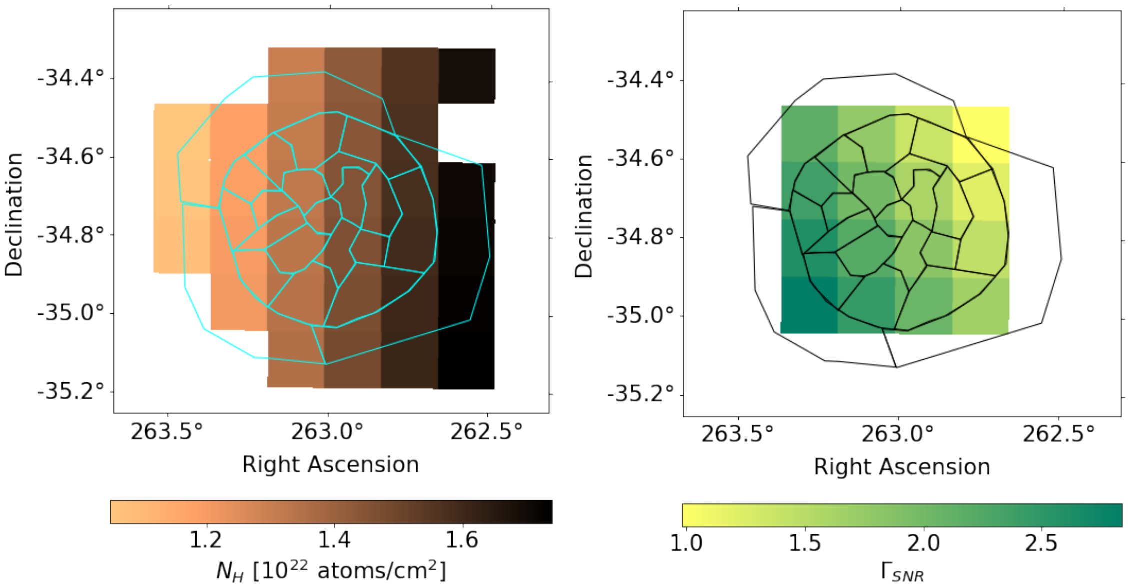

Figure 27: Visualization of the N_H gradient (left) and the Γ_{SNR} gradient (right). The corresponding numbers are given in Table 8. The absorption is increasing in western direction and the spectra are getting harder towards the north-west of the remnant. Over-plotted in cyan and black are the 22 sub-regions that Doroshenko et al. (2017) used for their *XMM-Newton* analysis. The photon index gradient is only defined for the 4 by 4 source regions, the N_H gradient for all 6 by 6 pixels minus the 6 removed due to contamination (see Sect. 4.1).

For HESS J1731-347, this is suspected to be the case, see Fig. 22 and Sect. 4.2.1. In the case of an interaction, several aspects could influence the shape of the (X-ray) spectrum: First, the magnetic field in molecular clouds tends to be stronger in areas of higher gas density. This might, on the one hand, lead to a higher maximum energy gained by particles through diffusive shock acceleration since this mechanism relies on elastic reflections of ionized particles in the magnetic field at both ends of the shock front. On the other hand, electrons are expected to lose their energy faster through synchrotron cooling, which leads to a softer spectrum. Thus, estimating the overall effect of a stronger magnetic field on the synchrotron spectrum is a complex issue. Another aspect that is expected to influence the spectrum in the case of an interaction is that the expansion velocity of the shock front is slowed down faster if the remnant is expanding into and thereby interacting with a denser environment. A slower shock expansion implies a lower maximum energy that can be gained by particles through diffusive shock acceleration (see Sect. 1.2.3). As a consequence, spectra are expected to become softer. This would be indicated by parallel N_H and Γ_{SNR} gradients, i. e. an increasing photon index in the direction of increasing absorption.

Besides differences in the spectral shape, the reduced shock expansion velocity towards a denser environment could also be an explanation for the fainter X-ray emission observed from the western part of the remnant. Doroshenko et al. (2017) found that this phenomenon is partly caused by the higher absorption, but to some extent also an intrinsic effect. As Cui et al. (2016) showed, to produce non-thermal X-ray synchrotron emission, electrons have to be accelerated to relativistic velocities which, as mentioned above, requires high shock expansion velocities. For a slower expanding shock, electrons gain less kinetic energy and therefore they predominantly produce synchrotron emission at longer wavelengths than the X-ray regime. This explanation would be in agreement with the fact that the difference in surface brightness between the eastern and western half is notable only in X-rays, while in radio and γ-rays, the remnant shows a pretty flat brightness profile (e. g. H. E. S. S. Collaboration et al. 2011). Radio synchrotron emission can still be produced by electrons accelerated at a slower expanding shock front and for the TeV emission, the hadronic scenario might become dominant. However, if there are differences in the expansion velocity across the remnant due to interactions with a cloud in the west, this interaction cannot be going on for a long time (where 'long' is meant on an astronomical scale). Otherwise, this would be expected to manifest in a somehow distorted shape of the remnant, which appears to be quite circular. As mentioned in Sect. 1.2.4, Cui et al. (2016) concluded in their evolution study of the remnant that it is expanding into a low-density region formed by the progenitor star's wind. Possibly, when it reaches the boundaries of this low-density bubble, the remnant started or will start to interact with the molecular cloud.[50]

In order to asses to which extent it is possible to trace variations in the photon index, the N_H gradient fit described in Sect. 4.2.1 was conducted again, this time not with a constant photon index across the remnant, but with the photon indices of individual regions also linked by a 2-dimensional gradient:

$$\Gamma_{ij} = \Gamma_{22} + \text{slope\_g\_x} \cdot (j-2) + \text{slope\_g\_y} \cdot (i-2) \tag{8}$$

where Γ_{ij} is the photon index of the source emission power law in region ij, i. e. the pixel in row i and column j. *slope_g_x* and *slope_g_y* denote the change in Γ when moving one pixel to the right or to the bottom, respectively. The reference region is region 22, which is the uppermost left source region. The resulting gradient slopes and absorption and photon index values calculated from them are listed in Table 8. Fig. 27 visualizes the results in an N_H map (left panel) and a Γ map (right panel). The slopes in the N_H gradient differ only slightly from those obtained for a constant Γ frozen to 2.66 (see Table 6). The total change over the analysed regions decreases from $\sim 0.8 \cdot 10^{22}$ atoms/cm^2 (for frozen Γ) to $\sim 0.7 \cdot 10^{22}$ atoms/cm^2 and values range from $N_{H,21} = 1.04 \cdot 10^{22}$ atoms/cm^2 to $N_{H,66} = 1.76 \cdot 10^{22}$ atoms/cm^2. The gradient is still oriented mainly in east-west direction and the slope in north-south direction is compatible with 0. The slopes for the photon index are significantly different from 0 in both directions at more than 3σ: *slope_g_x* $= -0.39 \pm 0.07$ and *slope_g_y* $= 0.23 \pm 0.06$. Values range from $\Gamma_{25} = 0.98 \pm 0.15$ to $\Gamma_{52} = 2.83 \pm 0.31$. This range clearly includes photon indices much smaller than it can be expected for the X-ray spectrum of an SNR. Values smaller than 1.6 are obtained for regions 24, 25 and 35. These are very dim regions where the low number of source photons makes it difficult to constrain the source model parameters.
The photon index appears to decrease towards the upper right corner of the remnant, in north-western direction. The direction of the Γ gradient is tilted with respect to the N_H gradient, which is oriented only in east-west direction. One way to assess whether the tilting is significant is to calculate the angle between the two gradient vectors and its uncertainties using the scalar product. Let φ be the angle spanned by vectors $\vec{a}$ and $\vec{b}$, then

$$\cos\varphi = \frac{\vec{a} \cdot \vec{b}}{|\vec{a}| \cdot |\vec{b}|} \tag{9}$$

where $|\vec{a}|$ and $|\vec{b}|$ are the lengths of the two vectors. Details on the calculation are given in Appendix G. The result is the following: The N_H and Γ_{SNR} gradient span an angle of $\varphi = \left(145^{+20}_{-13}\right)^\circ$. Thus, the highest value within uncertainties is 165°. An angle of 180°, for which the two vectors would be aligned, but pointing in different directions, is not covered. However, the difference in the orientation is rather small for the highest angle included in the uncertainty range.
The errors in the Γ gradient slopes are a factor of 6 and 7 larger than for the N_H gradient slopes in the y- and x-direction, respectively. This is partly due to the fact that only the 4 by 4 grid of source pixels can be used to constrain the Γ gradient, in comparison to the N_H gradient, where the inclusion of the background pixels leads to a 6 by 6 grid. Also, the uncertainty in the reference $\Gamma_{SNR,22}$ is higher than that in the reference $N_{H,14}$. As a consequence, the photon index values calculated from the gradient relation are subject to higher uncertainties than it is the case for the N_H values.
There are several reasons to take the results found in this section for the Γ gradient with care: First, the reduced statistics value does barely decrease from 0.86 to 0.84 with respect to the fit with constant

[50] The view on that is in any case a retrospective one: The distance to the remnant is ~3 kpc which corresponds to roughly 10 000 ly. Thus, the photons we observe today actually testify physical processes that happened roughly 10 000 years ago.

Γ_{SNR} and linked N_H, meaning that the data are already well represented by a model with constant photon index over the remnant. As mentioned before, in Fig. F1, the spectra of all 30 sub-regions and the best-fitting models found in Sect. 4.2.1 to 4.2.5 are plotted. There are no sub-regions for which the model with Γ_{SNR} and N_H gradient fits the spectrum considerably better than the one with constant photon index and N_H gradient. As a second point, looking at the photon indices for all sub-regions resulting from the gradient relation, the values for most of the faint regions in the western part of the remnant (at least regions 24, 25, 34, 35, 45, 55) seem unrealistically low. Constraining the Γ gradient necessarily relies also on the results of these faint regions for which the normalization of the remnant power law is at least one order of magnitude lower than for the brighter regions. Another important point to keep in mind is that parts of the Γ gradient might be artificially caused by the approximation of N_H changing as a smooth gradient. The actual behaviour of N_H across the remnant is most likely more complex, see Sect. 4.2.2. Since the parameters are correlated, an underestimation of N_H for some regions in the gradient model can lead to an artificially harder photon index of the corresponding spectra. The N_H gradient model only reflects changes of the absorption in the east-west direction, while the independent N_H fit also shows variations from south to north. Therefore, artificial Γ variations induced by the N_H gradient relation are more likely oriented perpendicular to the N_H gradient. In order to check which effect the N_H gradient model has on the results for the Γ gradient, the fit of the sub-region spectra was performed with independent N_H values and linked photon indices in the next section. Since it would not be useful to look for a physical interpretation of a possibly artificial Γ gradient component, the discussion of physical scenarios leading to a particular relative orientation of the N_H and Γ gradient is postponed to the end of the next section.

4.2.5. Fit with independent N_H and linked Γ_{SNR}

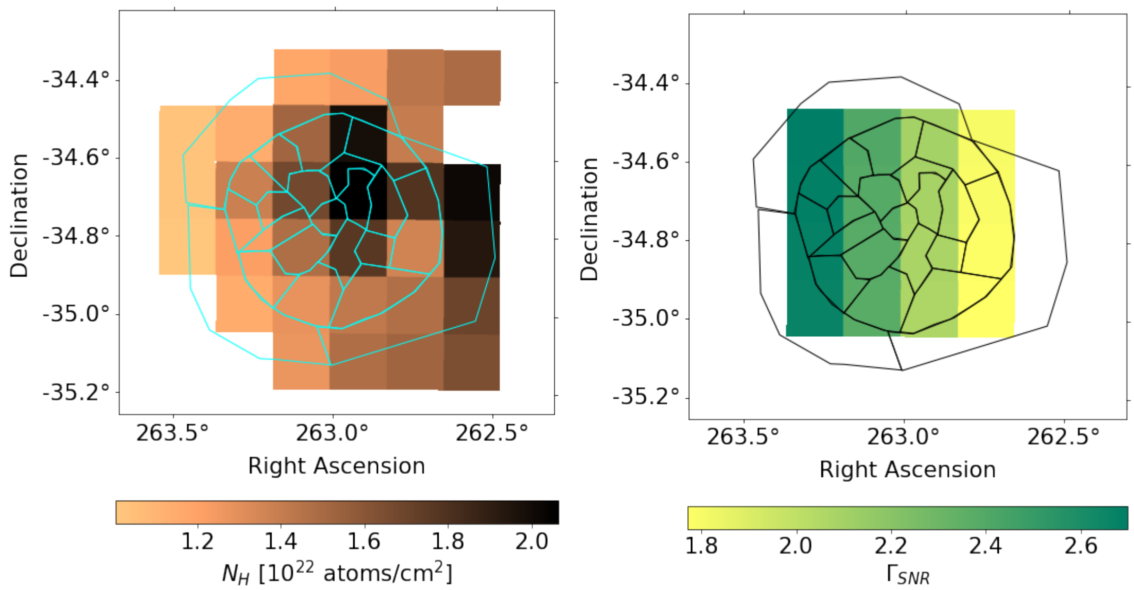

Figure 28: Visualization of the independent N_H values (left) and the Γ_{SNR} gradient (right) for the N_H independent, Γ_{SNR} linked fit. The corresponding best-fitting parameters are given in Table 9. Over-plotted in cyan and black are the 22 sub-regions that Doroshenko et al. (2017) used for their *XMM-Newton* analysis. In contrast to the previous section, where N_H was assumed to change as a smooth gradient (see Fig. 27), the photon index gradient is oriented only in east-west direction here (see text for interpretation).

Fig. 28 visualizes the results for the absorption and photon index of the sub-regions when N_H is allowed to vary independently and Γ_{SNR} is linked by a gradient relation according to Eq. 8. The corresponding parameter values and uncertainties are listed in Table 9. The results for the absorptions

Table 9: Best-fitting parameters for the simultaneous fit of the spectra of the 30 sub-regions shown in Fig. 20 with independent N_H and Γ_{SNR} linked by a 2-d gradient relation between individual regions. The Γ values for all regions except the reference region 22 were calculated according to Eq. 8. An error propagation for statistical errors was conducted, see caption of Table 6 for details. Absorptions are given in units of 10^{22} atoms/cm^2, power law normalizations in units of photons/cm^2/s. The gradient slopes are defined as change per pixel, i. e. over a distance of 8.75′. 'nan' entries mean that the confidence bounds could not be determined (often the case for parameter results close to the allowed minimum or maximum).

par	val	lower error	upper error	par	val	lower error	upper error
nh13.nH	1.18	-0.06	+0.07	pl_snr23.PhoIndex	2.40	-0.25	+0.25
nh14.nH	1.23	-0.06	+0.07	pl_snr24.PhoIndex	2.09	-0.22	+0.22
nh15.nH	1.44	-0.08	+0.09	pl_snr25.PhoIndex	1.79	-0.25	+0.25
nh16.nH	1.48	-0.09	+0.10	pl_snr32.PhoIndex	2.70	-0.36	+0.37
nh21.nH	1.03	-0.05	+0.05	pl_snr33.PhoIndex	2.39	-0.30	+0.30
nh22.nH	1.14	-0.07	+0.07	pl_snr34.PhoIndex	2.09	-0.27	+0.27
nh23.nH	1.52	-0.09	+0.09	pl_snr35.PhoIndex	1.78	-0.30	+0.30
nh24.nH	1.99	-0.16	+0.19	pl_snr42.PhoIndex	2.69	-0.42	+0.42
nh25.nH	1.40	-0.08	+0.14	pl_snr43.PhoIndex	2.39	-0.36	+0.37
nh31.nH	1.02	-0.05	+0.05	pl_snr44.PhoIndex	2.08	-0.34	+0.35
nh32.nH	1.38	-0.07	+0.08	pl_snr45.PhoIndex	1.78	-0.36	+0.37
nh33.nH	1.68	-0.08	+0.08	pl_snr52.PhoIndex	2.68	-0.49	+0.49
nh34.nH	2.06	-0.15	+0.16	pl_snr53.PhoIndex	2.38	-0.44	+0.44
nh35.nH	1.79	-0.15	+0.19	pl_snr54.PhoIndex	2.08	-0.43	+0.42
nh36.nH	2.02	-0.17	+0.21	pl_snr55.PhoIndex	1.77	-0.44	+0.44
nh41.nH	1.00	-0.05	+0.05	pl_snr22.norm	0.00064	-0.00013	+0.00016
nh42.nH	1.21	-0.07	+0.07	pl_snr23.norm	0.00296	-0.00040	+0.00049
nh43.nH	1.48	-0.07	+0.08	pl_snr24.norm	0.00152	-0.00030	+0.00040
nh44.nH	1.76	-0.11	+0.13	pl_snr25.norm	0.00000	nan	0.00009
nh45.nH	1.36	-0.08	+0.09	pl_snr32.norm	0.00444	-0.00054	+0.00062
nh46.nH	1.94	-0.16	+0.19	pl_snr33.norm	0.00579	-0.00055	+0.00063
nh52.nH	1.14	-0.07	+0.07	pl_snr34.norm	0.00197	-0.00032	+0.00040
nh53.nH	1.28	-0.07	+0.08	pl_snr35.norm	0.00029	-0.00010	+0.00013
nh54.nH	1.42	-0.09	+0.10	pl_snr42.norm	0.00244	-0.00031	+0.00037
nh55.nH	1.47	-0.08	+0.17	pl_snr43.norm	0.00313	-0.00031	+0.00035
nh56.nH	1.70	-0.12	+0.14	pl_snr44.norm	0.00193	-0.00028	+0.00035
nh63.nH	1.27	-0.07	+0.07	pl_snr45.norm	0.00047	-0.00011	+0.00013
nh64.nH	1.47	-0.09	+0.10	pl_snr52.norm	0.00048	-0.00012	+0.00014
nh65.nH	1.52	-0.10	+0.11	pl_snr53.norm	0.00285	-0.00037	+0.00044
nh66.nH	1.64	-0.11	+0.12	pl_snr54.norm	0.00086	-0.00015	+0.00019
pl_snr22.PhoIndex	2.70	-0.19	+0.20	pl_snr55.norm	0.00000	nan	+0.00009
slope_g_y.factor	-0.01	-0.09	+0.09				
slope_g_x.factor	-0.30	-0.12	+0.12				
red. stat.				0.84			

agree well with those found when fixing $\Gamma_{SNR} = 2.66$ for all regions (see Sect. 4.2.2 and in particular Fig. 23 left). Fig. 29 directly compares the independent N_H values for all regions for the case of fixed (blue, Sect. 4.2.2) and the case of linked (red, this section) photon indices. The results agree within 1σ confidence bounds. The left panel of Fig. 30 compares the N_H values for linked photon indices when N_H is also linked by a gradient relation (blue markers, Sect. 4.2.4) and when N_H can

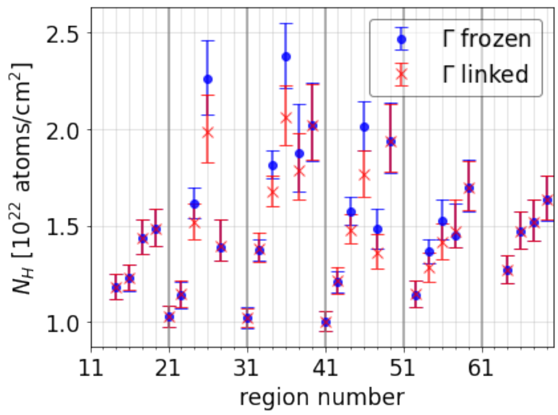

Figure 29: Comparison of the independent N_H values obtained from the fit in Sect. 4.2.2 with a frozen photon index (blue) and the ones found in this section (red) with a linked photon index between regions according to Eq. 8. Thick grey lines indicate the start of a new pixel row.

vary independently between the regions (red markers, this section). For some of the regions with high independent N_H values, there are large deviations to the gradient model, very similar to those found for a frozen photon index (see Sect. 4.2.3). For several other regions, however, the agreement of the N_H values is good. As a major difference to the N_H linked, Γ linked fit in the previous section, the photon index gradient is oriented only in east-west direction in the case of independent N_H values. This indicates that the component of the Γ_{SNR} gradient in Sect. 4.2.4 that is perpendicular to the N_H gradient (i. e. oriented in south-north direction) is indeed an artificial effect caused by the model representation of the N_H variations. Also, the range of photon indices across the remnant seems more reasonable for the case of independent N_H values, where it starts at $\Gamma_{44} = 1.8 \pm 0.4$ and goes up until $\Gamma_{22} = 2.7 \pm 0.2$. The results for the slopes are $slope\_g\_x = -0.30 \pm 0.12$ and $slope\_g\_y = -0.01 \pm 0.09$. Thus, the uncertainties in the Γ gradient slopes, which were already large for the N_H linked, Γ linked fit in Sect. 4.2.4, are again 1.5 to 2 times as large for independent N_H values. This is a consequence of the additional free parameters. The right panel of Fig. 30 shows the photon index values calculated from the gradient relation for both independent (red) and linked (blue) N_H. Errors are obtained from a statistical error propagation as described in the caption of Tab. 6 for the absorptions. For the case of independent N_H values, the uncertainties on the photon indices of the regions are so large that the change across each pixel row is hardly significant (especially with increasing distance to the reference pixel towards the southern part). This demonstrates again the limits imposed by counting statistics. Still, the Γ gradient slope in x-direction obtained from the fit is significant at more than 2σ. The reduced statistics value does not decrease considerably with respect to the N_H linked, Γ linked fit in Sect. 4.2.4, meaning that the additional free parameters are statistically not justified. Nevertheless, the results of the current section seem more reasonable from a physical point of view, mainly judging by the range of the photon index values.

Summarizing again the finding of this section, the spectrum of the remnant seems to harden in the direction where the absorption is increasing, likely because of a nearby molecular cloud. Therefore, the behaviour of the photon index seems to be the opposite of the expectation described at the beginning of Sect. 4.2.4: Instead of becoming softer towards regions where the remnant is potentially interacting with a denser environment, the spectra appear to be harder in this area. Therefore, this finding cannot be explained in the simple picture of a slower shock expansion as a consequence of interactions with a dense environment that has been discussed before. As a caveat of this result, it cannot be ruled out completely that the change in the photon index is (partly) caused by stray light originating from the nearby X-ray binary 1RXS J173157.7-335007. eROSITA is expected to handle this issue much better than *XMM-Newton*. Still, also a smaller, unnoticed contamination might have an effect on the analysis. The contaminating source is located in northern direction from the remnant. However, since the origin of single reflection photons is not reconstructed correctly, it could also influence the photon index of the spectra towards other directions. Doroshenko et al. (2017) initially also found harder spectra for sub-regions in the north-western part of the remnant in their analysis. A more careful investigation conducted by the authors then revealed that the hardening was caused by the increasing stray light contamination in that exact direction. This artificial effect was still present after they excluded all data where a stray light contamination was visible by eye in the image. Before Doroshenko et al. (2017), Bamba et al. (2012) also analysed the spatial variations of N_H and Γ for 13 sub-regions of HESS J1731-347, in this case using *Suzaku* observations.[51] As a general caveat, the *Suzaku* observations are likely affected by stray light contamination to a similar extent as it is the case for *XMM-Newton*. Because of a different instrument geometry, the contamination for *Suzaku* can be expected to be more diffuse and not to manifest in arc-like structures. Bamba et al. (2012) did not remove stray light contamination in their analysis. Therefore, this might have also influenced the photon index variations they found. Their photon index values range from 1.77 to 3.17. In a second analysis step, Bamba et al. (2012) combined the spectra of several sub-regions to trace the changes in 3 larger sub-areas, namely the northwest, center-east and southern part of the remnant, and re-fitted the joined data sets. They found the hardest photon index in the northwest (1.97), followed by the center-east (2.36) and the softest in the southern part (2.63), thus a hardening in roughly north-western direction. Bamba et al. (2012) suspected that this indicates the presence of a spectral break in the remnant spectrum (i. e. the spectrum has such a shape that it can be modelled with different photon indices in different energy ranges). A similar phenomenon was found e. g. by Takahashi et al. (2008) for a different galactic SNR, RX J1713.7-3946. Amongst other approaches, the authors fitted the spectrum with a broken power law, finding a photon index of 2.18 ± 0.03 for lower energies and a photon index of 2.53 ± 0.02 for higher energies with the a break energy of 3.13 ± 0.15 keV. In this context, harder photon indices towards the western part could signify that radiation from there is predominantly emitted in the energy regime below the cutoff and therefore can be described by a harder spectrum. This would be in agreement with a slowing-down of the shock expansion speed towards a denser environment and consequently a lower maximum energy gained by electrons through diffusive shock acceleration. An indication against the presence of a spectral break is that in the spectral fit of the total source, there was no hint that a model with the same photon index over the entire energy range is not suitable to represent the data. Certainly, the emission from the brighter eastern half is dominant and it might be the case that the spectral break remains unnoticed because the western part is much fainter and also because of the poor counting statistics. On the other hand, also for the *XMM-Newton* data analysed by Doroshenko et al. (2017) with much better counting statistics, a model with a uniform photon index was selected as appropriate representation of the data.

In order to draw a connection between the photon index variations found in the fit and the change of the spectral shape from the eastern to the western part of the remnant, Fig. 31 shows a comparison of some sub-region spectra. In the left panel, the region 32 spectrum is compared to that of region 34 which is further in the west. The right panel shows the spectra of regions 32 and 34, again one from the southern and the other from the western part. The comparisons show that the count rate is mostly reduced between ~ 0.6 keV and $\sim 1-1.5$ keV towards the western part, see Fig. 31. For reference, the source emission is the dominant spectral component between ~ 0.9 keV and ~ 2.8 keV (see Fig. 17). Thus, the decrease in the softer X-ray source emission is stronger than in the harder X-rays. This speaks against the presence of a spectral break, at least under the assumption that the photon index in the low-energy regime below the break is harder than that above the break. In this case, harder photon indices would indicate that spectra are dominated by softer energies, which does not seem to be the case for HESS J1731-347 since the count rate decreases stronger for energies between ~ 0.6 keV and $\sim 1-1.5$ keV towards the western part than for higher energies. Assuming that no spectral break is present and the spectrum can be fitted with a uniform photon index over the entire energy range (which seems to be likely), it is not surprising that the fit resulted in harder photon indices towards the western part of the SNR when looking at the plots of the spectra in Fig. 31. However, it cannot be disentangled

[51] These observations do not provide a complete coverage of the remnant, in contrast to the *XMM-Newton* data analysed by Doroshenko et al. (2017).

by eye to what extent the stronger decrease in a particular energy range below ∼ 1 − 1.5 keV might be caused by the stronger absorption, which can affect different energy ranges in a different way. Absorption variations could lead to spectra appearing harder although they intrinsically are not if softer X-ray radiation is more affected by a higher absorption. However, this effect should in principle be accounted for by models that consider absorption variations and therefore it should not affect the photon index values. Under the assumptions that this works as intended, that there are no other issues with the spectral model and that stray light issues are indeed negligible for eRSOITA, the hardening of the spectra towards the western part of the remnant could be considered an intrinsic effect of the source.

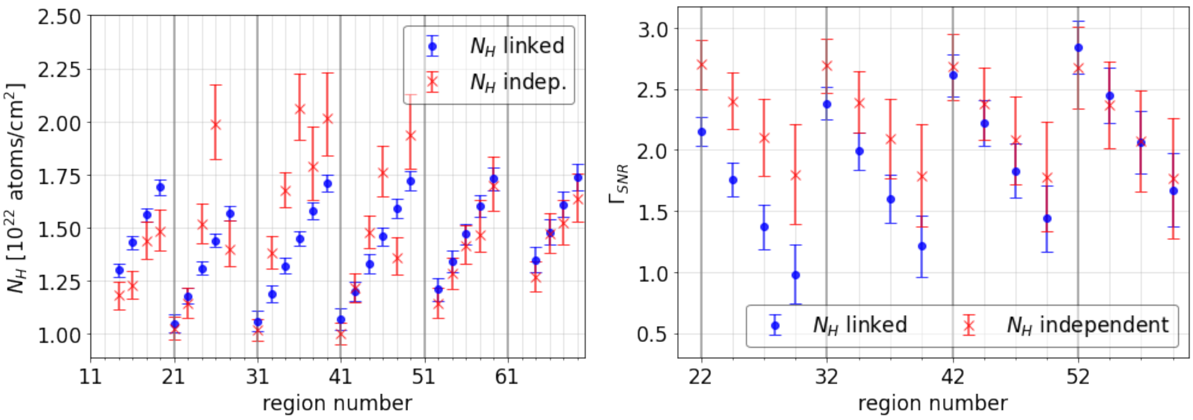

Figure 30: *Left panel:* Comparison of N_H values from the linked fit in the previous section (blue) and the independent fit in this section (red). Γ_{SNR} is linked in both cases. *Right panel:* Comparison of Γ_{SNR} values from the N_H linked, Γ_{SNR} linked fit in the previous section (blue) and the N_H independent, Γ_{SNR} linked fit in this section (red).

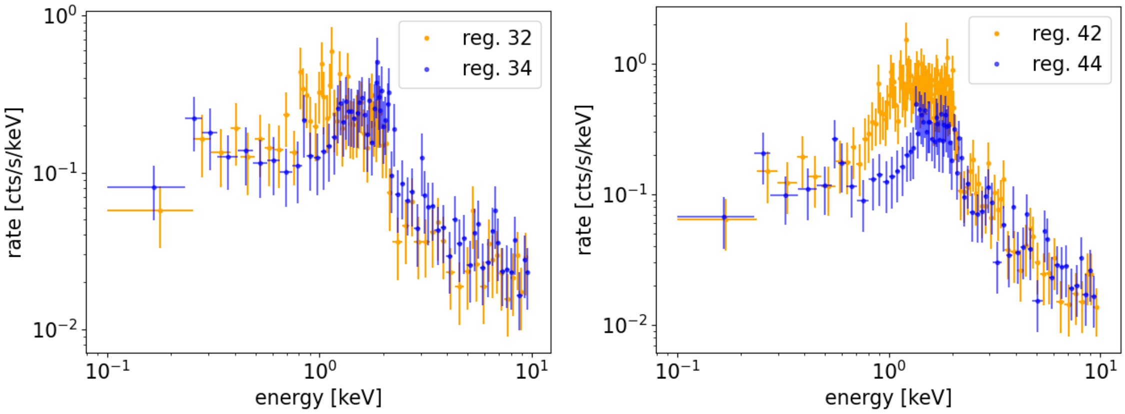

Figure 31: Comparison of two pairs of sub-region spectra, where the orange ones are extracted from the eastern part of the remnant and the blue ones from the eastern part. There are clear differences in the count rate decrease from east to west for different energy ranges.

If this is the case, one possible explanation might be a weaker magnetic field of the remnant in the western area. In this case, the synchrotron cooling time scale for electrons would be longer and therefore they would longer be able to produce higher-energy radiation than in areas with a stronger magnetic field. On the other hand, also the maximum energy of electrons gained through diffusive shock acceleration might be lower for a weaker magnetic field. As already mentioned, estimating the overall effect of the magnetic filed strength on the spectrum is a complex issue. Also, empirically, the magnetic field in molecular clouds tends to be stronger rather than weaker in regions of higher density. Besides harder spectra, the regions in the western part of the remnant also show a dimmer X-ray emission. This could, when disregarding the absorption pattern for a moment, actually be an indication for interactions with a less dense environment: Cassam-Chenai et al. (2004) analysed variations of X-ray emission and spectral model parameters across the galactic SNR RX J1713.7-3946. They found an increased X-ray brightness for regions with larger X-ray absorption (see their Fig. 6), which seems to be a contrary case to that of HESS J1731-347. The authors concluded that the interaction of RX J1713.7-3946 with denser material leads to an amplified X-ray emission. Further, they found higher photon indices for regions with stronger absorption within their source (see their Fig. 4), which is another contrary result to the finding of this section for HESS J1731-347. Cassam-Chenai et al. (2004) also produced hardness ratio maps (see their Fig. 8) of the 0.7–0.9 keV to 1.0–1.3 keV band and 5–8 keV to 1.6–2.0 keV band. The count ratio in the 0.7–0.9 keV to 1.0–1.3 keV band clearly decreases in the stronger absorbed regions in the south-west of their remnant, which indicates that the 0.7–0.9 keV emission is stronger absorbed or for a different reason less bright in this area. Apparently, this does not lead to a hardening of the spectra, possibly because it is indeed absorption-related and accounted for by varying absorptions in the model. The hardness ratio of the 5–8 keV to 1.6–2.0 keV band seems not show a behaviour that is correlated with increasing absorption (see Fig. 8 right panel of Cassam-Chenai et al. 2004). Judging from the sub-region spectra of HESS J1731-347 plotted in Fig. 31, a decrease in the hardness ratio for stronger absorbed regions can also be expected in this case when choosing appropriate energy ranges.

Apart from that, there is one other common finding of the analysis of HESS J1731-347 conducted in this Thesis work with the study of RX J1713.7-3946 by Cassam-Chenai et al. (2004): Photon indices tend to be softer in brighter regions. However, a positive correlation of absorption and X-ray brightness as it was found by Cassam-Chenai et al. (2004) for RX J1713.7-3946 can most likely be ruled out for HESS J1731-347. The absorption variations found in the X-ray spectral analysis in this Thesis and by Doroshenko et al. (2017), as well as the ^{12}CO absorption and brightness temperature maps (see Fig. 22) clearly speak against it. The intrinsic as well as the observed X-ray brightness become dimmer in stronger absorbed regions. Thus, if there is an interaction taking place with the molecular cloud, it seems to impede the production of X-ray synchrotron emission in some not yet constrained way rather than enhance it.

4.3. Fit of spectra from sub-regions adapted to the surface brightness of the source as measured with XMM-Newton

In order to be able to more directly compare the results of the spatially resolved spectral analysis to those obtained by Doroshenko et al. (2017) from *XMM-Newton* data, the merged eRASS 1 to 4 spectra of the remnant were extracted for the same sub-regions as used by these authors. In Sect. 4.3.1, all regions were fitted simultaneously with a constant photon index of $\Gamma_{SNR} = 2.66$ (the result of Doroshenko et al. 2017) and the N_H value of each region was an independent, free parameter. In Sect. 4.3.2, the N_H values were fixed to the results obtained by Doroshenko et al. (2017) and the photon index was constrained for each region independently.
In both cases, the cosmic X-ray background model parameters were frozen to the results obtained from the simultaneous fit of the source and background region in Sect. 3.3. The model was renormalized for each region, using its respective REGAREA ratio to the total background annulus. The instrumental background was renormalized using the BACKSCAL ratio.

4.3.1. Constraining absorptions for a fixed photon index

The left panel of Fig. 32 shows a color map of the absorption results for the 22 regions defined by Doroshenko et al. (2017) using eRASS:4 data. In the right panel, the original results of Doroshenko et al. (2017) are displayed for comparison. The pattern as well as the range of the values otained

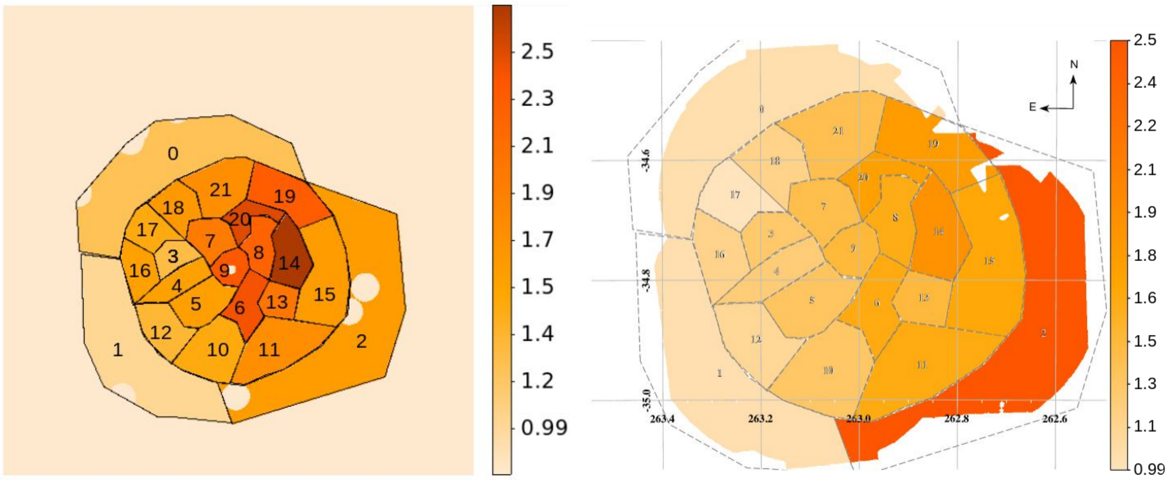

Figure 32: *Left panel:* N_H values from the eRASS:4 data analysis for the 18 source and 3 background regions defined by Doroshenko et al. (2017). *Right panel:* Original results of Doroshenko et al. (2017) for their spectral analysis of *XMM-Newton* data, see their Figure 2, right panel. The scale of the color map has been reproduced to increase the font size. The circles in the map of the left panel correspond to contaminating point sources that were removed from the background regions before the spectrum extraction. Within the source region, only the CCO was removed (see circle in the center).

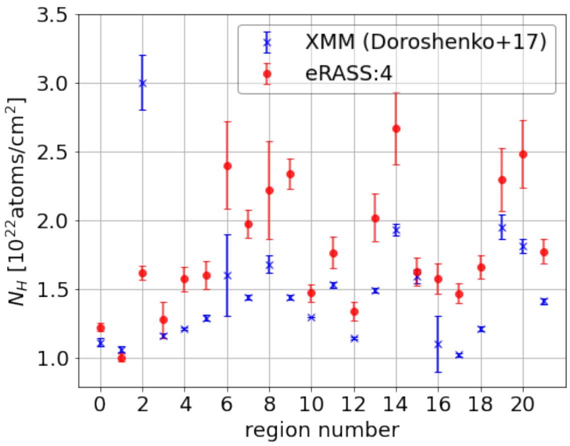

Figure 33: N_H values from the analysis of Doroshenko et al. (2017) (blue) plotted versus the region numbers. The red markers show the results for the spectra of the same regions for the eRASS:4 data analysis conducted in this Thesis.

from the eRASS:4 analysis is in good agreement with the results of Doroshenko et al. (2017). The largest difference is in the result of background region 2: $N_{H,\mathrm{eRASS}} = (1.54^{-0.05}_{+0.05}) \cdot 10^{22}$ atoms/cm^2, $N_{H,\mathrm{XMM}} = (3.0 \pm 0.2) \cdot 10^{22}$ atoms/cm^2. The spectra and best-fitting models of all regions are shown in Appendix H, together with the best-fitting models from the next Sect. 4.3.2. It is evident in these plots that the model for background region 2 with N_H frozen to the significantly higher value obtained by Doroshenko et al. (2017) does not represent the spectrum very well. The N_H value of Doroshenko et al. (2017) for this region seems not to be compatible with the data for the fitting approach chosen here, namely freezing the background model parameters to the values obtained from the simultaneous fit in Sect. 3.3, rescaling them accordingly and letting only the absorption vary as a free parameter. Probably, the spectrum could be represented by a model with this absorption value if the other parameters were also different.
The best-fitting values for the free parameters in the eRASS:4 analysis are listed in Table 10. Fig. 33

Table 10: Fit results using eRASS:4 data for the 22 regions defined by Doroshenko et al. (2017) when fixing the photon index to 2.66 for all regions. Absorptions are given in units of 10^{22} atoms/cm^2, power law normalizations in units of photons/cm^2/s. The numbers of the regions are over-plotted in Fig. 32, left.

par	val	lower err	upper err	par	val	lower err	upper err
nh0.nH	1.12	-0.03	+0.03	pl_snr3.norm	0.0003	-0.0001	+0.0001
nh1.nH	0.97	-0.03	+0.03	pl_snr4.norm	0.0025	-0.0002	+0.0002
nh2.nH	1.54	-0.05	+0.05	pl_snr5.norm	0.0014	-0.0002	+0.0002
nh3.nH	1.22	-0.12	+0.13	pl_snr6.norm	0.0010	-0.0002	+0.0003
nh4.nH	1.50	-0.08	+0.09	pl_snr7.norm	0.0043	-0.0003	+0.0003
nh5.nH	1.52	-0.10	+0.10	pl_snr8.norm	0.0006	-0.0002	+0.0002
nh6.nH	2.26	-0.27	+0.32	pl_snr9.norm	0.0058	-0.0004	+0.0004
nh7.nH	1.92	-0.10	+0.10	pl_snr10.norm	0.0034	-0.0002	+0.0003
nh8.nH	2.04	-0.27	+0.35	pl_snr11.norm	0.0014	-0.0002	+0.0002
nh9.nH	2.31	-0.11	+0.11	pl_snr12.norm	0.0026	-0.0002	+0.0002
nh10.nH	1.40	-0.06	+0.07	pl_snr13.norm	0.0015	-0.0002	+0.0002
nh11.nH	1.66	-0.11	+0.12	pl_snr14.norm	0.0018	-0.0003	+0.0004
nh12.nH	1.28	-0.06	+0.06	pl_snr15.norm	0.0008	-0.0002	+0.0002
nh13.nH	1.93	-0.16	+0.17	pl_snr16.norm	0.0013	-0.0002	+0.0002
nh14.nH	2.60	-0.24	+0.26	pl_snr17.norm	0.0033	-0.0002	+0.0002
nh15.nH	1.51	-0.09	+0.10	pl_snr18.norm	0.0033	-0.0003	+0.0003
nh16.nH	1.49	-0.10	+0.11	pl_snr19.norm	0.0012	-0.0002	+0.0003
nh17.nH	1.40	-0.07	+0.07	pl_snr20.norm	0.0018	-0.0003	+0.0003
nh18.nH	1.60	-0.08	+0.08	pl_snr21.norm	0.0035	-0.0003	+0.0003
nh19.nH	2.19	-0.20	+0.23				
nh20.nH	2.42	-0.22	+0.24				
nh21.nH	1.71	-0.09	+0.09				
red. stat.	0.87						

shows a direct comparison of the N_H result for each of the 22 regions from the *XMM-Newton* analysis of Doroshenko et al. (2017) and the eRASS:4 analysis described in Sect. 4.3 above. In most cases, there is a good agreement of the relative change of the absorption from one region to the next. The most prominent outlier is background region 2. Uncertainties are much smaller for the *XMM-Newton* analysis than for eRASS:4 which is a consequence of the longer exposure with *XMM-Newton*. The results from the eRASS:4 analysis are systematically higher which could be due to the use of the *tbabs* absorption model instead of the *wabs* model and the corresponding differences in the abundance selection (see Sect. 3.2).

4.3.2. Constraining photon indices for fixed absorptions

Since the counting statistics of the eRASS:4 data do not allow to fit the 22 regions with independent N_H and Γ parameters and absorption values were already constrained by Doroshenko et al. (2017), in this section, the absorption of each region was frozen to the respective result of Doroshenko et al. (2017) and the photon index was allowed to vary independently between the regions. The resulting photon index pattern is visualized in Fig. 34. Table 11 lists the corresponding best-fitting parameter values. Just as in Sect. 4.3.1, the background model parameters were frozen to the results obtained in Sect. 3.3.5 with normalizations rescaled accordingly, as described in Sect. 3.3.1. The reduced statistics value when fixing the N_H values and constraining the photon indices is slightly higher than that in the previous section (red. stat.=0.91 versus 0.87). For two regions in the western half of the remnant close to the center (region 6 and 8), the photon index is smaller than 1.5 which is a highly questionable result. Looking at Fig. 2 left of Doroshenko et al. (2017), these are very dim regions which hardly show any source emission in the image. Thus, constraining a photon index for these spectra is difficult, even more for the eRASS:4 observations with lower counting statistics. The issue of unreliable Γ results for dim regions was also discussed before in Sect. 4.2.4. The median of the photon indices of all regions is plotted in Fig. 34, right panel and is slightly below 2.0. This is lower than what can be expected looking at the results for the total remnant of Doroshenko et al. (2017) ($\Gamma + 2.66 \pm 0.01$) and also obtained in previous sections for background subtraction ($\Gamma_{SNR} \approx 2.8 \pm 0.3$) and background modelling ($\Gamma_{SNR} \approx 2.2 \pm 0.1$). In order to check whether there is a correlation evident by eye between the photon indices of the 19 source regions and the N_H values fixed to the results of Doroshenko et al. (2017), the latter are plotted as grey crosses on the secondary y-axis in Fig. 34, right. The variations of N_H and Γ appear not to be in an evident, fixed relation to each other.

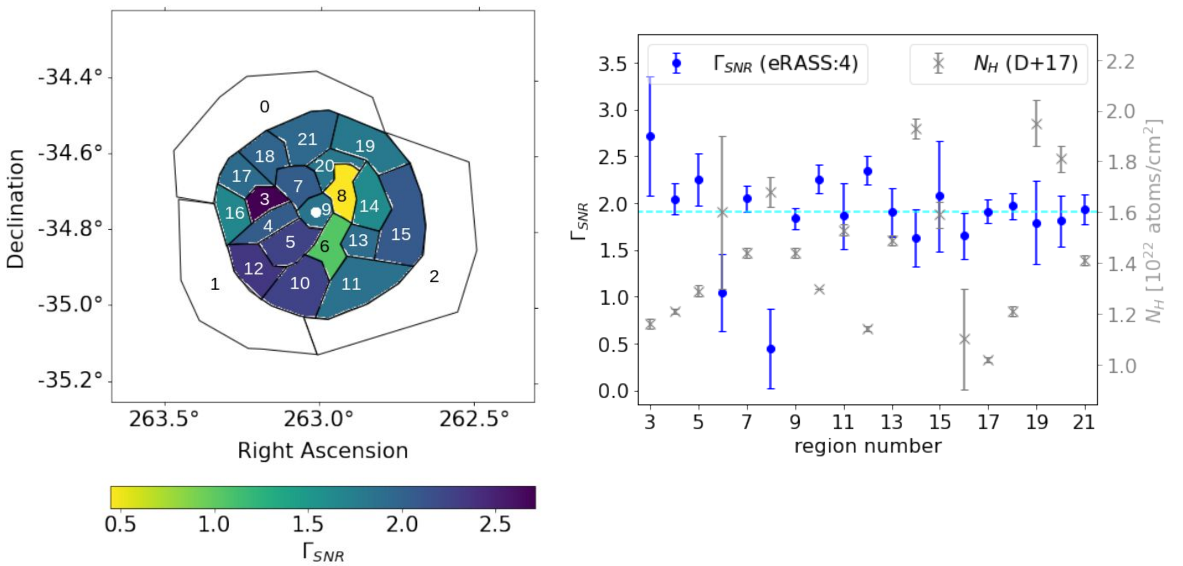

Figure 34: *Left panel:* Color map visualization of the photon index values obtained using eRASS:4 data with absorptions fixed to the results of Doroshenko et al. (2017). *Right panel:* Different representation including uncertainties. The region numbers plotted on the x-axis are the same that are overlayed on the map in the left panel. The cyan dashed line marks the median of the 19 photon index values. The grey crosses plotted on the secondary y-axis represent the N_H values found by Doroshenko et al. (2017) to which the absorptions were fixed in the fit. There is no correlation evident by eye between the N_H and Γ pattern.

As mentioned in the previous section, the spectra and best-fitting models of all 22 regions are shown in Appendix H. For background region 2 and region 9, the model with variable photon index and N_H fixed to the result of Doroshenko et al. (2017) clearly fits the data better than the one with fixed photon index and variable N_H. However, the unphysical results for regions 6 and 8 and the large uncertainties on many of the photon index values show that the results of this approach are not reliable for the given counting statistics.

Table 11: Photon index and power law normalization results for the 22 regions defined by Doroshenko et al. (2017) when fixing the absorption for each region to the value obtained by these authors (see their Table 2 and Fig. 33 in the previous section). Normalizations are given in units of photons/cm^2/s.

par	val	lower error	upper error	par	val	lower error	upper error
pl_snr3.PhoIndex	2.71	-0.60	+0.64	pl_snr3.norm	0.010	-0.003	+0.003
pl_snr4.PhoIndex	2.05	-0.16	+0.16	pl_snr4.norm	0.040	-0.004	+0.004
pl_snr5.PhoIndex	2.25	-0.27	+0.28	pl_snr5.norm	0.018	-0.003	+0.003
pl_snr6.PhoIndex	1.04	-0.38	+0.41	pl_snr6.norm	0.005	-0.001	+0.002
pl_snr7.PhoIndex	2.05	-0.13	+0.13	pl_snr7.norm	0.057	-0.005	+0.005
pl_snr8.PhoIndex	0.44	-0.40	+0.42	pl_snr8.norm	0.003	-0.001	+0.001
pl_snr9.PhoIndex	1.84	-0.11	+0.11	pl_snr9.norm	0.084	-0.006	+0.007
pl_snr10.PhoIndex	2.26	-0.15	+0.15	pl_snr10.norm	0.033	-0.003	+0.003
pl_snr11.PhoIndex	1.86	-0.32	+0.35	pl_snr11.norm	0.009	-0.002	+0.002
pl_snr12.PhoIndex	2.35	-0.15	+0.16	pl_snr12.norm	0.039	-0.003	+0.003
pl_snr13.PhoIndex	1.90	-0.25	+0.26	pl_snr13.norm	0.025	-0.004	+0.004
pl_snr14.PhoIndex	1.62	-0.29	+0.30	pl_snr14.norm	0.012	-0.002	+0.003
pl_snr15.PhoIndex	2.07	-0.52	+0.60	pl_snr15.norm	0.006	-0.002	+0.002
pl_snr16.PhoIndex	1.65	-0.24	+0.25	pl_snr16.norm	0.014	-0.002	+0.002
pl_snr17.PhoIndex	1.91	-0.12	+0.13	pl_snr17.norm	0.043	-0.003	+0.003
pl_snr18.PhoIndex	1.97	-0.14	+0.14	pl_snr18.norm	0.042	-0.003	+0.004
pl_snr19.PhoIndex	1.79	-0.40	+0.44	pl_snr19.norm	0.009	-0.002	+0.003
pl_snr20.PhoIndex	1.81	-0.26	+0.27	pl_snr20.norm	0.026	-0.004	+0.005
pl_snr21.PhoIndex	1.94	-0.15	+0.16	pl_snr21.norm	0.027	-0.003	+0.003
red. stat.				0.91			

5. Outlook: Simulating eROSITA spectra with a larger exposure

5.1. Method description

Since the eROSITA observations of HESS J1731-347 are not (notably) affected by stray light, in contrast to the *XMM-Newton* observations (Doroshenko et al., 2017), eROSITA observations of the remnant with a longer exposure would be a promising foundation to further constrain its properties in the X-ray regime. In particular, better counting statistics can be expected to enable a more reliable and more detailed analysis of the photon index variations.

In order to investigate the expected uncertainties in constraining the photon index for one single sub-pixel with longer exposure, the eROSITA spectra of the remnant were used to simulate several spectra with longer exposures which were then fitted. In a second step, a 4 by 4 set of Γ values with the uncertainties obtained from the simulated spectral fit were fitted with a 2d gradient relation and the uncertainties in the gradient slopes were determined.

For simplicity, the spectrum of the total remnant was used for the simulations. The extraction area of this spectrum is 12.5 times as large as that for the single pixels displayed in Fig. 20. Thus, the exposure of the simulated spectra was multiplied by a factor of 12.5 to estimate the exposure that would be needed for a generic sub-pixel in order to detect a number of counts comparable to that of the simulated total remnant spectrum. Proceeding like that, the resulting simulated spectra are expected to rather represent those of the brightest source pixels since they dominate the emission of the total source. Thus, the uncertainties in the photon indices and gradient slopes are probably underestimated for this case. In reality, constraining Γ variations involves also the spectra of dimmer source regions in the western part of the remnant which are subject to larger uncertainties. In order to take that into account, the uncertainties in the photon index were in a second step also determined for fainter spectra which were simulated by rescaling the normalization of the source emission power law by the count ratio of the spectrum of a faint source region (region 45) to a bright one (region 33), which is 165 cts/367 cts$\approx$ 0.45.[52]

The simulations were carried out using the *fakeit* command of the X-ray spectral fitting package *XSPEC*[53]. The required input is a source spectrum, a source model, a background spectrum and the desired exposure. The total source spectrum and background annulus spectrum were used and for the source model an absorbed power law with the parameters frozen to the results of the background subtracted fit of the total source (see Sect. 3.2). The resulting simulated spectrum comprises then the combined source and background emission. Additionally, a separate simulated background spectrum for the respective exposure is produced as output. The reason to use XSPEC instead of sherpa in this case was that XSPEC is able to simulate this background spectrum without requiring a background model. The simulation is based on the real background spectrum.

Before fitting the simulated source spectrum, a background subtraction was performed. From these fits, the relation between the exposure and the uncertainty in the photon index of a single pixel was estimated. In a second step, a hypothetical set of 4 by 4 photon index values representing all source pixels in Fig. 20 was fitted with a 2-dimensional gradient. For simplicity, the photon index was assumed to be constant for all 4 by 4 regions and all were assumed to have the same photon index uncertainty obtained from the fit of the simulated spectrum. Only the gradient slope uncertainty in

[52]This ratio is calculated based on the counts in eRASS 4 only due to an inaccuracy in the extraction procedure that was discovered later: When extracting a joined spectrum from 4 event files corresponding to the 4 eRASS surveys, the header of the resulting PHA data set contains the counts of eRASS 4 under the 'CTS' keyword, not the summed up counts of all surveys. However, for an approximate scaling between bright and dim regions, the ratio in eRASS 4 is sufficient.

[53]version 12.12.1

one direction was analysed and considered in the result plots. Since the photon index is assumed to be constant, i. e. the injected slope is 0 in the east-west as well as in the north-south direction, the error obtained from the fit is symmetrical in both directions. The fit of the photon index set was performed with sherpa using the *Polynom2d()* function. Except for the linear $x-$ and $y-$terms and the constant offset, all parameters were frozen to 0. The χ^2 statistics and *neldermead* optimization method was used for the fit and 1σ confidence bounds were calculated with the *Projection()* method.
The same procedure was repeated for the absorption column density N_H.
This is overall a more conservative analysis approach than the one applied in the analysis of the eRASS:4 spectra. On the one hand because background subtraction was used to fit the simulated spectra instead of background modelling. And on the other hand because the gradient slopes of N_H and Γ variations were not constrained from the spectral fitting itself, but fitted to the explicitly determined N_H and Γ values. These two differences are expected to increase statistical uncertainties. Nevertheless, the simulation results serve as an indication how precisely in particular photon index variations could be constrained with longer eROSITA observations.

5.2. Results

Fig. 35 shows in the left panel the uncertainties in the photon index resulting from the background subtracted fit of the simulated spectrum for the respective exposure on the x-axis. Since the spectrum of the total source was used for the simulation, which was extracted from an area that is 12.5 times as large as that of a single pixel (see method description in Sect. 5.1), the actual eRASS:4 exposure of ~ 2 ks corresponds already to an exposure of 25 ks for a single pixel, which is the first data point in the plot.[54] The data was fitted with a function of the form $y = c/\sqrt{x}$ which is the expected relation for uncertainties as a function of counts (and therefore exposure) in Poisson statistics. In the middle panel of Fig. 35, the uncertainty in the gradient slope (in one arbitrary direction) is displayed as a function of the photon index uncertainty when fitting a constant set of 4 by 4 photon index values with equal uncertainties with a 2-dimensional linear gradient in sherpa. The upper limit of $\Delta a_\Gamma \approx 0.067$ was derived from the requirement that a gradient slope of 0.2 per pixel can be constrained at 3σ significance. This corresponds to an assumed total change of the photon index of 0.6 across the remnant which is in agreement with the variations that Doroshenko et al. (2017) found for their spectral analysis of bright knots (see their Fig. 4). The right panel of Fig. 35 combines the results of the previous two plots to display the gradient slope uncertainty as a function of the exposure of the simulated spectra. According to this, for the case of bright pixels, it is possible to constrain a change in the photon index of 0.2 per pixel at 3σ significance already for an exposure on the order of 10-20 ks. For the dim pixels, on the other hand, the simulations indicate that a larger exposure on the order of 70 ks would be needed to achieve a similarly significant result. The actually required exposure is expected to lie somewhere in between the result for the bright and dim pixel. The fact that a Γ gradient at 3σ significance was already found with the current eRASS:4 data in Sect. 4.2.4 which has a total exposure of ~ 2 ks is due to several differences in the procedure: First, in Sect. 4.2.4, the Γ gradient was determined directly from the spectral fit without constraining the independent photon index values of all source pixels before. N_H values were also approximated by a gradient model in this section and not constrained independently for individual pixels. This reduces the number of free parameters and therefore the statistical uncertainties, which is the reason why that approach was applied in the analysis of the eRASS:4 data.[55] As a second difference, the simulated spectra were fitted after background subtraction, while in the analysis of the eRASS:4 data in Sect. 4.2.4 and 4.2.5, the background was modelled. For background modelling, statistical errors are expected to be smaller. For simplicity and since it does not require any assump-

[54]Rescaling the exposure in this way involves the assumption that the radiation of the remnant is more or less uniform across the source area. Only under this assumption, a longer exposure is interchangeable with a larger extraction area. Since the brightness of the remnant varies, this assumption is not accurately fulfilled. However, for a rough estimate as it is aimed at in this section, the assumption is useful for simplification.

[55]Already in Sect. 4.2.5, for independent N_H values, the significance of the Γ gradient slope is below 3σ.

tions on the components of the background spectrum, background subtraction was used in the case of the simulated spectra. The goal was to get a rough estimate of the required exposure when aiming at constraining the photon index of each single pixel independently at a certain accuracy that enables to determine the direction of the variations at 3σ significance. As a result, this should be possible with an exposure between 20 and 70 ks. The advantage of this approach with respect to determining the Γ gradient directly from the spectral fit is that it can be evaluated how well the gradient relation actually fits the variations. Deviations from a linear gradient in the form of small-scale local changes can be observed which remain unnoticed when applying the gradient relation a priori in the spectral fit.

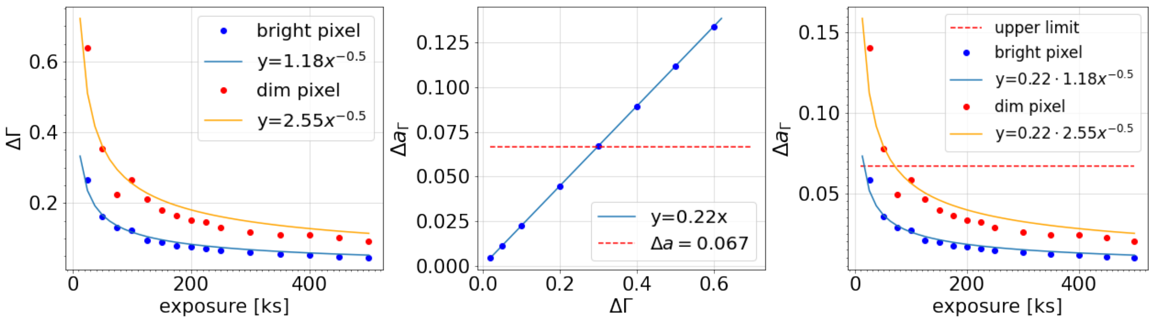

Figure 35: *Left panel:* 1σ uncertainties in the photon index of a generic sub-region (like those displayed in Fig. 20) as a function of the exposure. The red data points represent uncertainties for a faint pixel, the blue for a bright one (see Sect. 5.1 for details). *Middle panel:* Error in the Γ gradient slope as a function of the uncertainty in the photon index. The red dashed line displays the bound below which the gradient slope can be constrained at 3σ significance, assuming a change in Γ of 0.2 per pixel. *Right panel:* Error in the Γ gradient slope as a function of the exposure. In order to obtain this plot, the relation obtained from the fit in the middle panel was applied to the data in the left panel. The red dashed line represents the same upper limit on Δa_Γ as in the middle panel.

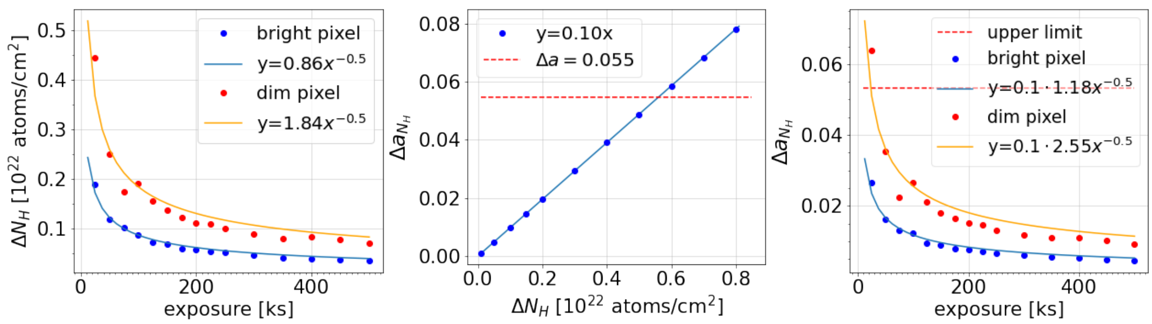

Figure 36: Same as Fig. 35, but for the gradient of the absorption column density N_H instead of the photon index Γ. The basis for the 3σ significance level was a change of $0.16 \cdot 10^{22}$ atoms/cm^2 in this case, as it was found in the analysis in Sect. 4.2.1.

Fig. 36 shows the same plots as Fig. 35, but for the gradient in the absorption column density instead of the photon index. In this case, the requirement to derive the upper limit of the slope error was to constrain a change of $0.16 \cdot 10^{22}$ atoms/cm^2 at 3σ. This was the gradient slope found in the analysis in Sect. 4.2.1. As a result of the simulations, the uncertainty in N_H for each single pixel is sufficiently small to constrain this slope in a gradient fit with the required significance for the case of bright pixels already for an exposure below 5 ks. Thus, it should be possible with the current eRASS:4 data.[56]

[56]Indeed, the significance of the N_H gradient slope in east-west direction found in Sect. 4.2.4 is above 10σ. However, as described above, the significance would be lower when applying the procedure used for the simulated spectra to the eRASS:4 data.

For the dim pixels, an exposure on the order of 30 ks is expected to be necessary. Again, the actual requirement is expected to lie somewhere in between. In contrast to the photon index, where no fit of sub-regions with independent values was conducted, in the case of N_H, it is also possible to compare the uncertainties on the independent N_H values obtained in Sect. 4.2.2 to those from the simulations. The values from the actual analysis are clearly smaller than those estimated by the simulations, which is not so much surprising, given that the fitting approach applied to the simulations is more conservative. As already mentioned in the paragraph on the Γ gradient fit, the first and probably most important difference is that background subtraction was used in the case of the simulations. What reduces the statistical uncertainties in the real spectral analysis further with respect to the fit of the simulated spectra is the fact that the photon index was frozen or linked in the two independent N_H fits performed on the eRASS:4 data (see Sect. 4.2.2 and 4.2.5). In contrast, when fitting the simulated spectra, all parameters of the absorbed power law were variable, corresponding to the case that N_H and Γ would be constrained individually for each sub-region. These two differences, background subtraction versus modelling and restricted photon index variations in the real spectral analysis in Sect. 4.2.2, are likely reasons for the fact that the statistical uncertainties on the independent N_H values obtained from the real analysis are smaller than those estimated from the simulations for an exposure of 2 ks (see Fig. 36 left). Additionally, in the case of the gradient slopes themselves, the same argument as explained above for the Γ gradient applies as an explanation for larger errors estimated from the simulations with respect to the real analysis results: N_H is first explicitly constrained from the simulations and then the values are fitted with a 2d gradient in the case of the simulations. In the real data analysis, the gradient is a part of the spectral model.

When comparing Fig. 35 and Fig. 36, it is also evident that the uncertainties in the N_H gradient slope are smaller with respect to those in the Γ gradient slope. Reasons for that are on the one hand a smaller uncertainty in N_H from the spectral fit. On the other hand, the slope uncertainty is considerably reduced by the fact that for constraining the N_H gradient, also the background pixels can be used, which results in a grid of 6 by 6 pixels. For the Γ gradient, only the source pixels can be considered, thus a 4 by 4 grid. In theory, the pixel size could be reduced in order to achieve a larger number of steps to constrain the gradient. Practically, this would reduce the number of counts within each pixel for the same exposure and a larger exposure would be required to achieve the same photon index accuracy and therefore the same significance level of the gradient slope.

6. Summary and conclusions

The X-ray spectral data of the eRASS 1 to 4 surveys for the non-thermal supernova remnant HESS J1731-347 have been analysed in this Thesis work. The data have a total exposure of ~2 ks for each TM. An X-ray image of the source was produced (Sect. 2), showing a much fainter emission in the western part which is closer to the galactic plane. This is also visible in the image produced by Doroshenko et al. (2017) from *XMM-Newton* data of several observation campaigns between 2007 and 2015. The spectrum of the total remnant was extracted from a circle with radius 17.5′, centered on the CCO (see Sect. 3.1). An annulus with inner radius 17.5′ and outer radius 24.7′ served as background region. Point sources listed in the eRASS 1 to 4 catalogs as well as those revealed by a source detection have been removed with an exclusion radius of at least 2′ from the background region. After that, the area ratio of background to source region turned out to be ~ 90%. Within the source region, only the CCO was masked out with a radius of 40″. The total source spectrum was fitted with two different approaches: background subtraction (Sect. 3.2) and background modelling (Sect. 3.3). The background subtracted fit yielded a photon index of $\Gamma_{SNR} = 2.8 \pm 0.2$ which is compatible with that found by Doroshenko et al. (2017) ($\Gamma_{SNR} = 2.66 \pm 0.01$), while the value obtained from the simultaneous fit in Sect. 3.3 was significantly lower: $\Gamma_{SNR} = 2.2 \pm 0.1$. For both fitting approaches, background subtraction as well as background modelling, the photon index changes when choosing a different background region. For background subtraction, results for the regions tested range from $\Gamma_{SNR} = 2.5 \pm 0.2$ (right half annulus) to $\Gamma_{SNR} = 2.9 \pm 0.3$ (left half annulus). This difference is not significant. However, the values included in the 1σ confidence range are considerably different. For background modelling, the results were $\Gamma_{SNR} = 2.3^{+0.1}_{-0.2}$ for the right half annulus and $\Gamma_{SNR} = 2.2 \pm 0.1$ for the left half annulus. Thus, the results for the right half annulus agree with background subtraction within the 1σ bounds. It is evident that the photon index determined from the background modelling fit has a smaller statistical uncertainty and is also less sensitive to the selection of the background region. In general, the results obtained from the background modelling fit are expected to be more reliable due to several caveats in the background subtraction approach. One of them is that when subtracting the background radiation, there is no possibility to scale the cosmic X-ray background and the FWC background by a different factor (as explained in Sect. 3.2). Also, the background subtraction approach has no ability to account for or even raise awareness of differences in the background emission between source and background region. For these reasons, background modelling is in general the preferable approach. The only question mark in this case arises from the disagreement with the photon index result obtained by Doroshenko et al. (2017). In the view of the poor counting statistics, it is difficult to make the firm statement that the photon index of the remnant as it is seen by eROSITA is undoubtedly lower than the result found by Doroshenko et al. (2017) from *XMM-Newton* data. Additionally, there might always be some hidden systematic errors due to the complexity of background modelling. The fact that the sensitivity of eROSITA drops faster towards higher X-ray energies than that of *XMM-Newton* could also influence the photon index result of the eRASS:4 analysis and make it less reliable. On the other hand, the stray light issues complicated the analysis of Doroshenko et al. (2017) and it cannot be ruled out completely that this has affected their photon index result. Thus, at this point, it can only be summarized that with the analysis approach applied in this Thesis work, involving the selection of a background model and background region, the photon index of the total SNR found from eRASS:4 data of all 7 TMs is significantly lower than the value obtained by Doroshenko et al. (2017) for *XMM-Newton* data.

In the further analysis, the source and background area was divided into 36 sub-regions in order to trace variations of the absorption column density N_H and the photon index Γ_{SNR} across the remnant (Sect. 4). The regions were chosen to be squares of equal size and were defined such that the source region is covered by a 4 by 4 grid, surrounded by one row of background pixels at the top, bottom, left and right, respectively. This leads to 6 by 6 pixels in total. The width of one pixel is $35'/4 = 8.75'$.

Six sub-regions were removed from the analysis due to contamination. The radius for point source removal was reduced to 40″ for sources with less than 100 counts in order to limit the area reduction of the pixels due to point source removal. This radius is still expected to include > 95% of the emitted energy (see Sect. 3.1) and the contaminating sources are faint enough that the eventually remaining 5% can be expected not to have a notable impact. The spectra of all regions were fitted simultaneously. In the view of the limited counting statistics, linking relations were introduced for both N_H and Γ_{SNR} between the sub-regions and fit results were compared for various combinations of N_H and Γ variation models. Linking N_H by a 2-dimensional gradient (according to Eq. 7) while $\Gamma_{SNR} = 2.66$ was frozen to the result of Doroshenko et al. (2017) yielded a positive N_H gradient slope in east-west direction (Sect. 4.2.1). The direction of increasing absorption is in agreement with the results of Doroshenko et al. (2017) who also found higher N_H values for sub-regions in the western part (see Fig. 32 right). The pattern of independent N_H results (Sect. 4.2.2) for a frozen, constant photon index shows some deviations from the 2d linear gradient model, for instance it also varies in south-north direction. Differences are in the range of about $\pm 5\sigma$ based on the uncertainties of the independent N_H values (Sect. 4.2.3). These differences lead to different directions in the Γ_{SNR} gradient for the two N_H patterns: When both N_H and Γ are linked by a 2d linear gradient, spectra appear harder towards the north-west of the remnant, i. e. there is a non-zero component of the Γ_{SNR} gradient in south-north direction perpendicular to the N_H gradient (Sect. 4.2.4). However, this component vanishes when N_H values are allowed to vary independently between regions (Sect. 4.2.5). Therefore, the Γ gradient slope in south-north direction can be considered an artifact arising from the underestimation of N_H in the gradient model for some northern regions. Due to the correlation of the absorption and the photon index, this leads to artificially harder spectra in northern direction. Thus, the final result of the spatially resolved spectral analysis is that the absorption tends to increase in western direction, while also showing variations in north-south direction. Changes of the photon index seem to be oriented only in east-west direction, with harder spectra in the western part of the remnant. Therefore, the spectrum of the remnant appears harder towards the region where a molecular cloud is likely to be present in its vicinity according to the X-ray absorption as well as ^{12}CO absorption and brightness temperature diagrams of H. E. S. S. Collaboration et al. (2011), see Fig. 22. The direction in which the spectra seem to harden is surprising, considering the fact that the shock expansion velocity is reduced in the case of an interaction with denser surroundings. So, in this picture, if there is and interaction taking place between the remnant and the molecular cloud, it is expected to lead to a smaller maximum energy particles can gain through diffusive shock acceleration and therefore softer rather than harder X-ray synchrotron spectra. Cassam-Chenai et al. (2004) found in their X-ray spectral analysis of the SNR RX J1713.7-3946 indeed softer spectra in sub-regions with stronger absorption. Additionally, their analysis revealed that stronger absorbed regions appear brighter in X-rays for RX J1713.7-3946, which can almost certainly be ruled out for HESS J1731-347 based on the results of this Thesis work and previous studies. From the two contrary findings of Cassam-Chenai et al. (2004) with respect to the analysis in this Thesis follows also one common result: Spectra appear harder for X-ray dimmer regions of the respective SNR, which, however, are stronger absorbed for HESS J1731-347 and less absorbed for RX J1713.7-3946 with respect to the brighter regions.[57]

Due to the limited counting statistics of the eRASS:4 observations, it is not meaningful to perform a fit with independent N_H and independent Γ_{SNR} in order to analyse the behaviour of Γ_{SNR} in greater detail. The fit with independent N_H and linked Γ_{SNR} is pretty much the end of the flagpole in constraining photon index variations. This can be seen on the one hand from the fact that the reduced fit statistics value does not decrease with respect to the N_H linked, Γ linked fit. On the other hand, uncertainties in the Γ_{SNR} values calculated from the gradient relation are so high for independent N_H values that variations over the pixel rows are hardly significant (see Fig. 30 right). Despite the statistical limitations, the analysis yielded a photon index gradient slope which is significant at 2.5σ and which indicates that spectra seem to harden towards the western part of the remnant. Overplotting

[57] Since the two studies deal with different SNRs, there is of course the possibility that the observed phenomena are caused by deviating properties of the two objects and their surroundings.

spectra of sub-rgions in the western and eastern part shows a different decrease in the count rate for stronger absorbed regions in different energy ranges (see Fig. 31). There is the chance that the photon index gradient is artificial even for independent N_H values. The stronger count rate decrease in a certain energy range below $\sim 1 - 1.5$ keV might be mainly absorption-related and if the fitted absorptions in the model for some reason do not (fully) account for it, this might cause an artificial hardening of the spectra since photon index and absorption are correlated. Additionally, judging from the reduced statistics value, the spectra are not considerably better represented by a model including photon index variations than by one with a constant photon index. This is a general caveat of the photon index variation results for the current data since the model is more complex than the data require it to be. Therefore, parameters are expected to be not very well constrained and artificial variations might be present. If the hardening of the spectra is indeed an intrinsic effect of the source, the physical processes leading to this phenomenon are not understood in the simple picture of slowing-down of the shock expansion through interactions with a molecular cloud. From this, one would expect a contrary behaviour, as discussed in Sect. 4.2.4 and 4.2.5.

As already indicated above, one caveat of the analysis is that due to the correlation of absorption and photon index, it cannot be ruled out that the photon index variations are artificial. For higher counting statistics, it is expected to be easier to disentangle the variations of the two parameters since the spectral shape is better constrained. Additionally, with the current data, assuming that there are indeed photon index variations, the question how well they can be represented by a 2d linear gradient model cannot be addressed. This is also because of the low counting statistics that do not allow a fit with independent absorption as well as independent photon index values (see above).[58] In order to get a more detailed and reliable insight into photon index variations, eROSITA observations of the remnant with a longer exposure would be instructive. With the aim of assessing the exposure required for a meaningful result, such spectra have been simulated as the last part of the analysis (Sect. 5). The simulations indicate that, under the assumptions made, an exposure between 20 ks and 70 ks would enable a sufficiently accurate constraining of the sub-region photon indices in order to get a 3σ significant slope of a gradient fitted to the photon index values. Thanks to the good stray light protection, studying photon index variations across the remnant with eROSITA seems promising. In general, it would of course be very beneficial for further exploring the X-ray Universe if the operations of this powerful instrument could be resumed. For larger supernova remnants like RX J1713.7-3946, the counting statistics of eRASS 1 to 4 might be already sufficient to get more detailed insights into Γ variations than in the case of HESS J1731-347. This could be interesting to explore for remnants that were not yet targets of extensive pointed X-ray observations.

[58] Since the analysis indicates clear deviations for N_H between independent values and the gradient model, it would not be instructive to restrict the variations of N_H to reduce the number of free parameters and search for independent Γ variations. This would be expected to induce artificial effects due to the correlation of the parameters.

Acknowledgements
I would like to thank Prof. Andrea Santangelo for the possibility to work in his group, which I highly appreciated. Further, this Thesis work would not have been possible without the supervision of Dr. Gerd Pühlhofer and Dr. Victor Doroshenko. I want to express my thanks to them for giving me many possibilities to extend my knowledge and skills through their instructive feedback and explanations, interesting discussions and helpful answers to my questions. I also thank them for the proofreading of my Thesis. I appreciated the discussions with Miltos Michailidis and Nhan Nguyen about general aspects of spectral extraction and analysis.
I am grateful to the IAAT community for several common activities as well as interesting lunch and coffee break conversations.
Last but not least, I want to thank my family and friends for their support.

References

Acero, F., Pühlhofer, G., Klochkov, D., Komin, N., Gallant, Y., Horns, D., and Santangelo, A. (2009). X- and gamma-ray studies of HESS J1731-347 coincident with a newly discovered SNR. *arXiv e-prints*, page arXiv:0907.0642.

Aharonian, F., Akhperjanian, A. G., Barres de Almeida, U., Bazer-Bachi, A. R., Behera, B., Beilicke, M., Benbow, W., Bernlöhr, K., Boisson, C., Bolz, O., Borrel, V., Braun, I., Brion, E., Brown, A. M., Bühler, R., Bulik, T., Büsching, I., Boutelier, T., Carrigan, S., Chadwick, P. M., Chounet, L. M., Clapson, A. C., Coignet, G., Cornils, R., Costamante, L., Dalton, M., Degrange, B., Dickinson, H. J., Djannati-Ataï, A., Domainko, W., Drury, L. O., Dubois, F., Dubus, G., Dyks, J., Egberts, K., Emmanoulopoulos, D., Espigat, P., Farnier, C., Feinstein, F., Fiasson, A., Förster, A., Fontaine, G., Funk, S., Füßling, M., Gallant, Y. A., Giebels, B., Glicenstein, J. F., Glück, B., Goret, P., Hadjichristidis, C., Hauser, D., Hauser, M., Heinzelmann, G., Henri, G., Hermann, G., Hinton, J. A., Hoffmann, A., Hofmann, W., Holleran, M., Hoppe, S., Horns, D., Jacholkowska, A., de Jager, O. C., Jung, I., Katarzyński, K., Kendziorra, E., Kerschhaggl, M., Khélifi, B., Keogh, D., Komin, N., Kosack, K., Lamanna, G., Latham, I. J., Lemière, A., Lemoine-Goumard, M., Lenain, J. P., Lohse, T., Martin, J. M., Martineau-Huynh, O., Marcowith, A., Masterson, C., Maurin, D., Maurin, G., McComb, T. J. L., Moderski, R., Moulin, E., de Naurois, M., Nedbal, D., Nolan, S. J., Ohm, S., Olive, J. P., de Oña Wilhelmi, E., Orford, K. J., Osborne, J. L., Ostrowski, M., Panter, M., Pedaletti, G., Pelletier, G., Petrucci, P. O., Pita, S., Pühlhofer, G., Punch, M., Ranchon, S., Raubenheimer, B. C., Raue, M., Rayner, S. M., Renaud, M., Ripken, J., Rob, L., Rolland, L., Rosier-Lees, S., Rowell, G., Rudak, B., Ruppel, J., Sahakian, V., Santangelo, A., Schlickeiser, R., Schöck, F., Schröder, R., Schwanke, U., Schwarzburg, S., Schwemmer, S., Shalchi, A., Sol, H., Spangler, D., Stawarz, Ł., Steenkamp, R., Stegmann, C., Superina, G., Tam, P. H., Tavernet, J. P., Terrier, R., van Eldik, C., Vasileiadis, G., Venter, C., Vialle, J. P., Vincent, P., Vivier, M., Völk, H. J., Volpe, F., Wagner, S. J., Ward, M., Zdziarski, A. A., and Zech, A. (2008). HESS very-high-energy gamma-ray sources without identified counterparts. , 477(1):353–363.

Anders, E. and Ebihara, M. (1982). Solar-system abundances of the elements. , 46(11):2363–2380.

Bailer-Jones, C. A. L., Rybizki, J., Fouesneau, M., Demleitner, M., and Andrae, R. (2021). Estimating Distances from Parallaxes. V. Geometric and Photogeometric Distances to 1.47 Billion Stars in Gaia Early Data Release 3. , 161(3):147.

Bamba, A., Pühlhofer, G., Acero, F., Klochkov, D., Tian, W., Yamazaki, R., Li, Z., Horns, D., Kosack, K., and Komin, N. (2012). Suzaku Observations of the Non-thermal Supernova Remnant HESS J1731-347. , 756(2):149.

Bell, A. R., Schure, K. M., Reville, B., and Giacinti, G. (2013). Cosmic-ray acceleration and escape from supernova remnants. *Monthly Notices of the Royal Astronomical Society*, 431(1):415–429.

Berezhko, E. G. and Völk, H. J. (2008). Hadronic versus leptonic origin of the gamma-ray emission from supernova remnant RX J1713.7-3946. , 492(3):695–701.

Cappelluti, N., Li, Y., Ricarte, A., Agarwal, B., Allevato, V., Tasnim Ananna, T., Ajello, M., Civano, F., Comastri, A., Elvis, M., Finoguenov, A., Gilli, R., Hasinger, G., Marchesi, S., Natarajan, P., Pacucci, F., Treister, E., and Urry, C. M. (2017). The Chandra COSMOS Legacy Survey: Energy Spectrum of the Cosmic X-Ray Background and Constraints on Undetected Populations. , 837(1):19.

Cash, W. (1979). Parameter estimation in astronomy through application of the likelihood ratio. , 228:939–947.

Cassam-Chenai, G., Decourchelle, A., Ballet, J., Sauvageot, J. L., Dubner, G., and Giacani, E. (2004). XMM-Newton observations of the supernova remnant RX J1713.7-3946 and its central source. , 427:199–216.

Cioffi, D. F., McKee, C. F., and Bertschinger, E. (1988). Dynamics of Radiative Supernova Remnants. , 334:252.

Cui, Y., Pühlhofer, G., and Santangelo, A. (2016). A young supernova remnant illuminating nearby molecular clouds with cosmic rays. , 591:A68.

Cui, Y., Yang, R., He, X., Tam, P. H. T., and Pühlhofer, G. (2019). Is the SNR HESS J1731-347 Colliding with Molecular Clouds? , 887(1):47.

Dame, T. M., Hartmann, D., and Thaddeus, P. (2001). The Milky Way in Molecular Clouds: A New Complete CO Survey. , 547(2):792–813.

Doroshenko, V., Pühlhofer, G., Bamba, A., Acero, F., Tian, W. W., Klochkov, D., and Santangelo, A. (2017). XMM-Newton observations of the non-thermal supernova remnant HESS J1731-347 (G353.6-0.7). , 608:A23.

Doroshenko, V., Pühlhofer, G., Kavanagh, P., Santangelo, A., Suleimanov, V., and Klochkov, D. (2016). Evidence for a binary origin of a central compact object. , 458(3):2565–2572.

Doroshenko, V., Suleimanov, V., Pühlhofer, G., and Santangelo, A. (2022). A strangely light neutron star within a supernova remnant. *Nature Astronomy*.

H. E. S. S. Collaboration, Abramowski, A., Acero, F., Aharonian, F., Akhperjanian, A. G., Anton, G., Balzer, A., Barnacka, A., Barres de Almeida, U., Becherini, Y., Becker, J., Behera, B., Bernlöhr, K., Bochow, A., Boisson, C., Bolmont, J., Bordas, P., Brucker, J., Brun, F., Brun, P., Bulik, T., Büsching, I., Carrigan, S., Casanova, S., Cerruti, M., Chadwick, P. M., Charbonnier, A., Chaves, R. C. G., Cheesebrough, A., Chounet, L. M., Clapson, A. C., Coignet, G., Cologna, G., Conrad, J., Dalton, M., Daniel, M. K., Davids, I. D., Degrange, B., Deil, C., Dickinson, H. J., Djannati-Ataï, A., Domainko, W., Drury, L. O., Dubois, F., Dubus, G., Dutson, K., Dyks, J., Dyrda, M., Egberts, K., Eger, P., Espigat, P., Fallon, L., Farnier, C., Fegan, S., Feinstein, F., Fernandes, M. V., Fiasson, A., Fontaine, G., Förster, A., Füßling, M., Gallant, Y. A., Gast, H., Gérard, L., Gerbig, D., Giebels, B., Glicenstein, J. F., Glück, B., Goret, P., Göring, D., Häffner, S., Hague, J. D., Hampf, D., Hauser, M., Heinz, S., Heinzelmann, G., Henri, G., Hermann, G., Hinton, J. A., Hoffmann, A., Hofmann, W., Hofverberg, P., Holler, M., Horns, D., Jacholkowska, A., de Jager, O. C., Jahn, C., Jamrozy, M., Jung, I., Kastendieck, M. A., Katarzyński, K., Katz, U., Kaufmann, S., Keogh, D., Khangulyan, D., Khélifi, B., Klochkov, D., Kluźniak, W., Kneiske, T., Komin, N., Kosack, K., Kossakowski, R., Laffon, H., Lamanna, G., Lennarz, D., Lohse, T., Lopatin, A., Lu, C. C., Marandon, V., Marcowith, A., Masbou, J., Maurin, D., Maxted, N., McComb, T. J. L., Medina, M. C., Méhault, J., Moderski, R., Moulin, E., Naumann, C. L., Naumann-Godo, M., de Naurois, M., Nedbal, D., Nekrassov, D., Nguyen, N., Nicholas, B., Niemiec, J., Nolan, S. J., Ohm, S., de Oña Wilhelmi, D., Opitz, B., Ostrowski, M., Oya, I., Panter, M., Paz Arribas, M., Pedaletti, G., Pelletier, G., Petrucci, P. O., Pita, S., Pühlhofer, G., Punch, M., Quirrenbach, A., Raue, M., Rayner, S. M., Reimer, A., Reimer, O., Renaud, M., de los Reyes, R., Rieger, F., Ripken, J., Rob, L., Rosier-Lees, S., Rowell, G., Rudak, B., Rulten, C. B., Ruppel, J., Ryde, F., Sahakian, V., Santangelo, A., Schlickeiser, R., Schöck, F. M., Schulz, A., Schwanke, U., Schwarzburg, S., Schwemmer, S., Sikora, M., Skilton, J. L., Sol, H., Spengler, G., Stawarz, Ł., Steenkamp, R., Stegmann, C., Stinzing, F., Stycz, K., Sushch, I., Szostek, A., Tavernet, J. P., Terrier, R., Tluczykont, M., Valerius, K., van Eldik, C., Vasileiadis, G., Venter, C., Vialle, J. P., Viana, A., Vincent, P., Völk, H. J., Volpe, F., Vorobiov, S., Vorster, M., Wagner, S. J., Ward, M., White, R., Wierzcholska, A., Zacharias, M., Zajczyk, A., Zdziarski, A. A., Zech, A., and Zechlin, H. S. (2011). A new SNR with TeV shell-type morphology: HESS J1731-347. , 531:A81.

Halpern, J. P. and Gotthelf, E. V. (2010). Two Magnetar Candidates in HESS Supernova Remnants. , 710(2):941–947.

Hou, L. G., Han, J. L., and Shi, W. B. (2009). The spiral structure of our Milky Way Galaxy. , 499(2):473–482.

Janka, H. T., Langanke, K., Marek, A., Martínez-Pinedo, G., and Müller, B. (2007). Theory of core-collapse supernovae. , 442(1-6):38–74.

Kirn, T. (2022). The AMS-100 experiment: The next generation magnetic spectrometer in space. *Nuclear Instruments and Methods in Physics Research A*, 1040:167215.

Klochkov, D., Pühlhofer, G., Suleimanov, V., Simon, S., Werner, K., and Santangelo, A. (2013). A non-pulsating neutron star in the supernova remnant HESS J1731-347/G353.6-0.7 with a carbon atmosphere. , 556:A41.

Klochkov, D., Suleimanov, V., Pühlhofer, G., Yakovlev, D. G., Santangelo, A., and Werner, K. (2015). The neutron star in HESS J1731-347: Central compact objects as laboratories to study the equation of state of superdense matter. , 573:A53.

Lagarias, J., Reeds, J., Wright, M., and Wright, P. (1998). Convergence properties of the nelder–mead simplex method in low dimensions. *SIAM Journal on Optimization*, 9:112–147.

Landstorfer, A., Doroshenko, V., and Pühlhofer, G. (2022). Dust scattering halo around the CCO in HESS J1731-347: A detailed analysis. , 659:A82.

Levenberg, K. (1944). A method for the solution of certain non-linear problems in least squares. *Quart. Appl. Math.*, (2):164–168.

Marquardt, D. W. (1963). An algorithm for least-squares estimation of nonlinear parameters. *Journal of the Society for Industrial and Applied Mathematics*, 11(2):431–441.

Maxted, N., Burton, M., Braiding, C., Rowell, G., Sano, H., Voisin, F., Capasso, M., Pühlhofer, G., and Fukui, Y. (2018a). Probing the local environment of the supernova remnant HESS J1731-347 with CO and CS observations. , 474(1):662–676.

Maxted, N., Burton, M., Braiding, C., Rowell, G., Sano, H., Voisin, F., Capasso, M., Pühlhofer, G., and Fukui, Y. (2018b). Probing the local environment of the supernova remnant HESS J1731-347 with CO and CS observations. , 474(1):662–676.

Milne, D. K., Goss, W. M., Haynes, R. F., Wellington, K. J., Caswell, J. L., and Skellern, D. J. (1979). Three unusual supernova remnants. , 188:437–444.

Moré, J. J. (1978). The levenberg-marquardt algorithm: Implementation and theory. In Watson, G. A., editor, *Numerical Analysis*, pages 105–116, Berlin, Heidelberg. Springer Berlin Heidelberg.

Nelder, J. A. and Mead, R. (1965). A Simplex Method for Function Minimization. *The Computer Journal*, 7(4):308–313.

Pavlinsky, M., Levin, V., Akimov, V., Krivchenko, A., Rotin, A., Kuznetsova, M., Lapshov, I., Tkachenko, A., Krivonos, R., Semena, N., Buntov, M., Glushenko, A., Arefiev, V., Yaskovich, A., Grebenev, S., Sazonov, S., Lutovinov, A., Molkov, S., Serbinov, D., Kudelin, M., Drozdova, T., Voronkov, S., Sunyaev, R., Churazov, E., Gilfanov, M., Ramsey, B., O'Dell, S. L., Kolodziejczak, J., Zavlin, V., and Swartz, D. (2018). ART-XC / SRG overview. In den Herder, J.-W. A., Nikzad, S., and Nakazawa, K., editors, *Space Telescopes and Instrumentation 2018: Ultraviolet to Gamma Ray*, volume 10699 of *Society of Photo-Optical Instrumentation Engineers (SPIE) Conference Series*, page 106991Y.

Predehl, P., Andritschke, R., Arefiev, V., Babyshkin, V., Batanov, O., Becker, W., Böhringer, H., Bogomolov, A., Boller, T., Borm, K., Bornemann, W., Bräuninger, H., Brüggen, M., Brunner, H., Brusa, M., Bulbul, E., Buntov, M., Burwitz, V., Burkert, W., Clerc, N., Churazov, E., Coutinho, D., Dauser, T., Dennerl, K., Doroshenko, V., Eder, J., Emberger, V., Eraerds, T., Finoguenov, A., Freyberg, M., Friedrich, P., Friedrich, S., Fürmetz, M., Georgakakis, A., Gilfanov, M., Granato, S., Grossberger, C., Gueguen, A., Gureev, P., Haberl, F., Hälker, O., Hartner, G., Hasinger, G., Huber, H., Ji, L., Kienlin, A. v., Kink, W., Korotkov, F., Kreykenbohm, I., Lamer, G., Lomakin, I., Lapshov, I., Liu, T., Maitra, C., Meidinger, N., Menz, B., Merloni, A., Mernik, T., Mican, B., Mohr, J., Müller, S., Nandra, K., Nazarov, V., Pacaud, F., Pavlinsky, M., Perinati, E., Pfeffermann, E., Pietschner, D., Ramos-Ceja, M. E., Rau, A., Reiffers, J., Reiprich, T. H., Robrade, J., Salvato, M., Sanders, J., Santangelo, A., Sasaki, M., Scheuerle, H., Schmid, C., Schmitt, J., Schwope, A., Shirshakov, A., Steinmetz, M., Stewart, I., Strüder, L., Sunyaev, R., Tenzer, C., Tiedemann, L., Trümper, J., Voron, V., Weber, P., Wilms, J., and Yaroshenko, V. (2021). The eROSITA X-ray telescope on SRG. , 647:A1.

Revnivtsev, M. (2003). Distribution of the Galactic bulge emission at |b|>2^o according to the RXTE Galactic Center scans. , 410:865–870.

Rho, J. and Petre, R. (1998). Mixed-Morphology Supernova Remnants. , 503(2):L167–L170.

Smith, R. K., Brickhouse, N. S., Liedahl, D. A., and Raymond, J. C. (2001). Collisional Plasma Models with APEC/APED: Emission-Line Diagnostics of Hydrogen-like and Helium-like Ions. , 556(2):L91–L95.

Takahashi, T., Tanaka, T., Uchiyama, Y., Hiraga, J. S., Nakazawa, K., Watanabe, S., Bamba, A., Hughes, J. P., Katagiri, H., Kataoka, J., Kokubun, M., Koyama, K., Mori, K., Petre, R., Takahashi, H., and Tsuboi, Y. (2008). Measuring the Broad-Band X-Ray Spectrum from 400eV to 40keV in the Southwest Part of the Supernova Remnant RXJ1713.7-3946. , 60:S131.

The H. E. S. S. Collaboration (2007). H.E.S.S. ICRC 2007 contributions. *arXiv e-prints*, page arXiv:0710.4057.

Tian, W. W., Leahy, D. A., Haverkorn, M., and Jiang, B. (2008). Discovery of the Radio and X-Ray Counterpart of TeV γ-Ray Source HESS J1731-347. , 679(2):L85.

Tian, W. W., Li, Z., Leahy, D. A., Yang, J., Yang, X. J., Yamazaki, R., and Lu, D. (2010). X-Ray Emission from HESS J1731-347/SNR G353.6-0.7 and Central Compact Source XMMS J173203-344518. , 712(2):790–796.

Truelove, J. K. and McKee, C. F. (1999). Evolution of Nonradiative Supernova Remnants. , 120(2):299–326.

Truemper, J. (1982). The ROSAT mission. *Advances in Space Research*, 2(4):241–249.

Vink, J. (2012). Supernova remnants: the X-ray perspective. , 20:49.

Wakely, S. P. and Horan, D. (2008). TeVCat: An online catalog for Very High Energy Gamma-Ray Astronomy. In *International Cosmic Ray Conference*, volume 3 of *International Cosmic Ray Conference*, pages 1341–1344.

Wang, J. and Fischer, D. A. (2015). Revealing a Universal Planet-Metallicity Correlation for Planets of Different Sizes Around Solar-type Stars. , 149(1):14.

Wilms, J., Allen, A., and McCray, R. (2000). On the Absorption of X-Rays in the Interstellar Medium. , 542(2):914–924.

Woltjer, L. (1972). Supernova Remnants. , 10:129.

A. Comparison of total remnant spectral fit for different instrumental backgrounds

Table A1: Best-fitting source model parameters when using the updated TM1 FWC model to represent the instrumental background of all TMs (left column) and for the appropriate FWC model for each TM (right column).

parameter	all new TM1	appropriate FWC model
nh_src.nH	$1.45^{+0.05}_{-0.03}$	$1.42^{+0.07}_{-0.04}$
pl_snr.norm	$0.023^{+0.002}_{-0.002}$	$0.023^{+0.004}_{-0.002}$
pl_snr.PhoIndex	$2.12^{+0.13}_{-0.09}$	$2.10^{+0.21}_{-0.09}$
red. stat.	0.90	0.90

The instrumental background of the merged data set is approximated by the TM1 FWC model (see Sect. 3.3.1). To estimate the goodness of this approximation, the spectra of the 7 TMs have been fitted each with the appropriate model and in the appropriate energy range (i. e. 0.3-8.0 keV for TM12346, 1.0-8.0 keV for TM57)[59]. All source and background spectra have been fitted simultaneously with the following models:

$$\text{bkg\_model[i]} = \text{cosmic\_bkg\_scale} \cdot (\text{apec\_kt01} + \text{nh\_bkg(apec\_kt03} + \text{pl146}))+ \\ \text{fwc\_scale\_bkg} \cdot \text{fwc\_model[i]}$$

for the background annulus spectrum, where i stands for the number of the TM, and

$$\text{src\_model[i]} = \text{nh\_src} \cdot \text{pl\_snr}+\text{cosmic\_bkg\_scale\_srcreg} \cdot (\text{apec\_kt01} + \text{nh\_src}\cdot \\ \cdot(\text{apec\_kt03} + \text{pl146}))+\text{fwc\_scale\_src} \cdot \text{fwc\_model[i]}$$

for the source region spectrum. The parameters of the cosmic X-ray background model were frozen to the results found in Sect. 3.3 for Γ_{SNR} thawed. The reason to do so was to avoid repeating the iterative procedure in which these parameters were found for the separated spectra of all 7 TMs. To account for a different normalization of the spectrum when considering only single TMs, separate constant scaling factors have been introduced for the instrumental background in the source region and in the background region as well as for the cosmic X-ray background in both extraction regions. The model involves the assumption that these scaling factors are the same for all TMs, i. e. that their contribution to the merged spectrum is equal.
The best-fitting source and background models for the fit of all TM spectra with separate models are plotted in Fig. A1 and compared to the ones obtained when the updated version of the TM1 FWC model is used for each TM. The fit with the TM1 model was carried out in the 0.3-8.0 keV energy range for all TMs. For TM5 and 7, the fit of the appropriate TM models was only carried out in the energy range of 1.0-8.0 keV (hence the strong deviation of the TM5 model in the low-energy regime).

[59] The FWC models are valid up to 10.0 keV. However, the remnant spectrum is dominated by noise above ~ 8.0 keV. Therefore, the energy range has been restricted for the fit.

Especially in the TM7 fit, the model underestimates the observed counts below ~ 0.5 keV. Using the appropriate TM7 FWC model instead of TM1 does not considerably improve this issue. Even when the energy range is extended to 0.3-8.0 keV (the respective plot is not shown here), the model is still too low at the low energy end. Hence, the TM7 spectrum cannot be represented properly at the low-energy end by the model fitting at least TM12346 data reasonably well. This agrees with the official recommendation of not using the TM 7 instrumental background model (and therefore TM7 spectra) below 1 keV. For the TM5 spectrum, in the case of HESS J1731-347, using the TM1 model seems to give a good representation at the low energy end while the TM5 model shows a strong deviation upwards from the data. This phenomenon again (as for the TM7 downward deviation) persists when extending the energy range to 0.3-8.0 keV. For TM2346, the deviations from the TM1 model are hardly notable. There is also a small deviation for TM1. The reason for that is the use of the old TM1 model in the separate TM model fit (blue) and of the new one in the all-TM1 fit (red, see Sect. 3.3.1 for an overview of the available FWC models). There are slight differences in the TM1 model parameters between the two cases.

Since, as mentioned above, the cosmic X-ray background model parameters were kept frozen to the results of the simultaneous source and background region fit of the merged spectra, the meaning of the comparison is limited. The cosmic X-ray background parameters were found under the assumption that the TM1 model represents the instrumental background of the merged data set reasonably well. However, the use of the appropriate FWC models together with the set of parameters found in Sect. 3.3 allows a good-quality fit of the spectra of all TMs with models deviating only marginally from those involving the TM1 model. This result is at least an indication that the approximation is reasonable. Also, the source model parameters which were allowed to vary do not differ significantly at the 1σ level and the reduced statistics values are equal, see Table A1.

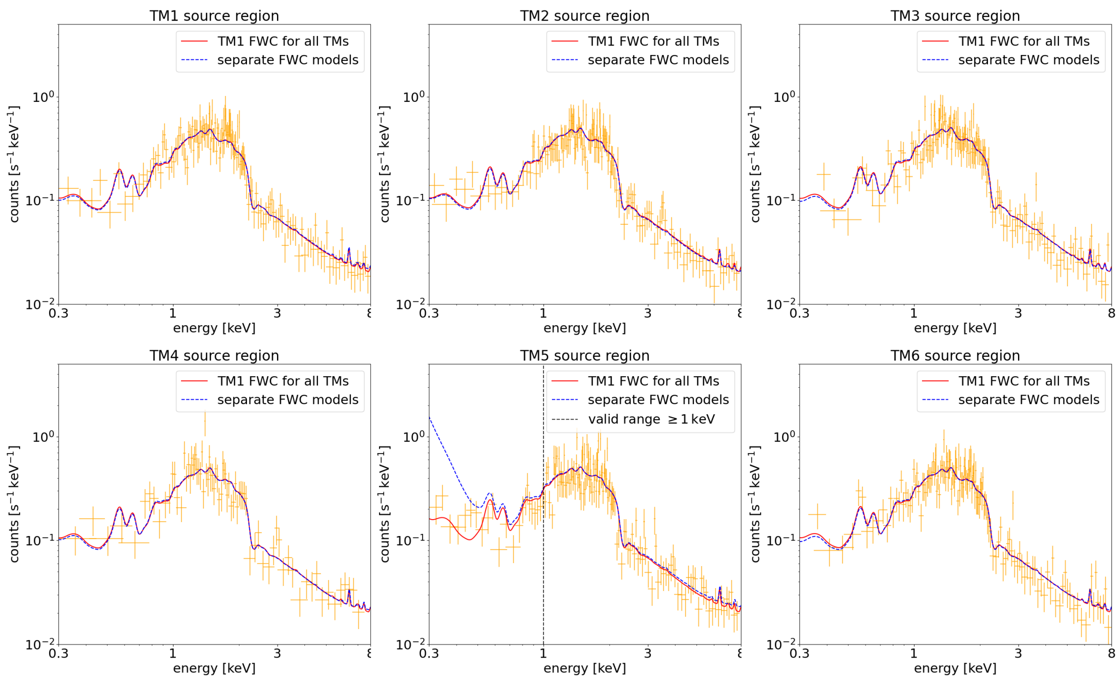

Figure A1: Figure continued on the next page.

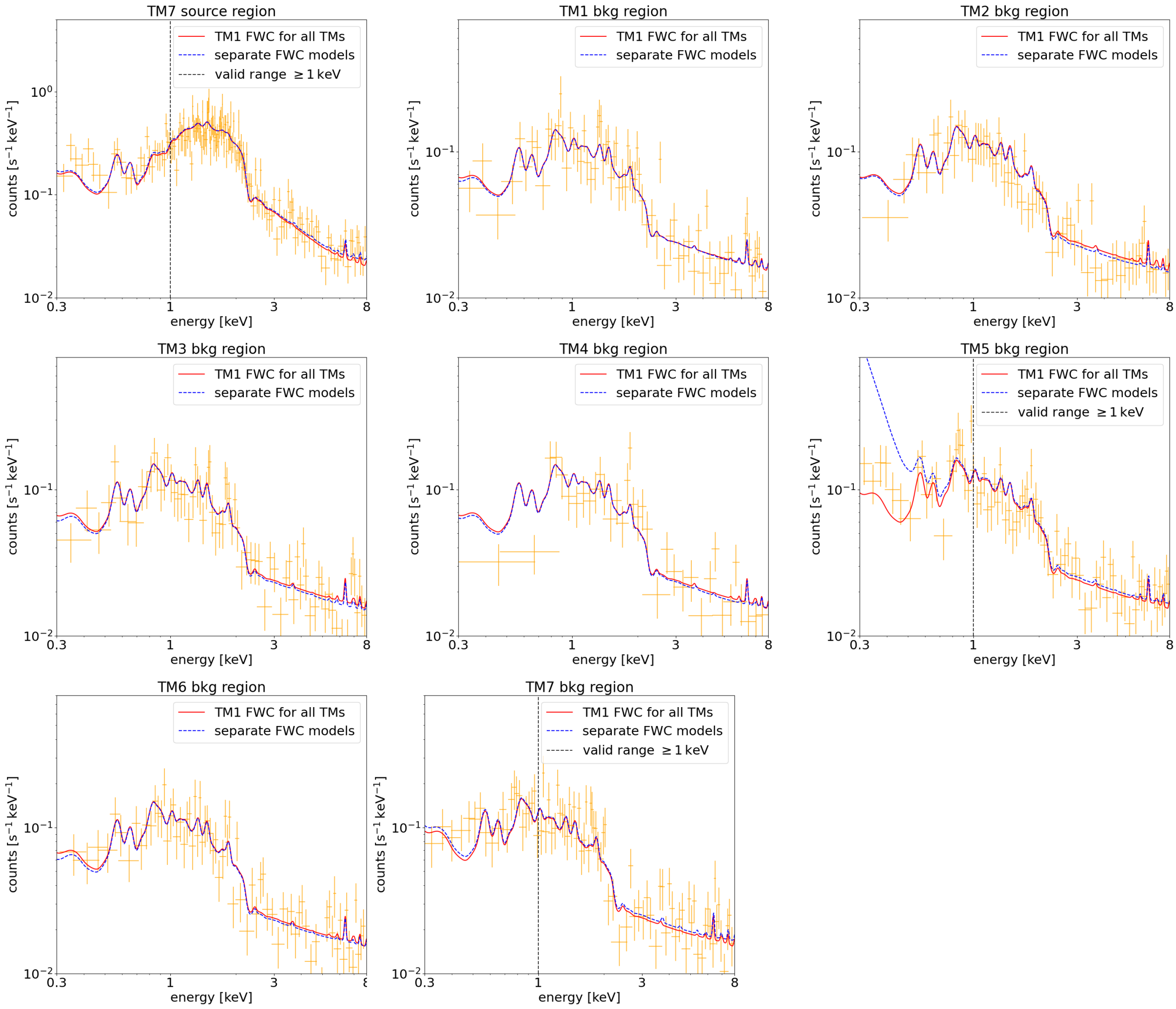

Figure A1: Plot of source and background spectra of the 7 TMs and best-fitting models when using the updated TM1 FWC model for all TMs (red) and the appropriate old (since the updated ones are not available for TM5 and 7) TM models for each TM (blue).

B. Comparison of background spectra for different extraction regions

The left panel of Figure B1 shows the background spectra for two different extraction annuli: one bordering directly on the source region which was used in the analysis, see Sect. 3, and one starting at a distance of 20′ from the CCO, i. e. with a separation of 2.5′ to the border of the source region. The spectrum of the larger annulus was renormalized using the area ratio of the two regions. The two spectra agree well for high energies. However, at the low-energy end, the spectrum of the larger annulus shows indication for a larger flux which reflects the higher background emission in the 0.3-1.8 keV band that can be seen on the bottom left of Figure 2. Even if the spectra almost agree within the error bars, all red data points except one lie below the blue for low energies. This implies a higher flux when integrating over the blue spectrum with respect to the red.

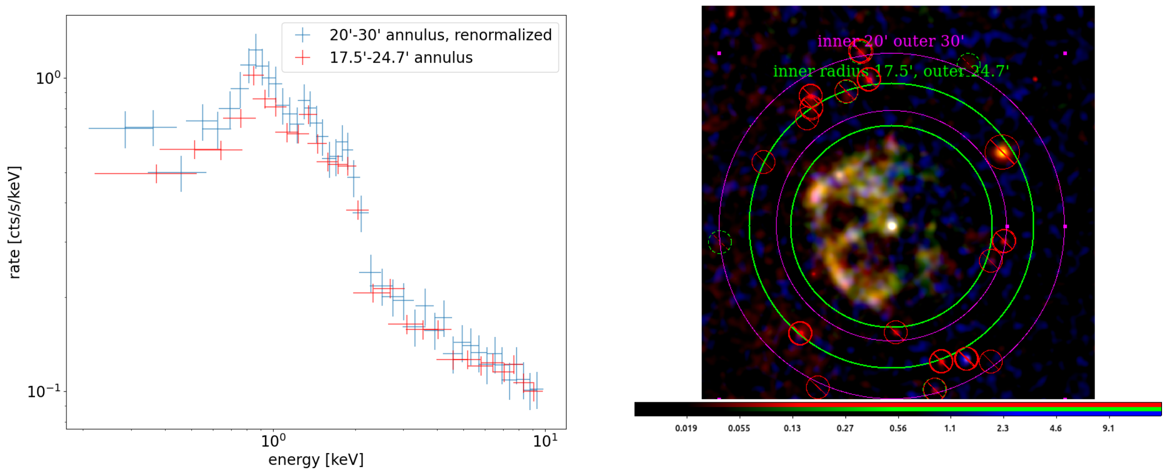

Figure B1: Left panel: Background spectra for two different annular extraction regions displayed in the right panel: a larger 20′ to 30′ annulus (blue spectrum) and a smaller 17.5′ to 24.7′ annulus (red spectrum), both centered on the CCO of HESS J1731-347. The spectra were grouped such that each bin contains at least 200 counts in order to capture the spectral shape clearly in the plot. The spectrum of the larger annulus was renormalized by multiplying the count rate by the extraction area ratio of the two regions. Error bars were not modified in the course of the normalization.

B.1. Results of background subtracted fit

Table B1: Best-fitting parameters for the background subtracted fit using two different background extraction regions (see Sect. B). The photon index Γ of the SNR emission power law is shown in the first column. The normalization of this power law is given in the second column. The third column lists the absorption column density in units of 10^{22} atoms/cm^2. The reduced fit statistics is given in the last column.

bkg annulus	Γ	norm	N_H	red. stat.
20′-30′	$3.33^{+0.27}_{-0.25}$	$0.072^{+0.019}_{-0.014}$	$2.46^{+0.19}_{-0.18}$	1.02
17.5′-24.7′	$2.77^{+0.23}_{-0.22}$	$0.045^{+0.010}_{-0.008}$	$2.00^{+0.17}_{-0.16}$	0.79

Table B1 shows the fit parameter results and reduced statistics values for the background subtracted fit using two different background annuli (see previous section). The background subtracted spectrum was fit in the energy range 0.5-4 keV with an absorbed power law using the *tbabs* absorption model as described in Sect. 3.2. The fit quality is clearly better for the smaller background annulus. Also, the results for the parameters are closer to the expectations considering the results Doroshenko et al. (2017) got from their XMM Newton data analysis of the source. A possible explanation for the differences when using the larger and smaller background annulus is that the larger one includes a bigger part of the background region where the rgb image shows a higher emission in the 0.3-1.8 keV range, see bottom left corner in Fig. B1, right panel. Since the photon index and the absorption are correlated, i. e. a spectrum with a high photon index and a high absorption can look similar as one with a lower photon index and lower absorption, by eye it is hardly possible to tell the difference between the two fits and judge which is the more appropriate one.

C. Fit results for simultaneous source and background region fit with TM12346 data only

As mentioned in Sect. 3.3 the underestimation of the source region count rate in the low-energy regime ≤ 0.5 keV is suggested to be related to the light-leak contamination in TM 5 and 7 data as these two TMs do not have an on-chip filter (Predehl et al. (2021)). Therefore, in this section, the simultaneous fit of the source and background area spectrum as it is described in Sect. 3.3 for the data of all 7 TMs is conducted for TM 12346 only. The best-fitting models for a frozen and thawed photon index of the remnant emission are shown in Fig. C1. As anticipated in Sect. 3.3.4, the underestimation of the count rate in the low-energy regime ≤ 0.5 keV is less prominent without TM 5 and 7 than when including their data (see Fig. 15).

Table C1 shows the best-fitting parameters for the fits in Fig. C1. Just as for the case of all TMs, the best fit for Γ_{SNR} frozen to 2.66 has almost the same reduced statistics value as that for a thawed photon index of the remnant emission. The quality of the fit improves slightly when excluding TM 5 and 7 data. The instrumental background scaling is significantly lower for obvious reasons when considering only 5 of the 7 TMs. However, the comparison with Table 5 reveals that there are no significant differences for the parameters of the source or cosmic X-ray background emission when TM 5 and 7 data is excluded. This indicates that the analysis results in this case are not significantly affected by eventual light leak contamination from TM 5 and 7.

Table C1: Best-fitting parameters for the simultaneous fit of the source and background region spectrum, using only the data of TM 12346 (i. e. of all TMs with an on-chip filter). Left: Γ_{SNR} is frozen to the result of Doroshenko et al. (2017). Errors correspond to the 1σ confidence bounds. Right: Γ_{SNR} is thawed. The corresponding fits are compared in Fig. C1. The results when including TM 5 and 7 data are given in Table 5.

	Γ_{SNR} = 2.66 frozen			Γ_{SNR} thawed		
parameter	value	lower error	upper error	value	lower error	upper error
pl_snr.PhoIndex	2.66	–	–	2.23	-0.13	+0.12
nh_bkg.nH	1.37	-0.10	+0.10	1.26	-0.13	+0.10
nh_src.nH	1.61	-0.05	+0.05	1.43	-0.09	+0.07
apec_kt01.kT	0.24	-0.01	+0.01	0.22	-0.01	+0.01
apec_kt03.kT	0.66	-0.04	+0.04	0.64	-0.04	+0.04
pl_snr.norm	0.037	-0.001	+0.001	0.026	-0.003	+0.003
pl146.norm	0.0026	-0.0003	+0.0003	0.0027	-0.0003	+0.0003
apec_kt01.norm	0.00074	-0.00004	+0.00004	0.00072	-0.00004	+0.00004
apec_kt03.norm	0.013	-0.003	+0.003	0.011	-0.003	+0.003
scale_bkgreg.factor	0.36	-0.01	+0.01	0.35	-0.01	+0.01
red. stat.	0.97			0.96		

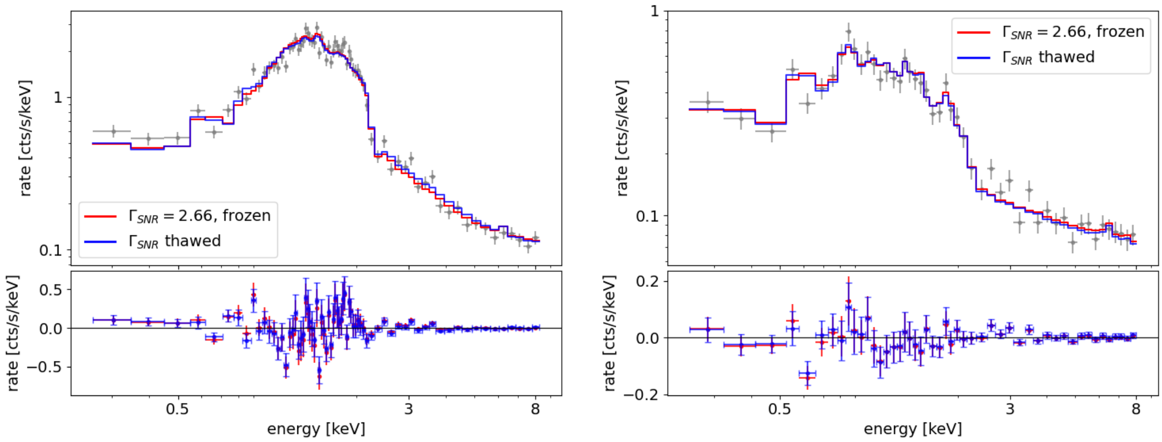

Figure C1: Source region (left) and background region (right) spectrum best-fitting models for the simultaneous fit of both data sets, using only data of TM 12346. For the red model, $\Gamma_{SNR} = 2.66$ is frozen. In the blue model, Γ_{SNR} is thawed. The best-fitting parameter values for both cases are given in Table C1. All other parameters are thawed except for the photon index of the AGN and GRXE power law ($\Gamma = 1.46$). The background spectrum is grouped to at least 70 counts per bin, the source spectrum to at least 100.

D. Background modelling fit for left and right half annulus background

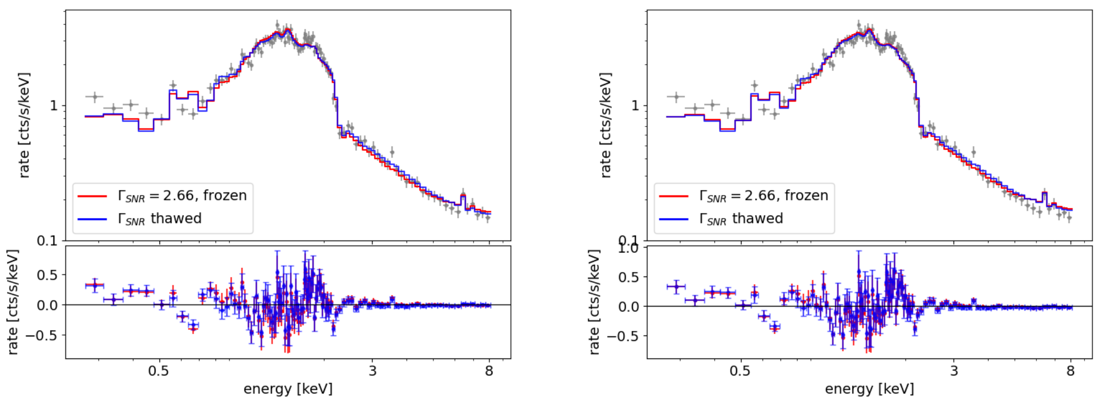

Figure D1: Best-fitting source region spectrum with frozen (red) and thawed (blue) photon index for different background regions: The left half of the background annulus is used to extract the background spectrum for the left panel fit, the right half annulus for the right panel fit. See Fig. 5 for the definition of the regions.

As mentioned in Sect. 3.3.5, the background modelling fit was also performed for background spectra extracted from different regions, namely the same as used for background subtraction in Sect. 3.2. The source and background region spectra were fitted simultaneously as described in Sect. 3.3. The best-fitting source and background models for a thawed and frozen photon index for both regions are shown in Fig. D1 and D2. Tables D1 and D2 list the corresponding numbers. For the case of a thawed Γ_{SNR}, the differences in the parameters for the two background regions are not significant at the 1σ level. The absorption is considerably higher for the right half annulus, but has also larger uncertainties. In the case of $\Gamma_{SNR} = 2.66$ frozen, the right background half annulus has a significantly higher $N_{H,\text{bkg}}$ than the left. This is what can be expected from the absorption pattern found in the spatially resolved spectral analysis (Sect. 4.1) and by Doroshenko et al. (2017). The remaining parameters agree within 1σ uncertainties also in this case. The fit is slightly better for the left half annulus, judging by the reduced fit statistics value.

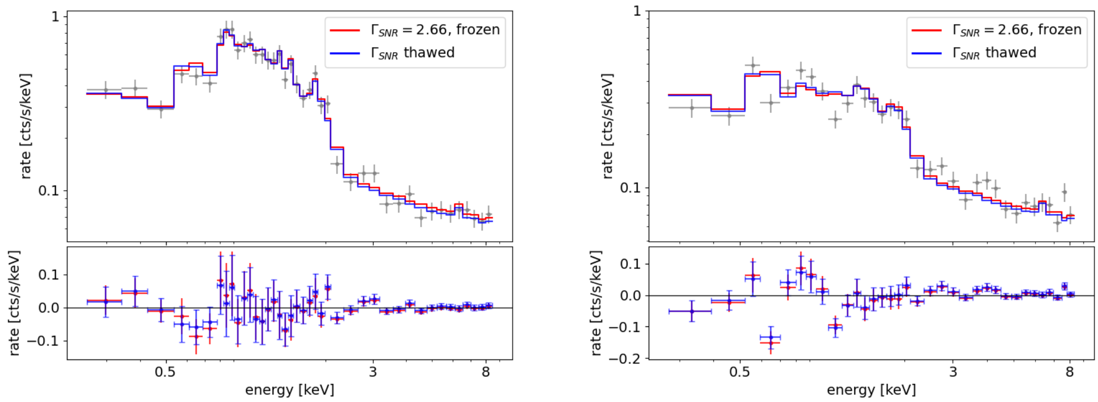

Figure D2: Best-fitting background spectrum with frozen (red) and thawed (blue) photon index for different background regions: The left half of the background annulus is used to extract the background spectrum for the left panel fit, the right half annulus for the right panel fit. See Fig. 5 for the definition of the regions.

Table D1: Best-fitting parameters of the simultaneous source and background region fit for the left half annulus background. Left columns: Γ_{SNR} is a free fit parameter. Right columns: Γ_{SNR} is frozen to the result of Doroshenko et al. (2017).

	Γ_{SNR} thawed			Γ_{SNR} frozen		
par	val	lower error	upper error	val	lower error	upper error
pl_snr.PhoIndex	2.18	-0.09	+0.10	2.66	–	–
pl_snr.norm	0.026	-0.002	+0.002	0.037	-0.001	+0.001
nh_src.nH	1.56	-0.06	+0.06	1.73	-0.05	+0.05
apec_kt01.kT	0.22	-0.01	+0.01	0.24	-0.01	+0.01
apec_kt01.norm	0.00043	-0.00002	+0.00002	0.00044	-0.00002	+0.00002
apec_kt07.kT	0.66	-0.03	+0.03	0.68	-0.03	+0.03
apec_kt07.norm	0.009	-0.002	+0.002	0.010	-0.002	+0.002
nh_bkg.nH	1.31	-0.09	+0.08	1.37	-0.08	+0.08
pl146.norm	0.0013	-0.0002	+0.0002	0.0013	-0.0002	+0.0002
scale_bkgreg.factor	0.31	-0.01	+0.01	0.32	-0.01	+0.01
red. stat.	0.92			0.94		

Fig. D3 shows the background spectra and models for the two half annuli when all model parameters except N_H are frozen to the best-fitting values of the source region only fit and rescaled accordingly. The models fit both spectra better than it is the case for the total annulus (see Fig. 12). For the left half annulus, the agreement is better than for the right around 0.8 keV and above ~ 2 keV. This could be a

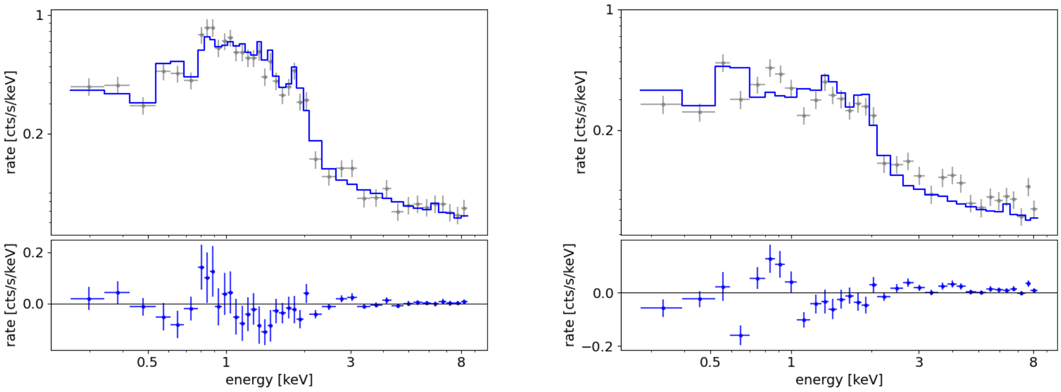

Figure D3: Background models for the left half annulus (left panel) and right half annulus (right panel) after the source region fit. Except for the absorption column density, all parameters are frozen to the best-fitting values for the source region and rescaled accordingly. The same plot for the total background annulus is shown in Fig. 12.

Table D2: Best-fitting parameters of the simultaneous source and background region fit for the right half annulus background. Left columns: Γ_{SNR} is a free fit parameter. Right columns: Γ_{SNR} is frozen to the result of Doroshenko et al. (2017).

	Γ_{SNR} thawed			Γ_{SNR} frozen		
par	val	lower error	upper error	val	lower error	upper error
pl_snr.PhoIndex	2.28	-0.15	+0.10	2.66	–	–
pl_snr.norm	0.028	-0.003	+0.003	0.037	-0.001	+0.001
nh_src.nH	1.49	-0.12	+0.08	1.66	-0.05	+0.07
apec_kt01.kT	0.23	-0.02	+0.01	0.24	-0.01	+0.01
apec_kt01.norm	0.00039	-0.00003	+0.00002	0.00040	-0.00002	+0.00002
apec_kt07.kT	0.68	-0.08	+0.05	0.70	-0.06	+0.05
apec_kt07.norm	0.005	-0.002	+0.002	0.006	-0.001	+0.002
nh_bkg.nH	1.58	-0.24	+0.16	1.74	-0.15	+0.20
pl146.norm	0.0012	-0.0002	+0.0002	0.0012	-0.0002	+0.0002
scale_bkgreg.factor	0.31	-0.01	+0.01	0.32	-0.01	+0.01
red. stat.		0.98			0.99	

hint that the shape of the background spectrum in the source region is more similar to that of the left half annulus. On the other hand, as pointed out in Sect. 3.3.5, the results of the background subtracted and background modelling fit agree within 1σ uncertainties for the right half annulus (see Table D2 below and for the background subtracted fit results Table 1). In contrast to that, the difference between the two fit results is even slightly larger than for the total background annulus when using the left half only. This raises doubts about how well the background emission in the source region is represented by the spectrum extracted from the left half annulus. The source to background ratio of the BACKSCAL and REGAREA values is very similar for the left and right half annulus: BACKSCAL src/left=2.32, REGAREA src/left=2.20, BACKSCAL src/right=2.45, REGAREA src/right=2.29. For reference, the values for the total annulus are BACKSCAL src/bkg=1.47 and REGAREA src/bkg=1.10. The difference in the photon index is comparable for the left half and the total annulus despite the much larger BACKSCAL versus REGAREA difference for the total annulus. On the other hand, there is a much larger photon index deviation between background subtraction and background modelling for the left halt annulus than for the right despite very similar BACKSCAL and REGAREA ratios. This indicates that an eventual scaling problem as discussed in Sect. 3.2 might not be the main reason for the large parameter deviations between the background subtraction and background modelling fit. The sensitivity of the fit results towards the selection of the background region, even for comparable REGAREA and BACKSCAL ratios, points towards N_H variations as a potential additional (or even alternative) reason for deviating parameters of the background subtracted fit.

E. Comparison of sub-regions fits for constant N_H and N_H linked by gradient

In order to support the necessity of introducing a gradient relation linking the N_H values across the remnant, Fig. E1 compares for 5 sub-regions the best-fitting model for a constant N_H to that obtained for the gradient relation. The regions with the most obvious differences were selected to be displayed in the figure. All of them are background regions from either the left or the right side of the remnant (see Fig. 20 for the naming scheme of the pixels). Clearly, for a constant N_H over all regions, the models overestimate the background spectra to the right hand side of the remnant where the absorption is higher, while they underestimate the spectra on the left which are less absorbed. Thus, fitting the spectra of all regions with a constant absorption does not allow to find a good model representation for all of them. This implies that introducing a gradient in N_H is necessary.

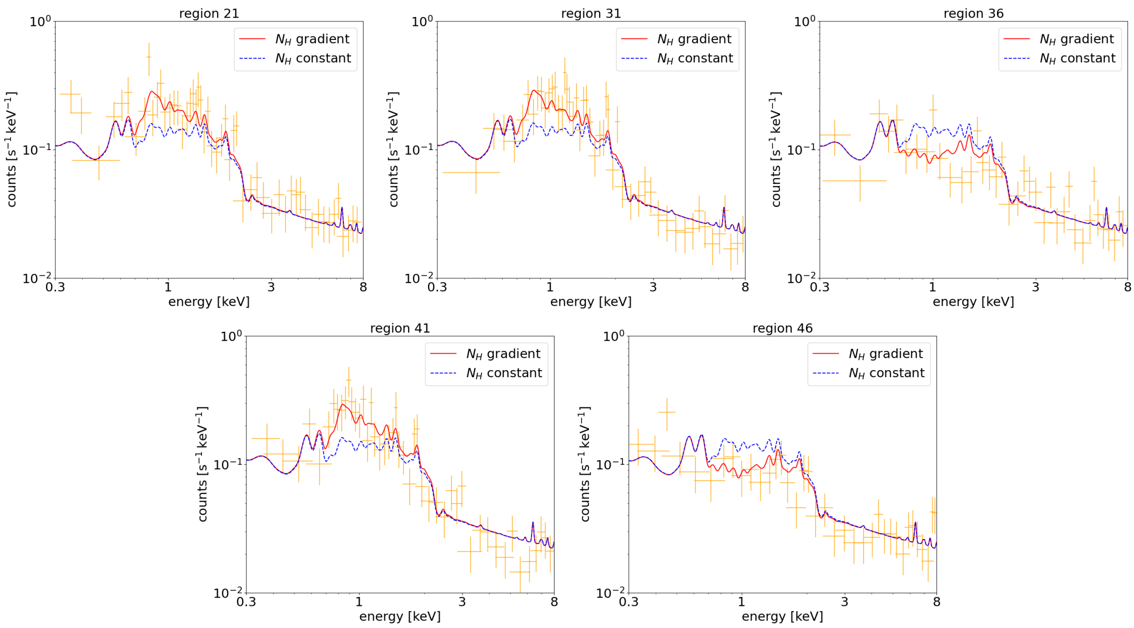

Figure E1: Best-fitting models for a simultaneous fit of all 30 sub-regions with constant (blue) and linked (red) N_H values for regions 21, 31, 36, 41 and 46. These regions have been selected for the figure since they show the most obvious differences between the two cases.

F. Spectra and models for 30 sub-regions with different N_H and Γ relations

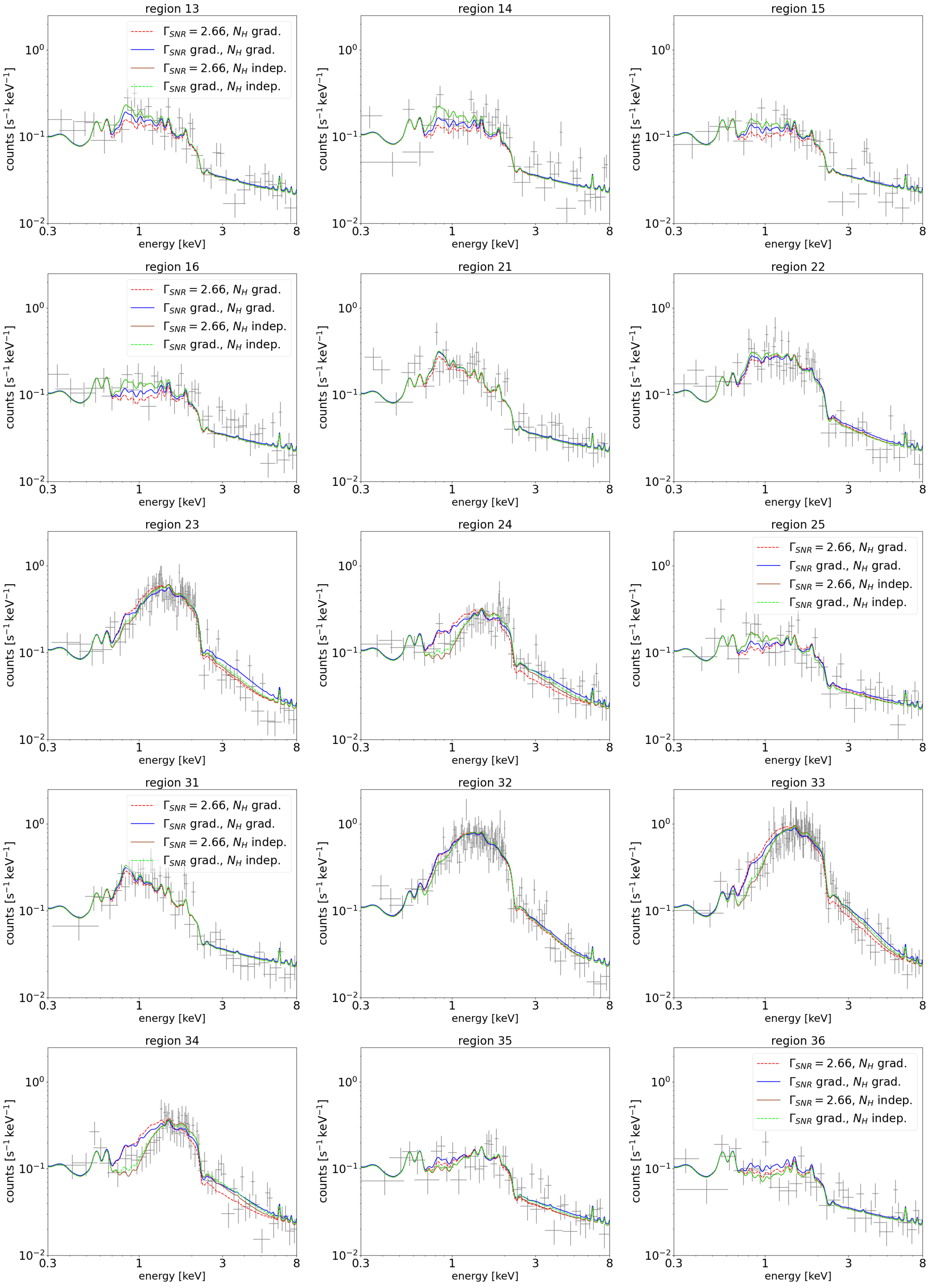

Figure F1: Figure continued on the next page.

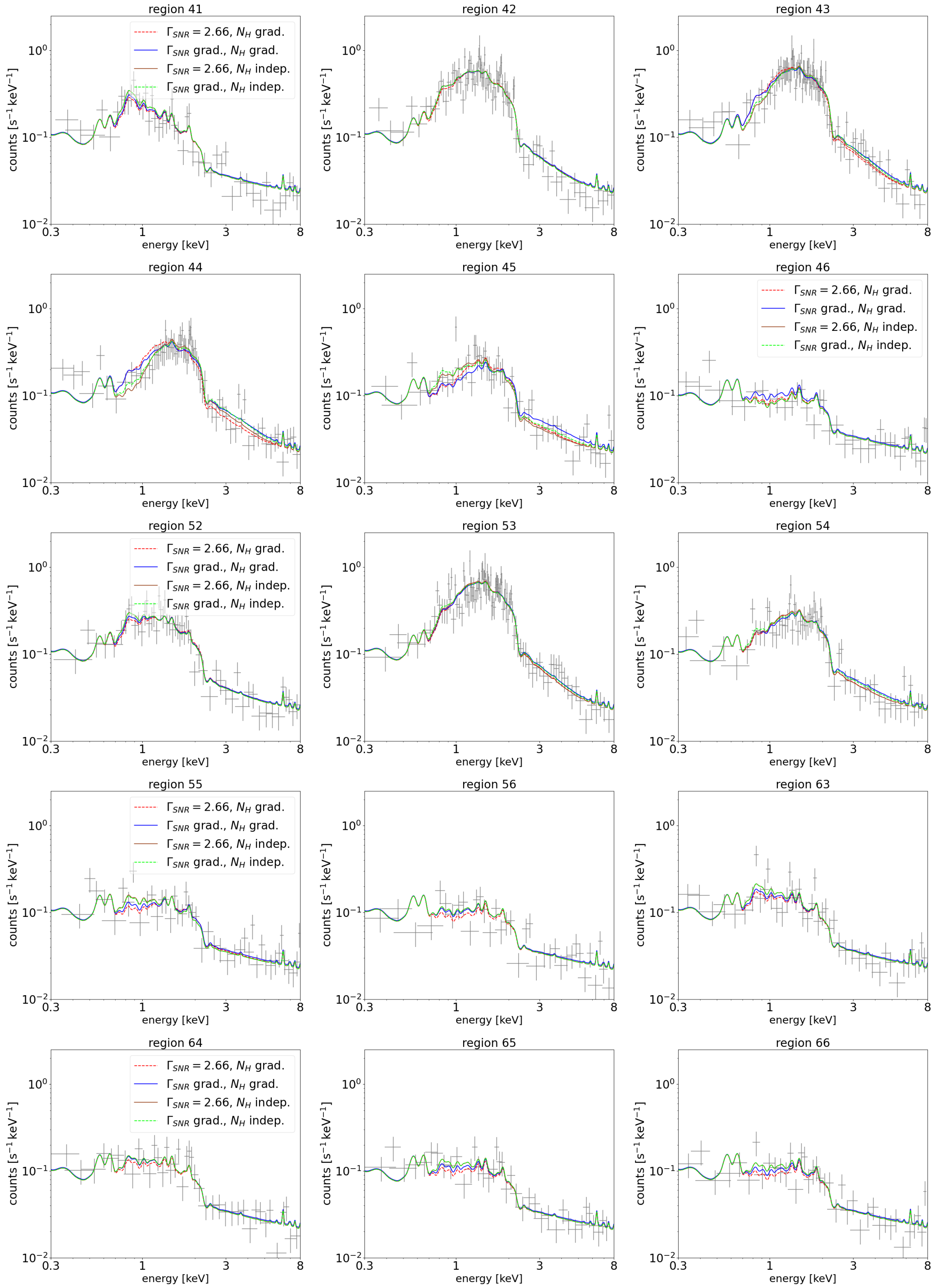

Figure F1: Best-fitting models for the spectra of the 30 sub-regions considered in the analysis (see Fig. 20). Displayed are models for $\Gamma_{SNR} = 2.66$ frozen and N_H linked by the relation defined in Eq. 7 (red dashed line, see Sect. 4.2.1), $\Gamma_{SNR} = 2.66$ frozen and N_H independent (brown solid line, see Sect. 4.2.2), N_H as well as Γ values linked by a gradient relation (blue solid line, see Sect. 4.2.4) and Γ_{SNR} linked by a gradient while N_H is independent (green dashed line, see Sect. 4.2.5). The spectra have been grouped to at least 10 counts per bin for the plot. The fit was performed with a grouping of at least 1 count per bin.

G. Angle spanned by N_H and Γ gradient

In the following, the angle spanned by the N_H and Γ_{SNR} gradient determined in Sect. 4.2.4 and its uncertainties are calculated.
For an angle φ spanned by vector $\vec{a} = (a_1, a_2)$ and $\vec{b} = (b_1, b_2)$, it holds

$$\cos\varphi = \frac{\vec{a} \cdot \vec{b}}{|\vec{a}| \cdot |\vec{b}|} \tag{F1}$$

To simplify the following expressions, the definition

$$\xi := (a_1^2 + a_2^2)(b_1^2 + b_2^2)$$

is introduced. Then,

$$\left(\frac{\partial \cos\varphi}{\partial a_1}\right) = b_1 \cdot \xi^{-\frac{1}{2}} - a_1(b_1^2 + b_2^2)(a_1 b_1 + a_2 b_2)\xi^{-\frac{3}{2}} \tag{F2}$$

$$\left(\frac{\partial \cos\varphi}{\partial a_2}\right) = b_2 \cdot \xi^{-\frac{1}{2}} - a_2(b_1^2 + b_2^2)(a_1 b_1 + a_2 b_2)\xi^{-\frac{3}{2}} \tag{F3}$$

$$\left(\frac{\partial \cos\varphi}{\partial b_1}\right) = a_1 \cdot \xi^{-\frac{1}{2}} - b_1(a_1^2 + a_2^2)(a_1 b_1 + a_2 b_2)\xi^{-\frac{3}{2}} \tag{F4}$$

$$\left(\frac{\partial \cos\varphi}{\partial b_2}\right) = a_2 \cdot \xi^{-\frac{1}{2}} - b_2(a_1^2 + a_2^2)(a_1 b_1 + a_2 b_2)\xi^{-\frac{3}{2}} \tag{F5}$$

The uncertainty in $\cos\varphi$ is according to statistical error propagation:

$$\Delta(\cos\varphi) = \sqrt{\left(\frac{\partial \cos\varphi}{\partial a_1} \cdot \Delta a_1\right)^2 + \left(\frac{\partial \cos\varphi}{\partial a_2} \cdot \Delta a_2\right)^2 + \left(\frac{\partial \cos\varphi}{\partial b_1} \cdot \Delta b_1\right)^2 + \left(\frac{\partial \cos\varphi}{\partial b_2} \cdot \Delta b_2\right)^2} \tag{F6}$$

and the range of angles spanned by the uncertainties is given by:

$$\varphi_{\min} = \arccos(\cos\varphi + \Delta(\cos\varphi)) \tag{F7}$$

$$\varphi_{\max} = \arccos(\cos\varphi - \Delta(\cos\varphi)) \tag{F8}$$

(The cosine function is monotonically decreasing in the interval $[0, \pi]$, therefore the signs are assigned that way.)

Now, the values of the N_H gradient are inserted for $\vec{a}$ and those of the Γ gradient for $\vec{b}$:

$$\vec{a} = \begin{pmatrix} 0.13 \\ 0.01 \end{pmatrix}, \Delta\vec{a} = \begin{pmatrix} 0.01 \\ 0.01 \end{pmatrix} \text{ and } \vec{b} = \begin{pmatrix} -0.39 \\ 0.23 \end{pmatrix}, \Delta\vec{b} = \begin{pmatrix} 0.07 \\ 0.06 \end{pmatrix}$$

Plugging the values in Eq. F7 and F8 yields (using also the precedent equations):

$$\varphi_{\min} = 132.2^\circ \tag{F9}$$

$$\varphi_{\max} = 165.4^\circ \tag{F10}$$

From Eq. F1 follows $\varphi = 145.1^\circ$.

H. Spectra and models for the 22 regions defined by Doroshenko et al. 2017

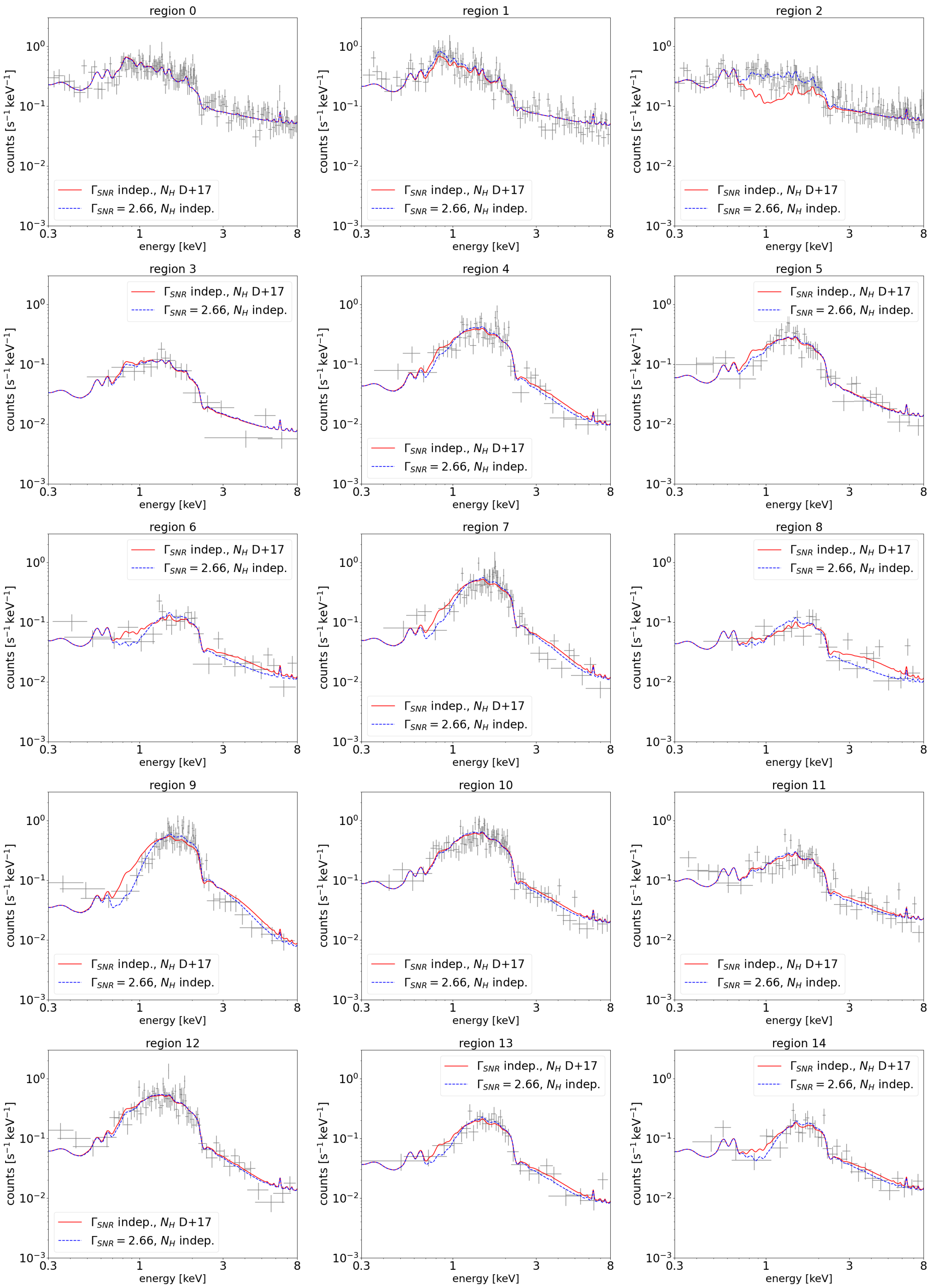

Figure G1: Figure continued on the next page.

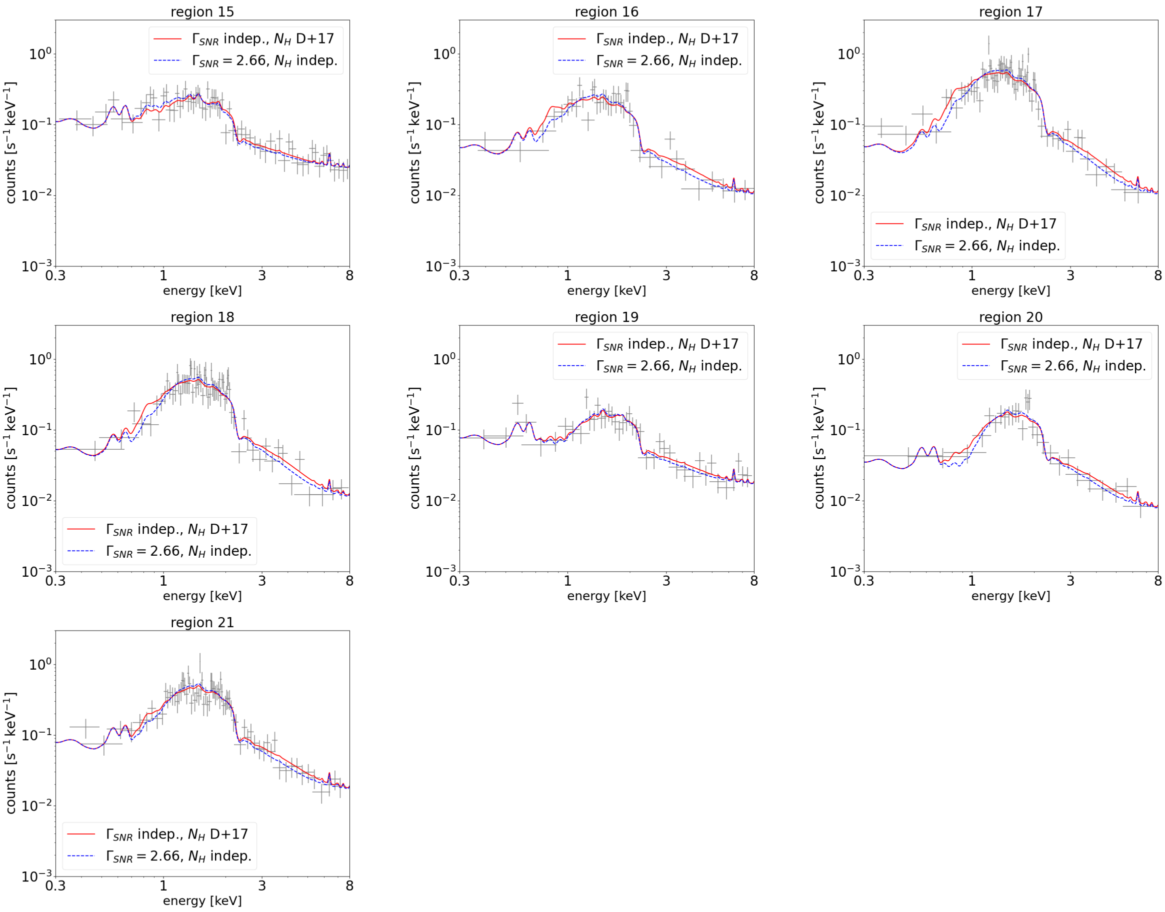

Figure G1: Spectra and best-fitting models for the 22 regions defined by Doroshenko et al. (2017) (see e. g. Fig. 32). Red: The photon index is fixed to 2.66 for all regions and N_H can vary independently. Blue: N_H is fixed to the result Doroshenko et al. (2017) found for each individual region while the photon index can vary independently.